

539

20-73
P-105

**NASA
Technical
Paper
3120**

May 1991

**Development of an Integrated
Aeroservoelastic Analysis
Program and Correlation
With Test Data**

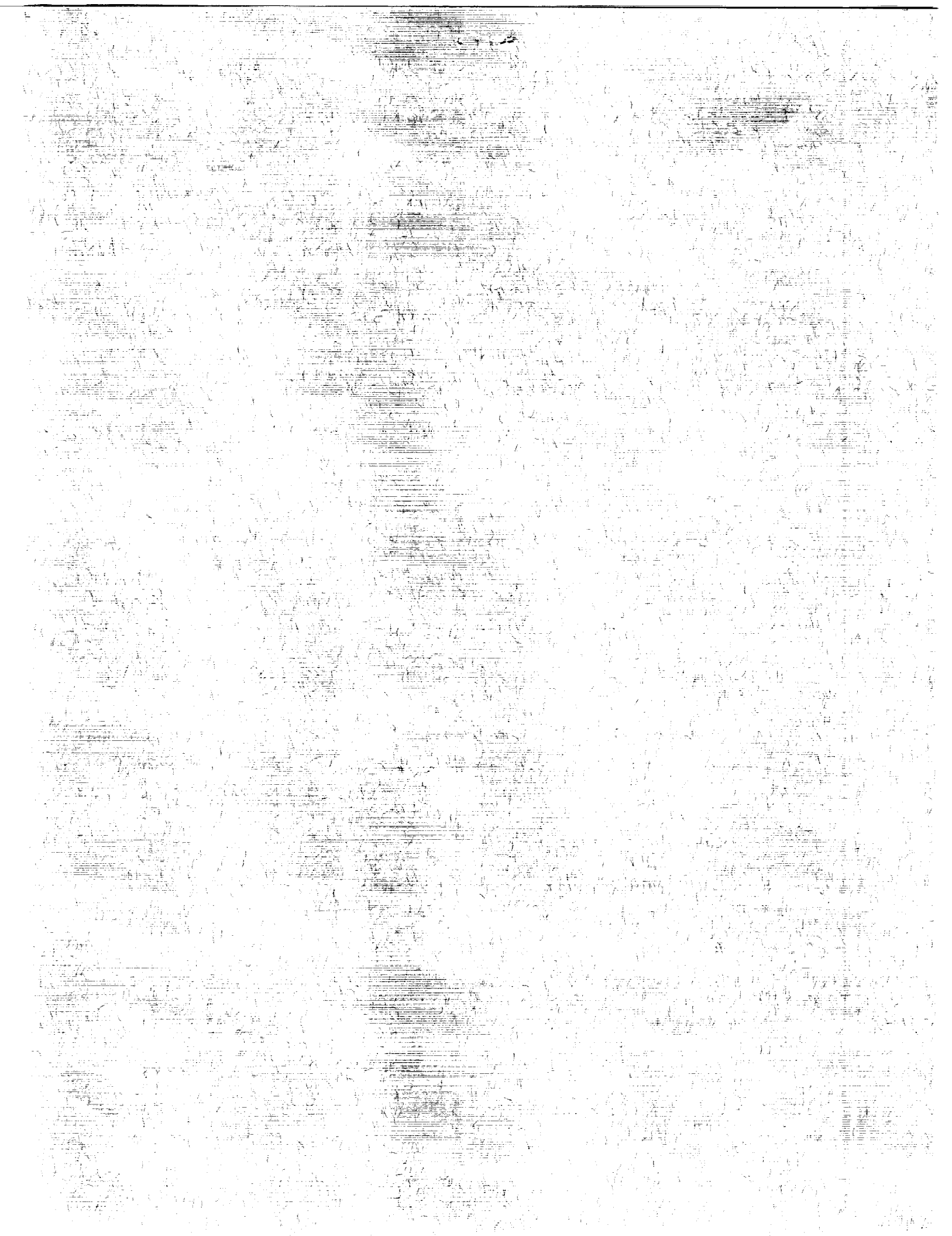
K. K. Gupta, M. J. Brenner,
and L. S. Voelker

DEVELOPMENT OF AN INTEGRATED
AEROSERVOELASTIC ANALYSIS PROGRAM AND
CORRELATION WITH TEST DATA (NASA)

105 p
CSCL 018

Unclas
HI/01 0020543

NASA



**NASA
Technical
Paper
3120**

1991

**Development of an Integrated
Aeroservoelastic Analysis
Program and Correlation
With Test Data**

K. K. Gupta, M. J. Brenner,
and L. S. Voelker
*Dryden Flight Research Facility
Edwards, California*

NASA

National Aeronautics and
Space Administration
Office of Management
Scientific and Technical
Information Division



CONTENTS

SUMMARY	1
NOMENCLATURE	1
INTRODUCTION	4
FORMULATION OF NUMERICAL PROCEDURE	5
Coordinate Transformation	8
Determination of Sensor Outputs	8
Augmentation of Analog Elements and Controller	9
DESCRIPTION OF THE STARS PROGRAM	11
Preprocessor	11
Finite Element Modeling	11
Aeroelastic Analysis	11
Aeroservoelastic (ASE) Controls Analysis	11
Postprocessor	12
NUMERICAL RESULTS	12
Structural Dynamics and Aeroelastic Analysis	12
AEROSERVOELASTIC ANALYSIS—COMPARISONS WITH MEASURED DATA	13
Open-Loop Roots	13
Frequency Responses	14
Flight Data Responses	15
Flight Measured Modal Data	16
CONCLUDING REMARKS	16
TABLES	17
APPENDIX A—FORMULATION OF THE EQUATIONS OF MOTION	21
Coordinate System and Kinematics	21
Kinetic Energy	22
Potential Energy	22
Virtual Work	22
Rigid Body Air Loads	23
Unsteady Aerodynamic Forces	23
Body Forces	23
Gust Loads	24
Engine Thrust	24
Equations of Motion	24
APPENDIX B—INERTIAL-TO-BODY-FIXED COORDINATE TRANSFORMATION	26

APPENDIX C—STABILITY DERIVATIVES	30
Determination of Static and Dynamic Stability Derivatives	30
Longitudinal Derivatives	30
Lateral–Directional Derivatives	31
Aerodynamic Derivative Representation	36
REFERENCES	39

SUMMARY

This report presents the details and results of an extension of the general-purpose finite element SStructural Analysis RoutineS (STARS) to perform a complete linear aeroelastic and aeroservoelastic analysis. The earlier version of the STARS computer program enabled effective finite element modeling as well as static, vibration, buckling, and dynamic response analysis of damped and undamped systems, including those with pre-stressed and spinning structures. Additions to the STARS program include aeroelastic modeling for flutter and divergence solutions, and hybrid control system augmentation for aeroservoelastic analysis.

Numerical results of the X-29A aircraft pertaining to vibration, flutter–divergence, and open- and closed-loop aeroservoelastic controls analysis are compared to ground vibration, wind-tunnel, and flight-test results. The open- and closed-loop aeroservoelastic controls analyses are based on a hybrid formulation representing the interaction of structural, aerodynamic, and flight control dynamics.

NOMENCLATURE

A	plant dynamics matrix in body-fixed coordinates
$\mathbf{A}_e(k)$	aerodynamic influence coefficient matrix
\mathbf{A}_j	coefficient matrices of aerodynamic approximation, ($j = 0, 1 \dots$)
$\hat{\mathbf{A}}$	plant dynamics matrix in inertial frame of reference
$\tilde{\mathbf{A}}$	solution to aerodynamic approximations \mathbf{A}_j from equation (10)
A_x, A_y, A_z	body axis accelerations
AERO7	six-degree-of-freedom, wind-tunnel based aerodynamic simulation data
AIC	aeroelastic influence coefficients
ASE	aeroservoelastic analysis
a_x, a_y, a_z	body axis perturbation accelerations
B	control influence matrix in body-fixed coordinates
\mathbf{B}_e	effective stiffness correction matrix defined in equation (A-26)
$\hat{\mathbf{B}}$	control influence matrix in inertial frame of reference
b	wing span
C	output state matrix in body-fixed coordinates
\mathbf{C}_d	elastic damping matrix
$\hat{\mathbf{C}}$	generalized damping matrix
$\hat{\mathbf{C}}$	$\hat{\mathbf{C}} + \bar{q} \frac{b}{V} \mathbf{A}_1$
C_D, C_L, C_Y	coefficients of drag, lift, and side force
C_l, C_m, C_n	coefficients of roll, pitch, and yaw moment
CPM	constant pressure method
\bar{c}	mean aerodynamic chord
D	output control matrix in body-fixed coordinates
DLM	doublet lattice method
dB	decibel

dof	degree of freedom
E	column of identity matrices
F	force matrix
FEM	finite-element model
G	feedback controller matrix
GVS	ground vibration survey
\bar{g}	gravity vector
g	aeroelastic damping
H	open-loop transfer function matrix of plant and all analog elements
\hat{H}	closed-loop transfer function matrix
H^*	hybrid loop gain matrix
HF X	high frequency crossing (see table 6)
HG X	high gain crossing (see table 6)
I	identity matrix
Im	imaginary part
i^*	$\sqrt{-1}$
K	elastic stiffness matrix
\hat{K}	generalized stiffness matrix
$\hat{\hat{K}}$	$\hat{K} + \bar{q}A_0$ (see equation (15))
\bar{K}_{ee}	effective stiffness matrix
KEAS	knots equivalent airspeed
k	reduced frequency
k_i	discrete set of reduced frequencies
LF X	low frequency crossing (see table 6)
LG X	low gain crossing (see table 6)
M	elastic inertia matrix
\hat{M}	generalized mass matrix
$\hat{\hat{M}}$	$\hat{M} + \bar{q}(\frac{b}{V})^2 A_2$ (see equation (15))
P	forcing function for elastic dynamics
\hat{P}	generalized forcing function
P, Q, R	total roll, pitch, and yaw rate
P_1, Q_1, R_1	reference (trim) roll, pitch, and yaw rate
p, q, r	perturbation roll, pitch, and yaw rate
Q	generalized aerodynamic force matrix
\hat{Q}	approximation of Q
\hat{Q}_R, \hat{Q}_I	real and imaginary parts of \hat{Q}
\bar{Q}	Q without the rigid air loads

$\tilde{\mathbf{Q}}$	stacked matrix of $\tilde{\mathbf{Q}}$ for a discrete set of reduced frequencies
Q	generalized force
\mathbf{q}	displacement vector
\mathbf{q}_s	modal displacements at sensor location
\bar{q}	dynamic pressure
\dot{q}, \ddot{q}	velocity and accelerations
R	matrix (see equation (18))
Re	real part
\mathbf{r}	reference input vector
\vec{r}	position vector
S	see equations (6) and (7)
S	reference area of wing
STARS	SStructural Analysis RoutineS
s	Laplace variable
\mathbf{T}	thrust vector
\mathbf{T}_i	inertial to body-fixed coordinate transformation matrices for rigid body states, $i = 1, 2, 3$ (see appendix B)
$\tilde{\mathbf{T}}_i$	inertial to body-fixed coordinate transformation matrices for combined rigid, elastic, and aerodynamic lag states
\mathbf{T}_s	sensor interpolation matrix
T	sample time for digital controller
U, V, W	total velocities in body-fixed frame of reference
U_1, V_1, W_1	reference (trim) velocities in body-fixed frame of reference
\mathbf{u}	system input vector
u, v, w	perturbation velocities in body-fixed frame of reference
VW	virtual work
$W1B, F1B, \dots$	vibration modes (see tables 1 and 2)
\mathbf{x}	system state vector in body-fixed reference frame
$\hat{\mathbf{x}}$	system state vector in inertial frame
\mathbf{x}_j	j th lag state vector
x, y, z	longitudinal, lateral, and directional displacement
\mathbf{y}	system output vector
α	angle of attack
α_1	trim angle of attack
$\alpha(\omega)$	equivalent downwash
β	angle of sideslip
β_i	aerodynamic lag terms
Γ, Γ_i	inertial to body-fixed coordinate transformation matrices, $i = 1, 2$ (see appendix B)

δ	control surface deflection
η	generalized coordinate vector
Θ, Φ, Ψ	total pitch, roll, and yaw angles
Θ_1, Φ_1, Ψ_1	reference (trim) pitch, roll, and yaw angles
θ, ϕ, ψ	perturbation pitch, roll, and yaw angles
$\Lambda, \tilde{\Lambda}, \Lambda_i, \tilde{\Lambda}_i$	inertial to body-fixed coordinate transformation matrices, $i = 1, 2$ (see appendix B)
τ	system time delay
$\Omega, \tilde{\Omega}$	angular velocity matrices
ω	frequency
ζ	damping

Subscripts

B	body-fixed frame of reference
D	drag
e	elastic
I	inertial frame of reference
L	lift
q	pitch rate
R	real part of a complex number (inertial frame of reference in appendix B)
r	rigid
x, y, z	coordinate system

Superscripts

T	matrix transpose
-1	matrix inverse

INTRODUCTION

Aircraft systems are becoming increasingly complex because of the integration of distinct technologies used to attain numerous objectives in the areas of performance, control, flying qualities, maneuver techniques, fuel efficiency, and various mission requirements. The design process must respond to specifications from all disciplines to achieve these diverse goals and integrate accordingly. Design procedures must account for conflicting objectives and the interaction of dynamics from the control system, structure, and aerodynamics. Coupling between these dynamic elements of the model can be treated passively with structural modifications and passive filtering, or actively with control mechanisms driven by appropriate control laws. Analysis of the consequences of the design is essential to perform safe and effective mission tasks. Aeroservoelastic analysis is used to investigate the potential problems arising from high bandwidth control of relatively flexible aircraft by combining linear models of structure, unsteady aerodynamics, and control system into one dynamic system. The models are augmented to address stability and performance issues.

Vibration, aeroelastic, and aeroservoelastic analyses are presented in this report, computed with the SStructural Analysis RoutineS (STARS) program, an integrated analysis tool evolved from an earlier (ref. 1) finite element structural analysis program. A number of available computer programs perform only individual aspects of these analyses (refs. 2–5). The STARS program was created to analyze complex practical systems such as aircraft and is designed as a unified, compact, modular, and highly graphics oriented analysis tool. Extensive verification and application of the program has been made at the NASA Dryden Flight Research Facility in support of flight programs, such as the X-29A, through correlation of analysis with ground-test and flight-test data. The formulation of the mathematical procedures, a program outline and description, and selected results of these analyses are presented.

FORMULATION OF NUMERICAL PROCEDURE

Extensions made to the STARS program include aeroelastic modeling and control system augmentation to the aero-structural dynamics. An approximation for the unsteady aerodynamics is performed with a Padé fit to the aerodynamic influence coefficients (AIC) to generate a state-space aero-structural dynamic model. This model is transformed from the inertial to body-axis coordinate system for control system augmentation. Aeroservoelastic analysis is achieved for either analog or digital controllers with hybrid frequency responses and eigenvalue solutions for closed-loop modal behavior.

The matrix equation of motion for structures relevant to the current analysis has the following form

$$\mathbf{M}\ddot{\mathbf{q}} + \mathbf{C}\dot{\mathbf{q}} + \mathbf{K}\mathbf{q} + \bar{q}\mathbf{A}_e(k)\mathbf{q} = \mathbf{P}(t) \quad (1)$$

in which

\mathbf{M}	is the inertia matrix,
\mathbf{C}_d	the damping matrix,
\mathbf{K}	the elastic stiffness matrix,
\bar{q}	dynamic pressure,
k	reduced frequency $\frac{\omega\bar{c}}{2V}$, ω and \bar{c} being the natural frequency and mean chord length, respectively,
$\mathbf{A}_e(k)$	the aerodynamic influence coefficient matrix calculated for a given Mach number and set of k values,
\mathbf{q}	the displacement vector, and
$\mathbf{P}(t)$	the external forcing function.

The free vibration solution is first affected (refs. 1 and 6) on the matrix formulation

$$\mathbf{M}\ddot{\mathbf{q}} + \mathbf{K}\mathbf{q} = \mathbf{0} \quad (2)$$

yielding the frequencies, ω , and mode shapes Φ . Applying a transformation

$$\mathbf{q} = \Phi\boldsymbol{\eta} \quad (3)$$

to equation (1) and pre-multiplying both sides by Φ^T yields the generalized equation of motion

$$\hat{\mathbf{M}}\ddot{\boldsymbol{\eta}} + \hat{\mathbf{C}}\dot{\boldsymbol{\eta}} + \hat{\mathbf{K}}\boldsymbol{\eta} + \bar{q}\mathbf{Q}(k)\boldsymbol{\eta} = \hat{\mathbf{P}}(t) \quad (4)$$

where $\hat{\mathbf{M}} = \Phi^T\mathbf{M}\Phi$, $\hat{\mathbf{C}} = \Phi^T\mathbf{C}\Phi$, $\hat{\mathbf{K}} = \Phi^T\mathbf{K}\Phi$, $\mathbf{Q} = \Phi^T\mathbf{A}_e\Phi$, $\hat{\mathbf{P}} = \Phi^T\mathbf{P}$, the modal matrix $\Phi = [\Phi_r\Phi_e\Phi_\delta]$, and the generalized coordinate $\boldsymbol{\eta} = [\eta_r\eta_e\eta_\delta]$, thereby incorporating rigid body, elastic, and control surface motions, respectively. A general Lagrangian formulation of the equations of motion for an aircraft maneuver analysis is given in appendix A.

The generalized aerodynamic force matrix $\mathbf{Q}(k)$ may be approximated (ref. 7) with Padé polynomials in $i^*k (= i^* \frac{\omega \bar{c}}{2V} = \frac{s \bar{c}}{2V}$, where the Laplace variable $s = i^* \omega$)

$$\hat{\mathbf{Q}}(k) = \mathbf{A}_0 + i^*k \mathbf{A}_1 + (i^*k)^2 \mathbf{A}_2 + \frac{i^*k}{i^*k + \beta_1} \mathbf{A}_3 + \frac{i^*k}{i^*k + \beta_2} \mathbf{A}_4 + \dots \quad (5)$$

with aerodynamic lag terms β_j (assume $j = 1, 2$), and

$$\frac{i^*k}{i^*k + \beta_j} = \frac{k^2}{k^2 + \beta_j^2} + \frac{i^*k \beta_j}{k^2 + \beta_j^2}$$

The rigid airload coefficients assume the following form

$$\begin{aligned} \mathbf{A}_0 &= \hat{\mathbf{Q}}_R(k_1) \\ \mathbf{A}_1 &= \frac{\hat{\mathbf{Q}}_I(k_1)}{k_1} - \frac{\mathbf{A}_3}{\beta_1} - \frac{\mathbf{A}_4}{\beta_2} \end{aligned}$$

where k_1 is the smallest reduced frequency, with a value near zero, used to compute \mathbf{A}_j for $j = 0, 1, 2, \dots$. Separating real and imaginary parts in equation (5) yields

$$\begin{aligned} \tilde{\mathbf{Q}}_R(k) &= \hat{\mathbf{Q}}_R(k) - \mathbf{A}_0 \\ &= \begin{bmatrix} -k^2 \mathbf{I} & \frac{k^2}{k^2 + \beta_1^2} \mathbf{I} & \frac{k^2}{k^2 + \beta_2^2} \mathbf{I} \end{bmatrix} \begin{bmatrix} \mathbf{A}_2 \\ \mathbf{A}_3 \\ \mathbf{A}_4 \end{bmatrix} \\ &= \mathbf{S}_R(k) \tilde{\mathbf{A}} \end{aligned} \quad (6)$$

$$\begin{aligned} \tilde{\mathbf{Q}}_I(k) &= \frac{\hat{\mathbf{Q}}_I(k)}{k} - \mathbf{A}_1 \\ &= \begin{bmatrix} \mathbf{0} & \frac{\beta_1}{k^2 + \beta_1^2} \mathbf{I} & \frac{\beta_2}{k^2 + \beta_2^2} \mathbf{I} \end{bmatrix} \begin{bmatrix} \mathbf{A}_2 \\ \mathbf{A}_3 \\ \mathbf{A}_4 \end{bmatrix} \\ &= \mathbf{S}_I(k) \tilde{\mathbf{A}} \end{aligned} \quad (7)$$

The unknown coefficients \mathbf{A}_3 and \mathbf{A}_4 can be determined by substituting the previous expression for \mathbf{A}_1 into equation (7). However, the resulting solution is sensitive to the choice of β_j for approximating rigid airloads. If the elements of the aerodynamic damping matrix \mathbf{A}_1 are replaced with known damping coefficients (steady aerodynamic derivatives), then the solution for rigid airloads becomes insensitive to the β_j values.

For a chosen number of values of reduced frequencies k_i , equations (6) and (7) may be combined as

$$\begin{bmatrix} \tilde{\mathbf{Q}}_R(k_2) \\ \tilde{\mathbf{Q}}_I(k_2) \\ \vdots \\ \tilde{\mathbf{Q}}_R(k_{NF}) \\ \tilde{\mathbf{Q}}_I(k_{NF}) \end{bmatrix} = \begin{bmatrix} \mathbf{S}_R(k_2) \\ \mathbf{S}_I(k_2) \\ \vdots \\ \mathbf{S}_R(k_{NF-1}) \\ \mathbf{S}_I(k_{NF-1}) \end{bmatrix} \begin{bmatrix} \mathbf{A}_2 \\ \mathbf{A}_3 \\ \mathbf{A}_4 \end{bmatrix} \quad (8)$$

or

$$\tilde{\mathbf{Q}} = \mathbf{S} \tilde{\mathbf{A}} \quad (9)$$

and a least-square solution

$$\tilde{\mathbf{A}} = [\mathbf{S}^T \mathbf{S}]^{-1} \mathbf{S}^T \tilde{\mathbf{Q}} \quad (10)$$

yields the required coefficients $\mathbf{A}_2, \mathbf{A}_3, \mathbf{A}_4$. The procedure is easily extended for a larger number of lag terms, if desired. Equation (4) may then be rewritten, assuming simple harmonic motion, as

$$\hat{\mathbf{M}} \ddot{\eta} + \hat{\mathbf{C}} \dot{\eta} + \hat{\mathbf{K}} \eta + \bar{q} [\mathbf{A}_0 \eta + \mathbf{A}_1 \frac{s\bar{c}}{2V} \eta + \mathbf{A}_2 \left(\frac{s\bar{c}}{2V} \right)^2 \eta + \mathbf{A}_3 \mathbf{x}_1 + \mathbf{A}_4 \mathbf{x}_2 + \dots] = \mathbf{0} \quad (11)$$

such that

$$\mathbf{x}_j = \frac{s\eta}{s + \frac{2V}{\bar{c}} \beta_j} \quad (12)$$

from which

$$\dot{\mathbf{x}}_j + \left(\frac{2V}{\bar{c}} \right) \beta_j \mathbf{x}_j = \dot{\eta} \quad (13)$$

Collecting like terms gives

$$(\hat{\mathbf{K}} + \bar{q} \mathbf{A}_0) \eta + \left(\hat{\mathbf{C}} + \bar{q} \frac{\bar{c}}{2V} \mathbf{A}_1 \right) \dot{\eta} + \left(\hat{\mathbf{M}} + \bar{q} \left(\frac{\bar{c}}{2V} \right)^2 \mathbf{A}_2 \right) \ddot{\eta} + \bar{q} \mathbf{A}_3 \mathbf{x}_1 + \bar{q} \mathbf{A}_4 \mathbf{x}_2 + \dots = \mathbf{0} \quad (14)$$

or

$$\hat{\mathbf{K}} \eta + \hat{\mathbf{C}} \dot{\eta} + \hat{\mathbf{M}} \ddot{\eta} + \bar{q} \mathbf{A}_3 \mathbf{x}_1 + \bar{q} \mathbf{A}_4 \mathbf{x}_2 + \dots = \mathbf{0} \quad (15)$$

Rewriting equations (13) and (15) as one matrix equation

$$\begin{bmatrix} \mathbf{I} & & & \\ & \hat{\mathbf{M}} & & \\ & & \mathbf{I} & \\ & & & \mathbf{I} \end{bmatrix} \begin{bmatrix} \dot{\eta} \\ \ddot{\eta} \\ \dot{\mathbf{x}}_1 \\ \dot{\mathbf{x}}_2 \end{bmatrix} = \begin{bmatrix} \mathbf{0} & \mathbf{I} & \mathbf{0} & \mathbf{0} \\ -\hat{\mathbf{K}} & -\hat{\mathbf{C}} & -\bar{q} \mathbf{A}_3 & -\bar{q} \mathbf{A}_4 \\ \mathbf{0} & \mathbf{I} & -\frac{V}{\bar{c}} \beta_1 \mathbf{I} & \mathbf{0} \\ \mathbf{0} & \mathbf{I} & \mathbf{0} & -\frac{V}{\bar{c}} \beta_2 \mathbf{I} \end{bmatrix} \begin{bmatrix} \eta \\ \dot{\eta} \\ \mathbf{x}_1 \\ \mathbf{x}_2 \end{bmatrix} \quad (16)$$

or

$$\mathbf{M}' \dot{\mathbf{x}}' = \mathbf{K}' \mathbf{x}' \quad (17)$$

and

$$\begin{aligned} \dot{\mathbf{x}}' &= (\mathbf{M}')^{-1} \mathbf{K}' \mathbf{x}' \\ &= \mathbf{R} \mathbf{x}' \end{aligned} \quad (18)$$

Now rearranging the state-space vector \mathbf{x}' as

$$\begin{aligned} \mathbf{x}'' &= [(\eta_r, \eta_e, \dot{\eta}_r, \dot{\eta}_e, \mathbf{x}_1, \mathbf{x}_2) \quad (\eta_\delta, \dot{\eta}_\delta)] \\ &= [\hat{\mathbf{x}} \mathbf{u}] \end{aligned} \quad (19)$$

equation (18) may be partitioned as

$$\begin{bmatrix} \dot{\hat{\mathbf{x}}} \\ \dot{\mathbf{u}} \end{bmatrix} = \begin{bmatrix} \mathbf{R}_{1,1} & \mathbf{R}_{1,2} \\ \mathbf{R}_{2,1} & \mathbf{R}_{2,2} \end{bmatrix} \begin{bmatrix} \hat{\mathbf{x}} \\ \mathbf{u} \end{bmatrix} \quad (20)$$

where the first matrix equation denotes the plant dynamics and the second represents the dynamics of control modes. In the case of plant dynamics, the state-space equations become

$$\dot{\hat{\mathbf{x}}} = \hat{\mathbf{A}} \hat{\mathbf{x}} + \hat{\mathbf{B}} \mathbf{u} \quad (21)$$

the associate matrices and vectors being defined as

$\hat{\mathbf{A}}$	plant dynamics matrix
$\hat{\mathbf{B}}$	control surface influence matrix
$\hat{\mathbf{x}}$	generalized coordinates in inertial frame
\mathbf{u}	control surface motion input into plant

and in which the terms $\hat{\mathbf{A}}\hat{\mathbf{x}}$ and $\hat{\mathbf{B}}\mathbf{u}$ represent the airplane dynamics and forcing function due to control surface motion, respectively.

Coordinate Transformation

To incorporate control laws designed to control body-axis motions, it is necessary to transform equation (21) from the Earth-fixed (inertial) to the body-fixed coordinate system. Since no transformations are applied to elastic and aerodynamic lag state vectors, a transformation of the form

$$\begin{aligned}\dot{\mathbf{x}} &= \tilde{\mathbf{T}}_2^{-1}(\hat{\mathbf{A}}\tilde{\mathbf{T}}_1 - \tilde{\mathbf{T}}_3)\mathbf{x} + \tilde{\mathbf{T}}_2^{-1}\hat{\mathbf{B}}\mathbf{u} \\ &= \mathbf{A}\mathbf{x} + \mathbf{B}\mathbf{u}\end{aligned}\quad (22)$$

in which

$$\tilde{\mathbf{T}}_1 = \begin{bmatrix} \mathbf{T}_1 & \mathbf{0} \\ \mathbf{0} & \mathbf{I} \end{bmatrix}$$

Coordinate transformation matrix \mathbf{T}_1 yields the required state-space equation in the body coordinate system. A detailed description of the transformation procedure is given in appendix B.

Determination of Sensor Outputs

The structural nodal displacements are related to the generalized coordinates by equation (3) and the related sensor motion can be expressed as

$$\begin{aligned}\mathbf{q}_s &= \mathbf{T}_s\Phi\boldsymbol{\eta} \\ &= \mathbf{C}_0\mathbf{x}\end{aligned}\quad (23)$$

where $\mathbf{C}_0 = [\mathbf{T}_s\Phi\mathbf{0}\mathbf{0}\mathbf{0}]$, and in which \mathbf{T}_s is an interpolation matrix. Similar relations may be expressed for sensor velocities and acceleration as

$$\begin{bmatrix} \dot{\mathbf{q}}_s \\ \ddot{\mathbf{q}}_s \end{bmatrix} = \begin{bmatrix} \mathbf{T}_s\Phi\dot{\boldsymbol{\eta}} \\ \mathbf{T}_s\Phi\ddot{\boldsymbol{\eta}} \end{bmatrix}\quad (24)$$

$$= \mathbf{C}_1\dot{\mathbf{x}}\quad (25)$$

where

$$\mathbf{C}_1 = \begin{bmatrix} \mathbf{T}_s\Phi & \mathbf{0} & \mathbf{0} & \mathbf{0} \\ \mathbf{0} & \mathbf{T}_s\Phi & \mathbf{0} & \mathbf{0} \end{bmatrix}$$

Pre-multiplying equation (22) by \mathbf{C}_1

$$\begin{aligned}\mathbf{C}_1\dot{\mathbf{x}} &= \mathbf{C}_1\mathbf{A}\mathbf{x} + \mathbf{C}_1\mathbf{B}\mathbf{u} \\ &= \mathbf{C}_2\mathbf{x} + \mathbf{D}_2\mathbf{u}\end{aligned}\quad (26)$$

Adjoining equations (23) and (25)

$$\mathbf{y} = \begin{bmatrix} \mathbf{q}_s \\ \dot{\mathbf{q}}_s \\ \ddot{\mathbf{q}}_s \end{bmatrix} = \begin{bmatrix} \mathbf{C}_0 \\ \mathbf{C}_2 \end{bmatrix} \mathbf{x} + \begin{bmatrix} \mathbf{0} \\ \mathbf{D}_2 \end{bmatrix} \mathbf{u} \quad (27)$$

or

$$\mathbf{y} = \mathbf{C}\mathbf{x} + \mathbf{D}\mathbf{u} \quad (28)$$

which is the required sensor output relationship signifying motion at the sensors due to body motion (\mathbf{C}) and control surface motions (\mathbf{D}).

Augmentation of Analog Elements and Controller

Equations (22) and (27) represent the complete state-space formulation for the aircraft incorporating structural and aeroelastic effects. To conduct an aeroservoelastic analysis, it is essential to augment such a formulation with associated analog elements such as actuators, sensors, notches, and pre-filters along with the controller. Denoting the state-space equation of one such typical element in series as follows

$$\begin{aligned} \dot{\mathbf{x}}^{(i)} &= \mathbf{A}^{(i)}\mathbf{x}^{(i)} + \mathbf{B}^{(i)}\mathbf{u}^{(i)} \\ \mathbf{y}^{(i)} &= \mathbf{C}^{(i)}\mathbf{x}^{(i)} + \mathbf{D}^{(i)}\mathbf{u}^{(i)} \end{aligned} \quad (29)$$

which can be augmented to the plant equations (22) and (27) as

$$\begin{bmatrix} \dot{\mathbf{x}} \\ \dot{\mathbf{x}}^{(i)} \end{bmatrix} = \begin{bmatrix} \mathbf{A} & \mathbf{0} \\ \mathbf{B}^{(i)}\mathbf{C} & \mathbf{A}^{(i)} \end{bmatrix} \begin{bmatrix} \mathbf{x} \\ \mathbf{x}^{(i)} \end{bmatrix} + \begin{bmatrix} \mathbf{B} \\ \mathbf{B}^{(i)}\mathbf{D} \end{bmatrix} [\mathbf{u}] \quad (30)$$

or

$$\dot{\mathbf{x}}_{(i)} = \mathbf{A}_{(i)}\mathbf{x}_{(i)} + \mathbf{B}_{(i)}\mathbf{u} \quad (31)$$

noting that $\mathbf{u}^{(1)} = \mathbf{y}$ from equation (27). Also

$$\begin{bmatrix} \mathbf{y} \\ \mathbf{y}^{(i)} \end{bmatrix} = \begin{bmatrix} \mathbf{C} & \mathbf{0} \\ \mathbf{D}^{(i)}\mathbf{C} & \mathbf{C}^{(i)} \end{bmatrix} \begin{bmatrix} \mathbf{x} \\ \mathbf{x}^{(i)} \end{bmatrix} + \begin{bmatrix} \mathbf{D} \\ \mathbf{D}^{(i)}\mathbf{D} \end{bmatrix} [\mathbf{u}]$$

or

$$\mathbf{y}_{(i)} = \mathbf{C}_{(i)}\mathbf{x}_{(i)} + \mathbf{D}_{(i)}\mathbf{u} \quad (32)$$

becomes the new sensor output expression.

All analog elements, including a controller, can be augmented similarly at the input and the output of the plant. Figure 1 shows a typical feedback control system with controller \mathbf{G} . For such a system the three sets of relevant matrix equations are

$$\begin{aligned} \dot{\mathbf{x}} &= \mathbf{A}\mathbf{x} + \mathbf{B}\mathbf{u} \\ \mathbf{y} &= \mathbf{C}\mathbf{x} + \mathbf{D}\mathbf{u} \\ \mathbf{u} &= \mathbf{r} - \mathbf{G}\mathbf{y} \end{aligned} \quad (33)$$

where equation (32) is the feedback equation. The required transfer functions may be obtained by Laplace transformation

$$\begin{aligned} s\mathbf{x}(s) &= \mathbf{A}\mathbf{x}(s) + \mathbf{B}\mathbf{u}(s) \\ \mathbf{y}(s) &= \mathbf{C}\mathbf{x}(s) + \mathbf{D}\mathbf{u}(s) \\ \mathbf{u}(s) &= \mathbf{r}(s) - \mathbf{G}(s)\mathbf{y}(s) \end{aligned} \quad (34)$$

From equation (33)

$$\mathbf{x}(s) = [s\mathbf{I} - \mathbf{A}]^{-1}\mathbf{B}\mathbf{u}(s) \quad (35)$$

and substituting equation (34) in equation (33) yields the required open-loop frequency response for zero initial conditions

$$\begin{aligned} \mathbf{y}(s) &= [\mathbf{C}(s\mathbf{I} - \mathbf{A})^{-1}\mathbf{B} + \mathbf{D}]\mathbf{u}(s) \\ &= \mathbf{H}(s)\mathbf{u}(s) \end{aligned} \quad (36)$$

where $\mathbf{H}(s)$ is the open-loop transfer function without the controller. To obtain the closed-loop frequency response, equation (35) is first substituted in equation (33) to get

$$\begin{aligned} \mathbf{u}(s) &= \mathbf{r}(s) - \mathbf{G}(s)\mathbf{H}(s)\mathbf{u}(s) \\ &= [\mathbf{I} + \mathbf{G}(s)\mathbf{H}(s)]^{-1}\mathbf{r}(s) \end{aligned} \quad (37)$$

and then using equation (36) gives

$$\begin{aligned} \mathbf{y}(s) &= \mathbf{H}(s)[\mathbf{I} + \mathbf{G}(s)\mathbf{H}(s)]^{-1}\mathbf{r}(s) \\ &= \hat{\mathbf{H}}(s)\mathbf{r}(s) \end{aligned} \quad (38)$$

in which $\hat{\mathbf{H}}(s)$ is the closed-loop transfer function. The frequency response plots can be obtained from the transfer matrices $\mathbf{H}(s)$ or $\hat{\mathbf{H}}(s)$ as the case may be. Associated damping and frequency values of the system may also be calculated by solving the eigenvalue problem of the relevant \mathbf{A} matrix for various k_i values or dynamic pressures and observing the changes in sign of the real part of an eigenvalue to detect instabilities.

In the case of a digital controller, a hybrid approach is adopted for the frequency response solution. Thus if \mathbf{A}' , \mathbf{B}' , \mathbf{C}' , and \mathbf{D}' are the state-space matrices associated with the controller, the related transfer function is simply given by

$$\mathbf{G}(z) = \mathbf{C}'[z\mathbf{I} - \mathbf{A}']^{-1}\mathbf{B}' + \mathbf{D}' \quad (39)$$

and the frequency response formulation (ref. 8) for the hybrid analog-digital system with time delay τ and sample time T can be written as

$$\begin{aligned} \mathbf{y}(s) &= \mathbf{G}(z)_{[z=e^{sT}]} \left(\frac{\mathbf{H}(s)[ZOH]}{T} \right) \mathbf{u}(s) \\ &= \mathbf{G}(s, T)\mathbf{H}^*(s, \tau, T)\mathbf{u}(s) \end{aligned} \quad (40)$$

in which

$$\begin{array}{ll} \mathbf{H}(s) & \text{is the plant transfer function with all analog elements} \\ [ZOH] & \text{is the zero-order hold complex expression } \left(= e^{-s\tau} \frac{1-e^{-sT}}{s} \right) \end{array}$$

and where $\mathbf{H}^*(s, \tau, T)$ is now the loop gain transfer function of the hybrid system. The closed-loop frequency response may be obtained as before by using equations (33) and (39)

$$\begin{aligned} \mathbf{y}(s) &= \left\{ \mathbf{H}^*(s, \tau, T)[\mathbf{I} + \mathbf{G}(s, T)\mathbf{H}^*(s, \tau, T)]^{-1} \right\} \mathbf{r}(s) \\ &= \hat{\mathbf{H}}^*(s, \tau, T)\mathbf{r}(s) \end{aligned} \quad (41)$$

To calculate the damping and frequencies, modes with natural frequencies much beyond the Nyquist frequency are truncated. The analog plant dynamics matrix \mathbf{A} is then transformed into the z -plane by standard discretization procedures and augmented to controller dynamics \mathbf{A}' . Appropriate eigenproblem solution of the final matrix yields the required results, as previously discussed.

DESCRIPTION OF THE STARS PROGRAM

The STARS program primary modules are shown in figure 2. The associated schematic for the aeroservoelastic analysis is shown in figure 3. Some highlights of each module are presented herein.

Preprocessor

This module enables automatic generation of finite element mesh and associated STARS input data for any continuum. The interactive graphics program is capable of generating complex structural systems through interpolation, duplication, mirror-imaging, and cross-sectioning of modular representative forms using menu or command options. This program is designed to run on a wide variety of commonly used graphics terminals.

Finite Element Modeling

This module is made up of many finite elements which are suitable for modeling complex practical structures. Some basic elements are as follows

1. One-dimensional rods, bars, and beam elements,
2. two-dimensional, triangular and quadrilateral elements pertaining to membranes, shear, plate bending, and shells including sandwich and composites,
3. three-dimensional, tetrahedron, prism, and hexahedron elements, and
4. one- and two-dimensional finite dynamic elements.

The desirable features of this module include random data input, bandwidth minimization, multiple coordinate systems, mechanical and thermal loading, general interdependent deflection boundary conditions, automatic node, and element generation as well as plot of geometry.

Aeroelastic Analysis

A newly developed constant pressure method (CPM) (ref. 9) is used for computing unsteady aerodynamic forces for the supersonic flow, whereas the doublet lattice method (DLM) (ref. 5) is used for the corresponding subsonic case. Both k and p - k aerodynamic stability (flutter and divergence) solution methods are available in this module.

Aeroservoelastic (ASE) Controls Analysis

In this module, the aerostructural problem is recast in the Laplace domain and the unsteady generalized aerodynamic forces are curve fitted, using Padé and least-square approximations, to compute state-space matrices. Such matrices are augmented with analog elements such as actuators, sensors, prefilters, and notch filters.

For an analog controller, the state-space matrices are appropriately augmented into that of the entire system and the related transfer function produces the open- and closed-loop frequency responses as desired. The associated modal frequency and damping values may also be derived by solving the eigenvalue problem of the relevant state-space (A) matrix involving the plant dynamics.

In the case of a digital controller, a hybrid approach is adopted in which the associated transfer function is suitably combined with that of the original analog system. This combination yields the hybrid transfer function from which

the open- and closed-loop frequency responses may be computed as desired. To obtain the modal frequency and damping values, the analog A matrix is first discretized and added to the corresponding matrix for the controller.

Furthermore, stability analyses for open-loop flutter and divergence or closed-loop control augmentation aero-servoelastic analysis (ASE) can be performed by solving the appropriate eigenvalue problem. The former analysis can be compared with the aeroelastic analysis using k and p - k methods, whereas the latter analysis proves to be useful for comparing relevant flight-test results of such unstable aircraft as the X-29A.

Postprocessor

Extensive interactive plotting facilities are available for solution results pertaining to each module of the STARS program. These facilities include contour lines of deformations and stresses as well as time-dependent functions of dynamic responses, mode shapes, flutter and divergence plots for k , p - k and root locus methods, and phase and gain plots pertaining to the ASE analyses as well as the corresponding damping and frequency plots.

NUMERICAL RESULTS

The presently developed integrated aero-structural-control analysis program STARS has been used extensively to solve related problems of the X-29A forward-swept wing research aircraft (refs. 10 and 11) (fig. (4)). The X-29A aircraft has thin wings of composite materials that are aeroelastically tailored to eliminate structural divergence within the flight envelope. Full-span, double hinged, variable-camber flaperons and strake flaps operate with full-authority variable-incidence canards to yield minimum trim drag. The presence of the supercritical airfoil enables efficient transonic cruise performance and high transonic maneuvering. The canard configured aircraft is up to 35-percent statically unstable, thus requiring appropriate feedback controls for augmented static stability. Whereas these combined technologies result in significant improvement in overall aerodynamic and structural performance, they may also cause adverse dynamic interaction of the flight controls with the flexible structure if not integrated properly. Therefore an ASE analysis assumes a very important role in the design process.

In this report a comparison of ASE as well as vibration and aeroelastic analysis of the X-29A aircraft between the STARS calculated results and test results is presented in detail.

Structural Dynamics and Aeroelastic Analysis

A finite element model of the X-29A aircraft is shown in figure 5. This somewhat reduced dynamic model (approximately 3000 dof) was derived from the detailed stress model (7100 dof) by using an equivalent shell method for the various appendages to reduce free vibration analysis time. The fuselage was modeled with line elements and the vibration problem for the entire structure was solved by a block Lanczos procedure (refs. 1 and 12). A summary of such free vibration analysis results is compared with those obtained by the ground vibration survey (GVS) as shown in tables 1 and 2 for the symmetric and antisymmetric cases, respectively. The corresponding node line comparisons are shown in figures 6 and 7. A more detailed presentation of the vibration results can be found in reference 13.

Extensive aeroelastic analyses were performed to determine flutter and divergence speeds of the aircraft employing the k , p - k , and root-contour methods for comparison purposes; associated STARS unsteady aerodynamic paneling is shown in figure 8. Such results from the STARS model are compared with GVS results in tables 3 and 4, where the column labeled STARS (ASE) represents the results of the eigensolution of the plant A matrix, whereas figures 9 through 12 show the various flutter solution plots.

In general, good correlation of results for various cases was observed from the results presented herein. A more detailed mode-by-mode comparison of these results is presented in reference 13.

AEROSERVOELASTIC ANALYSIS—COMPARISONS WITH MEASURED DATA

The [A, B, C, D] dynamic system computed by STARS is compared with measured data in the form of a linearized aerodynamic database for the X-29A aircraft, called AERO7, and flight data. The AERO7 is a nonlinear, six dof, rigid body wind-tunnel database with flexibility corrections to the rigid data, heretofore denoted as flexibilized data. The comparisons consist of

1. Open-loop roots: the rigid body modal characteristics from linearized AERO7 data, the STARS rigid body modes, and the STARS model with all rigid and elastic modes included, are represented.
2. Frequency responses: loop gain and longitudinal closed-loop responses are computed with measured GVS and STARS modal data aircraft dynamics augmented to a digital flight control system. Stability margins are also compared.
3. Flight data responses: longitudinal loop gains computed from STARS are compared with those generated from flight data and linearized AERO7 data, and
4. Flight measured modal data: flight determined modal damping and frequency results are compared to STARS results for the first two symmetric modes and first three antisymmetric modes.

The four flight conditions analyzed are

1. Mach 0.7 at 40,000-ft altitude,
2. Mach 0.9 at 30,000-ft altitude,
3. Mach 0.9 at 15,000-ft altitude, and
4. Mach 1.2 at 30,000-ft altitude.

Condition 1 is a low dynamic pressure case, 2 is the X-29A aircraft design point, 3 is a high dynamic pressure condition, and 4 is a supersonic point where the CPM was used to calculate the theoretical data.

Open-Loop Roots

The rigid body roots are tabulated in tables 5(a), (b), (c), and (d) for the longitudinal modes (phugoid and short period) and lateral-directional modes (spiral, roll, and dutch roll). Complex poles are written as (ω, ζ) . The STARS roots are compared to linearized rigid (without flexibility corrections) and flexibilized AERO7 data. The STARS rigid body model (rigid) contains all unsteady lag states on the rigid body and control modes, but no elastic modes or AERO7 flexibilized data corrections to the generalized aerodynamic stiffness and damping matrices (appendix C) are included. The models generated with lag states on only rigid and control modes by incorporating AERO7 flexibilized stability derivatives into the generalized aerodynamic stiffness and damping matrices are designated as Rigid-flexibilized in the tables. The flexible model (flexible) consists of all rigid, elastic, and control modes with lag states included. Flexible models are corrected with rigid AERO7 derivatives (not flexibilized) since the flexibility effects are already modeled by incorporation of the elastic modes.

The columns labeled Full contain roots computed from a full-order model, either containing only the rigid modes (rigid and rigid/flexibilized) or both rigid and elastic modes (flexible). Columns designated Reduced represent roots computed from a reduced form of the full-order model by only including the static contribution of the excluded

states. Those states describing rigid body dynamics are retained and all other states are excluded in the reduced-order model to represent the static contribution of flexibility as well as unsteady aerodynamics on the rigid model. Hence, the state vector is partitioned into rigid body states (r), and all other states (o) in the model, as

$$\mathbf{x} = \begin{pmatrix} \mathbf{x}_r \\ \mathbf{x}_o \end{pmatrix}$$

and the \mathbf{A} , \mathbf{B} , \mathbf{C} system is similarly partitioned as

$$\mathbf{A} = \begin{pmatrix} \mathbf{A}_{rr} & \mathbf{A}_{ro} \\ \mathbf{A}_{or} & \mathbf{A}_{oo} \end{pmatrix} \quad \mathbf{B} = \begin{pmatrix} \mathbf{B}_r \\ \mathbf{B}_o \end{pmatrix} \quad \mathbf{C} = (\mathbf{C}_r \quad \mathbf{C}_o)$$

where \mathbf{D} is unchanged. Then the reduced model is given by

$$\begin{aligned} \dot{\mathbf{x}}_r &= (\mathbf{A}_{rr} - \mathbf{A}_{ro}\mathbf{A}_{oo}^{-1}\mathbf{A}_{or}) \mathbf{x}_r \\ &\quad + (\mathbf{B}_r - \mathbf{A}_{or}\mathbf{A}_{oo}^{-1}\mathbf{B}_o) \mathbf{u} \\ \mathbf{y} &= (\mathbf{C}_r - \mathbf{C}_o\mathbf{A}_{oo}^{-1}\mathbf{A}_{or}) \mathbf{x}_r \\ &\quad + (\mathbf{D} - \mathbf{C}_o\mathbf{A}_{oo}^{-1}\mathbf{B}_o) \mathbf{u} \end{aligned}$$

Residualization of the states in this way results in a reduced-order model reflecting the effects of the deleted elastic as well as unsteady dynamics on the rigid body modes. The coupling may be significant especially when the aircraft is relatively flexible (ref. 14).

The root comparisons between the STARS corrected models and AERO7 models are quite good for all modes except the phugoid and spiral modes. In fact, STARS predicts totally damped phugoid characteristics instead of the expected oscillatory behavior. These very low frequency modes are difficult to predict with a Padé fit over a wide reduced frequency range. Results using the generalized forces at one or two of the lowest reduced frequencies with zero or first-order Padé fits show more reasonable behavior for both phugoid and spiral modes. This procedure is recommended if aeroelastic effects are being investigated on only these low frequency modes. The other modes with more reduced frequencies included, however, are reproduced very well with the present STARS implementation of AERO7 data.

The uncorrected STARS model does not have a well defined phugoid because the forces in the forward velocity dof are zero (appendix C). Hence, a root at zero is evident in all cases. The other root is therefore meaningless. A comparison of the rigid AERO7 model and the uncorrected rigid STARS model shows how well the theoretical STARS aerodynamic model compares to a wind-tunnel derived model. The roll and dutch roll modes demonstrate excellent agreement, while the short period is not as close in agreement, but reasonable.

Aeroelastic effects are most noticeable at flight condition 3, the high dynamic pressure transonic condition, where differences between rigid AERO7 and flexibilized AERO7 are most evident, but still not significant. The STARS program also demonstrates flexible effects when comparing the rigid roots with flexible model roots. Similar minor differences between full-order and reduced-order solutions are also evident, showing that flexibility effects on rigid body stability are essentially negligible.

In general, the comparisons validate the ability of STARS to reproduce rigid body dynamics with flexibility effects.

Frequency Responses

Loop gains and longitudinal closed-loop frequency responses were computed and stability margins determined for the four flight conditions with the digital normal mode (ref. 11) control system augmented to the aircraft states.

The longitudinal and lateral-directional control system block diagrams are shown in figures 13 and 14, respectively. Hybrid frequency responses (ref. 8) were calculated to account for aliasing effects of dynamics with frequencies higher than the Nyquist frequency of 20 Hz (126 rad/sec). Points designated OL in the diagrams represent open-loop response locations. The C_L locations in figure 13 are the longitudinal closed-loop input-output signals from filtered pilot stick position to aircraft pitch rate response since pitch rate is the dominant feedback variable.

Stability margins for all augmented models are displayed in tables 6(a), (b), (c), and (d). Loop gains are plotted in figures 15 to 18 (longitudinal), figures 19 to 22 (lateral), and figures 23 to 26 (directional) for all four flight conditions analyzed, using measured GVS modal data and modes generated from the STARS. Aircraft dynamics include all rigid, elastic, and control modes with lag states and AERO7 flexibilized data incorporated. Control system dynamics include all elements shown in figures 13 and 14.

Longitudinal frequency response overplots in figures 15 to 18 show some dissimilarity between 30 and 100 rad/sec due to the first two symmetric elastic modes. Pitch rate response from the first wing bending and first fuselage vertical bending modes is more pronounced from the measured GVS modal data than from STARS modes. Notch filters were designed for the X-29A aircraft to gain stabilize all modal responses to less than -6 dB in the loop gains throughout the flight envelope. Condition 3 at Mach 0.9, 30,000-ft altitude was one of the most critical points in the longitudinal axis. Lateral responses in figures 19 to 22 show fairly benign modal contributions to feedbacks, and the measured model is not dramatically different from the STARS model. Supersonic condition 4 shows some offset between the gain curves due to differences in aileron effectiveness. The directional responses in figures 23 to 26 demonstrate a much more significant discrepancy between 50 and 100 rad/sec, amounting to 20 to 30 dB in this frequency range. Modal contributions from the first three antisymmetric elastic modes to the yaw rate feedback are 10 to 30 times greater from the measured GVS data than from the STARS model.

These observations demonstrate an important aspect of the ASE modeling process. A critical issue for an accurate analysis is the sensor feedback motion caused by modal dynamics. Since the feedback sensors are usually located in the fuselage, the fuselage motion at the sensor locations must be determined precisely. Sufficient accuracy is difficult to obtain from a finite element model of the fuselage. A very detailed high-order stress model is needed to obtain the proper sensor motion due to fuselage dynamics. Slight differences in mode shapes between the model and actual aircraft can result in significant discrepancies in feedback dynamics between the model prediction and actual aircraft. A ground test is essential to determine the actual feedback due to modal dynamics. The X-29A aircraft ground tests demonstrated that the discrepancies were extremely significant (ref. 4).

Longitudinal closed-loop plots in figures 27 to 30 for all four flight conditions reveal the flexibility of the GVS aircraft model compared to the STARS model. Closed-loop models are significantly different representations of the dynamic interaction between the digital control system and flexible-unsteady effects, in contrast to the equivalent open-loop description, since the dynamics beyond the Nyquist frequency are propagated through all discrete and continuous elements simultaneously. The consequences of sampling and aliasing on these dynamics contribute to the modal interaction between the controller and aircraft model. Analysis using the entire closed-loop spectrum may expose possible problems in the feedback mechanism due to the interface of discrete and continuous dynamics. The relatively small differences between STARS and GVS models in the longitudinal loop gains of figures 15 to 18 are magnified when the loops are closed in the corresponding closed-loop plots of figures 27 to 30, yet closed-loop modal damping is adequate as a result of notch filter design. In these cases, closed-loop plots seem to exaggerate minor differences in modal damping between GVS and STARS models, which also depend on phase relationships between modal dynamics and feedback sensor motions.

Flight Data Responses

Loop gains were computed for the longitudinal axis from flight data (ref. 15) and are compared with the augmented flexible (including all rigid, elastic, control, and lag states) STARS models in figures 31 to 34 for all flight

conditions analyzed. Correlation is excellent for the spectrum range of the measured data. The AERO7 models are overplotted for reference. The STARS models match the flight data as well as AERO7 models for all flight conditions shown. These STARS models are corrected with rigid AERO7 coefficients as outlined in appendix C. Hence, the plots show that STARS models flexibilized by incorporating the calculated mode shapes properly represent the rigid body motion.

Flight Measured Modal Data

Figures 35 and 36 portray good agreement between flight measured modal results and STARS calculations for the symmetric wing first bending and fuselage first vertical bending modes. The STARS data are obtained by calculating the roots of the flexible model augmented to the digital control system. This procedure is possible only for those modes with natural frequencies up to and near the Nyquist frequency. Such similarities between STARS and flight results validate the STARS formulation for the entire flight envelope. Antisymmetric correlations shown in figures 37 to 39 for the antisymmetric wing first bending, fuselage first lateral bending, and fin first bending also show the effectiveness of STARS to predict elastic behavior. The only noticeable difference between the STARS results and flight data is in the antisymmetric wing first bending damping and frequency at lower altitudes. The STARS program predicts a higher damping and lower frequency and is therefore less conservative at these conditions. At higher altitudes the correlation is much better for this mode.

CONCLUDING REMARKS

The mathematical formulation of the procedures to perform vibration, aeroelastic, and aeroservoelastic analyses with the structural analysis routines program has been presented, along with numerical results for the X-29A aircraft. Interaction of structural dynamics, aerodynamics, and flight control systems is modeled using both a finite element model and measured modes to predict flutter-divergence and aeroservoelastic phenomena. Correlation with measured data from ground tests as well as flight measured results is used to validate the capability of STARS to analyze complex dynamical systems such as flexible aircraft controlled with digital control systems.

*Dryden Flight Research Facility
National Aeronautics and Space Administration
Edwards, California, March 20, 1989.*

Table 1. Free vibration analysis results for X-29A symmetric half-aircraft.

Primary motion	STARS	GVS
	frequency, Hz	frequency, Hz
Rigid body	0.00	n/a
Wing first bending (<i>W1B</i>)	8.96	8.61
Fuselage first vertical bending (<i>F1B</i>)	12.87	11.65
Fuselage second vertical bending (<i>F2B</i>)	19.03	24.30
Canard pitch (<i>CP</i>)	21.02	21.70
Wing second bending (<i>W2B</i>)	26.28	26.30
Wing first torsion (<i>W1T</i>)	30.30	36.70
Canard bending pitch (<i>CBP</i>)	47.70	42.20
Wing third bending (<i>W3B</i>)	49.52	51.50

Table 2. Free vibration analysis results for X-29A antisymmetric half-aircraft.

Primary Motion	STARS	GVS
	frequency, Hz	frequency, Hz
Rigid body	0.00	n/a
Wing first bending (<i>W1B</i>)	10.08	11.3
Fuselage first bending (<i>F1B</i>)	12.35	12.5
Fin first bending (<i>Fin1B</i>)	17.18	15.2
Canard pitch (<i>CP</i>)	21.52	21.9
Wing first torsion (<i>W1T</i>)	27.15	26.8
Wing second bending (<i>W2B</i>)	32.88	34.8
Fin second bending (<i>Fin2B</i>)	41.58	45.2
Wing third bending (<i>W3B</i>)	45.85	51.7
Fin first torsion (<i>Fin1T</i>)	48.95	50.0
Inboard flap torsion (<i>IFT</i>)	50.83	51.0

Table 3. X-29A aircraft flutter and divergence speeds for symmetric modes.

Mode	Divergence point, KEAS			Flutter point, KEAS		
	STARS	STARS		STARS	STARS	
	k	ASE	GVS	k	ASE	GVS
<i>W1B</i>	833	819	865	---	---	---
<i>CP</i>	912	910	1017	---	---	---
<i>CBP</i>	---	---	---	---	---	694
<i>W3B</i>	---	---	---	1275	1231	1222

Table 4. X-29A aircraft flutter and divergence speeds for antisymmetric modes.

Mode	Divergence point, KEAS			Flutter point, KEAS		
	STARS	STARS		STARS	STARS	
	k	ASE	GVS	k	ASE	GVS
W1B	838	833	808	---	---	---
F1B	---	---	---	848	797	924
CP	913	918	980	---	---	---
W2B	---	---	---	1143	1157	1315

Table 5. Comparison of rigid body modal characteristics between STARS and linearized aerodynamic database for X-29A aircraft.

Mode	Model							
	Linear rigid	STARS rigid		Linear flexibilized	STARS rigid/flexibilized		STARS flexible	
	AERO7	Full	Reduced	AERO7	Full	Reduced	Full	Reduced
(a) Mach = 0.7, altitude = 40,000 ft.								
Phugoid	(0.7,0.08)	0.0,0.11	0.0,0.12	(0.07,0.08)	-0.01,-0.12	-0.001,-0.12	-0.001,-0.12	-0.001,-0.12
Short period	2.1,-2.7	0.9,-1.3	0.9,-1.3	2.1,-2.7	2.3,-2.7	2.3,-2.6	2.3,-2.7	2.3,-2.6
Spiral	0.03	0.0005	0.0005	0.03	0.5	0.003	0.5	-0.001
Roll	-1.1	-1.1	-1.3	-1.1	-1.3	-0.9	-1.3	-1.0
Dutch roll	(1.9,0.05)	(1.6,0.07)	(1.6,0.07)	(1.9,0.05)	(2.2,0.05)	(2.0,0.08)	(2.2,0.05)	(2.0,0.08)
(b) Mach = 0.9, altitude = 30,000 ft.								
Phugoid	(0.08,0.17)	0.0,0.32	0.0,0.35	(0.08,0.17)	-0.003,-0.28	-0.003,-0.28	-0.003,-0.31	-0.003,-0.32
Short period	3.2,-4.5	1.1,-2.3	1.1,-2.3	3.3,-4.6	3.6,-4.6	3.5,-4.4	3.6,-4.5	3.5,-4.3
Spiral	0.01	0.000	0.000	0.01	0.3	0.002	0.3	-0.003
Roll	-2.4	-2.4	-2.5	-2.4	-2.0	-1.9	-2.2	-2.2
Dutch roll	(2.9,0.05)	(2.7,0.08)	(2.7,0.08)	(2.9,0.05)	(3.4,0.07)	(3.0,0.13)	(3.4,0.07)	(3.1,0.12)
(c) Mach = 0.9, altitude = 15,000 ft.								
Phugoid	(0.09,0.26)	0.0,-0.002	0.0,-0.002	(0.08,0.27)	-0.005,-0.48	-0.005,-0.50	-0.005,-0.60	-0.005,-0.62
Short period	4.2,-6.5	1.7,-3.1	1.7,-3.1	4.4,-6.9	5.1,-7.0	4.9,-6.5	4.9,-6.8	4.7,-6.3
Spiral	0.01	0.0002	0.0002	0.01	0.2	0.002	0.2	-0.009
Roll	-4.9	-4.4	-4.6	-4.9	-3.4	-3.6	-4.3	-4.7
Dutch roll	(3.8,0.07)	(3.7,0.10)	(3.7,0.09)	(3.8,0.07)	(4.4,0.08)	(3.8,0.15)	(4.4,0.06)	(4.0,0.14)
(d) Mach = 1.2, altitude = 30,000 ft.								
Phugoid	(0.07,0.22)	0.0,-0.32	0.0,-0.31	(0.08,0.22)	0.0,-0.40	0.0,-0.39	0.0,-0.37	0.0,-0.37
Short period	2.4,-4.0	1.7,-2.4	1.7,-2.5	2.4,-4.1	3.0,-5.2	3.0,-4.9	2.9,-5.2	2.9,-4.9
Spiral	0.006	-0.0003	-0.0003	0.006	0.208	0.003	0.16	-0.034
Roll	-4.1	-4.0	-3.9	-4.1	-3.2	-3.2	-4.0	-4.0
Dutch roll	(4.2,0.08)	(3.9,0.09)	(3.8,0.10)	(3.8,0.08)	(4.6,0.08)	(3.7,0.15)	(4.4,0.08)	(3.5,0.14)

Table 6. Comparison of gain/phase margins between STARS models and models based on linearized aerodynamic data for X-29A aircraft.

Axis	Model		
	AERO7 flexibilized	STARS rigid/ flexibilized	STARS flexible
(a) Mach = 0.7, altitude = 40,000 ft.			
Pitch			
LF X/gain margin	1.26/7.84	1.15/6.38	1.15/6.41
HF X/gain margin	23.9/11.2	24.1/11.3	24.2/11.4
Gain X	5.89	5.53	5.54
Phase margin	49.0	48.5	48.6
Roll			
Frequency X	15.2	14.9	15.0
Gain X	2.45	2.13	2.09
Gain margin	17.9	19.2	19.4
Phase margin	78.8	74.5	75.3
Yaw			
Frequency X	11.1	11.2	11.0
Gain X	3.87	4.13	4.06
Gain margin	12.0	10.8	10.9
Phase margin	62.1	63.9	64.6
(b) Mach = 0.9, altitude = 30,000 ft.			
Pitch			
LF X/gain margin	2.23/7.88	2.01/6.54	2.01/6.74
HF X/gain margin	23.8/6.65	23.6/6.49	23.5/6.47
Gain X	9.64	9.16	9.33
Phase margin	41.3	41.2	40.3
Roll			
Frequency X	13.7	14.0	14.0
Gain X	2.69	2.5	2.33
Gain margin	17.0	18.9	19.6
Phase margin	68.0	57.3	61.4
Yaw			
Frequency X/gain margin	13.2/11.3	13.6/10.5	13.6/11.2
LG X/phase margin	1.46/268.0	1.47/262.0	1.50/261.0
HG X/phase margin	5.64/56.1	5.94/60.10	5.65/62.7

Table 6. Concluded.

Axis	Model		
	AERO7 flexibilized	STARS rigid/ flexibilized	STARS flexible
(c) Mach = 0.9, altitude = 15,000 ft.			
Pitch			
LF X/gain margin	2.85/7.17	2.29/5.37	3.20/5.76
HF X/gain margin	26.4/6.47	26.1/6.22	25.6/5.97
Gain X	12.3	11.3	11.7
Phase margin	38.7	39.6	37.5
Roll			
Frequency X	13.3	12.9	13.3
Gain X	3.47	3.42	2.93
Gain margin	15.0	16.5	18.2
Phase margin	66.0	48.2	59.9
Yaw			
Frequency X	13.1	13.8	13.7
LG X/phase margin	2.36/248	2.38/241	2.46/239
HG X/phase margin	5.91/54.2	5.84/66.2	5.45/69.4
Gain margin	12.6	12.2	13.4
(d) Mach = 1.2, altitude = 30,000 ft.			
Pitch			
LF X/gain margin	2.08/9.98	1.49/7.85	2.33/8.07
HF X/gain margin	24.7/7.28	24.4/7.03	24.9/7.67
Gain X	9.26	8.66	8.17
Phase margin	45.8	44.8	43.5
Roll			
Frequency X	12.5	12.5	12.3
Gain X	2.62	2.75	2.13
Gain margin	16.9	18.4	20.4
Phase margin	72.0	57.3	72.3
Yaw			
Frequency X	13.2	13.8	13.7
LG X/phase margin	2.25/248	2.21/245	2.29/243
HG X/phase margin	6.73/48.2	6.99/54.7	6.30/60.3
Gain margin	10.3	9.45	11.0

APPENDIX A FORMULATION OF THE EQUATIONS OF MOTION

The equations of motion of an aircraft or a flight vehicle can be derived by considering various forces acting on the system. In classical mechanics, a Lagrangian definition of the equations enables a suitable derivation of the equilibrium state of a flying vehicle. This derivation requires certain physical concepts leading to the definition of the energy and the kinematics. The energy can be expressed in terms of kinetic energy, potential energy, and the virtual work done. The kinematics are generally expressed with respect to an inertial coordinate system which is assumed to be at rest. In the study of space-bound vehicles, such an inertial system is referenced to a distant star. However, in the case of an Earth-bound vehicle, the inertial system can be fixed to the center of the Earth where it is assumed that the angular velocities and the linear motions of the Earth have little effect on the dynamics of the aircraft.

Coordinate System and Kinematics

Let the position vector of a mass point on the aircraft be described by

$$\vec{r}_i = \vec{r}_r + \vec{r}_{b_i} + \vec{q}_{e_i} \quad (\text{A-1})$$

where

- \vec{r}_i is the position vector of the mass point i
- \vec{r}_r is the position vector of the rigid body-fixed coordinate system origin O with respect to inertial space
- \vec{r}_{b_i} is the position vector of mass point i with respect to origin O
- \vec{q}_{e_i} is a vector of the deformation of the mass i with respect to the rigid body-fixed coordinate system

If P , Q , and R are the angular velocities of the aircraft measured about the rigid body-fixed axis system, then the velocity of the mass can be written as

$$\dot{\vec{r}}_i = \frac{\partial}{\partial t}(\vec{r}_i) + \vec{\omega} \times \vec{r}_i \quad (\text{A-2})$$

where $\vec{\omega} = P\hat{i} + Q\hat{j} + R\hat{k}$. Equations (A-1) and (A-2) in matrix notation for all mass points can be written as

$$\mathbf{q} = \Phi_r \mathbf{q}_r + \mathbf{q}_e \quad (\text{A-3})$$

$$\dot{\mathbf{q}} = \Phi_r \dot{\mathbf{q}}_r + \dot{\mathbf{q}}_e + \Omega(\Phi_r \mathbf{q}_r + \mathbf{q}_e) \quad (\text{A-4})$$

for

$$\Omega = \begin{bmatrix} \ddots & & \mathbf{0} \\ & \vec{\omega} & \\ \mathbf{0} & & \ddots \end{bmatrix} \quad (\text{A-5})$$

and

$$\vec{\omega} = \begin{bmatrix} 0 & -R & Q \\ R & 0 & -P \\ -Q & P & 0 \end{bmatrix} \quad (\text{A-6})$$

where \mathbf{q}_r and $\dot{\mathbf{q}}_r$ are rigid body displacement and velocity vectors, respectively, Φ_r is a rectangular matrix of the rigid body mode shapes, and \mathbf{q}_e is the elastic coordinates vector.

Kinetic Energy

Assuming that the mass matrix \mathbf{M} for the aircraft system is known, the kinetic energy (KE) of the system is given by

$$KE = \frac{1}{2} \dot{\mathbf{q}} \mathbf{M} \dot{\mathbf{q}} \quad (\text{A-7})$$

To simplify the algebra in the following development, the displacement vector \mathbf{q} and the corresponding velocity $\dot{\mathbf{q}}$ will be expressed in the generalized coordinate system, that is

$$\mathbf{q} = \begin{bmatrix} \Phi_r & \Phi_e \end{bmatrix} \begin{pmatrix} \eta_r \\ \eta_e \end{pmatrix} = \Phi \eta \quad (\text{A-8})$$

where Φ_e is a rectangular matrix of the vibration modes. The velocity vector in terms of the generalized coordinates is given by

$$\dot{\mathbf{q}} = \Phi \dot{\eta} + \Omega \Phi \eta \quad (\text{A-9})$$

Substituting equation (A-9) into (A-7) gives the kinetic energy

$$KE = \frac{1}{2} [\Phi \dot{\eta} + \Omega \Phi \eta]^T \mathbf{M} [\Phi \dot{\eta} + \Omega \Phi \eta] \quad (\text{A-10})$$

Potential Energy

If the stiffness matrix of the aircraft system is denoted by \mathbf{K} , the potential energy of the system is

$$PE = \frac{1}{2} \mathbf{q}^T \mathbf{K} \mathbf{q} = \frac{1}{2} \eta^T \Phi^T \mathbf{K} \Phi \eta \quad (\text{A-11})$$

Virtual Work

The external forces acting on the system can be classified as those dependent on the elastic deformation and the oscillatory motion of the aircraft, and those independent of the motion. The motion dependent forces are:

1. rigid body aerodynamic forces,
2. unsteady aerodynamic forces, and
3. body forces.

Motion independent forces are:

1. atmospheric gust loads and
2. engine thrust.

Rigid Body Air Loads

The computed air loads in a rigid configuration involve several parameters such as angle of attack (α), angle of sideslip (β), angular velocities P , Q , and R , and the control deflections δe , δa , and δr related to the elevator, aileron, and rudder, respectively. Since the aerodynamic forces are nonlinear functions of these parameters, a set of panel loads are computed at discrete values of these parameters and stored in a matrix array. In the analysis the air load vector for derived values of the parameters is computed by interpolation. Hence the rigid air load vector (air/rigid) symbolically is represented by

$$\mathbf{F}_{air/rigid} = \mathbf{F}(\alpha, \beta, P, Q, R, \delta e, \delta a, \delta r)$$

The virtual work done by this force is

$$VW_1 = \eta^T \Phi^T \mathbf{F}_{air/rigid} \quad (\text{A-12})$$

Unsteady Aerodynamic Forces

The aerodynamic forces arising from elastic deformation and oscillatory motion can be given by

$$\mathbf{F}_{air/flex} = \bar{q} \mathbf{A}_e(k) \mathbf{q} \quad (\text{A-13})$$

where $\mathbf{A}_e(k)$ is an influence coefficient matrix and \bar{q} is the dynamic pressure. The contribution to the virtual work from the unsteady forces is

$$\begin{aligned} VW_2 &= \bar{q} \eta^T \Phi^T \mathbf{A}_e(k) \Phi \eta \\ &= \bar{q} \eta^T [\mathbf{Q}(k)] \eta \end{aligned}$$

where $\mathbf{Q}(k)$ are the generalized forces due to η_r and η_e coordinates. As k approaches 0, $\mathbf{Q}(k)$ corresponds to the steady aerodynamic loads. However the air load due to the rigid body modes such as pitch and yaw is already included in the $\mathbf{F}_{air/rigid}$ vector. Therefore the steady air load components caused by η_r should be subtracted from $\mathbf{Q}(k)$ to give

$$\bar{\mathbf{Q}}(k) = \mathbf{Q}(k) - \begin{bmatrix} \overbrace{\mathbf{Q}(0)}^{\eta_r} & \overbrace{\mathbf{0}}^{\eta_e} \end{bmatrix} \quad (\text{A-14})$$

Then the virtual work is

$$VW_2 = \bar{q} \eta^T \bar{\mathbf{Q}}(k) \eta \quad (\text{A-15})$$

Body Forces

Let ϕ , θ , ψ be the Euler angles defining the orientation of the body-fixed axis with respect to the Earth. Then the gravity vector is

$$\vec{\mathbf{g}} = g \begin{pmatrix} -\sin \theta \\ \cos \theta \sin \phi \\ \cos \theta \cos \phi \end{pmatrix} \quad (\text{A-16})$$

The body forces are then given by

$$\mathbf{F}_{body} = \mathbf{ME} \vec{\mathbf{g}} \quad (\text{A-17})$$

where $\mathbf{E} = \begin{bmatrix} \mathbf{I}_3 \\ \mathbf{I}_3 \\ \vdots \end{bmatrix}$. The virtual work due to body forces is

$$VW_3 = \eta^T \Phi^T \mathbf{ME} \vec{\mathbf{g}} \quad (\text{A-18})$$

Gust Loads

The dynamic loads in the gust environment (discrete or random) can be computed based on the unsteady aerodynamic influence coefficients discussed earlier. The contribution to the virtual work from the gust loads is

$$VW_4 = \eta^T \Phi^T \mathbf{A}_e(k) \alpha(\omega) \mathbf{G}_{gust} \quad (\text{A-19})$$

where $\alpha(\omega)$ is an equivalent downwash computed from the gust environment and \mathbf{G}_{gust} is a measure of the gust intensity.

Engine Thrust

Future tactical fighters are expected to employ thrust vectoring to achieve superior maneuverability. Therefore the work done in more than one axis system is an important factor in the analysis of stability and maneuver performance. The virtual work contributed by the engine thrust is then

$$VW_5 = \eta^T \Phi^T \mathbf{T} \quad (\text{A-20})$$

where \mathbf{T} is a vector representing the components of the thrust at specified points.

Equations of Motion

Having defined the expressions for the energy, it is then permissible to derive the equations of motion using the Lagrangian principle, that is

$$\frac{d}{dt} \left(\frac{\partial L}{\partial \dot{\eta}} \right) - \frac{\partial L}{\partial \eta} = 0 \quad (\text{A-21})$$

where

$$L = KE - PE - VW \quad (\text{A-22})$$

in which KE is the kinetic energy given by equation (A-10), PE is the potential energy given by equation (A-11), and VW is the virtual work as the sum of the terms given by equations (A-12), (A-15), (A-18), (A-19), and (A-20). Performing the indicated differentiation with respect to each component of the generalized coordinates (η) and simplifying, the following equations of motion are obtained

$$\begin{aligned} & \Phi^T \left[\bar{q} \mathbf{F}_{air/rigid} - \underbrace{\mathbf{M} \mathbf{E} \bar{\mathbf{g}}}_{\text{body force}} + \underbrace{\mathbf{F}_T}_{\text{thrust}} - \underbrace{\bar{q} \mathbf{Q}_G \mathbf{G}_{gust}}_{\text{gust}} \right] = \\ & \left[\underbrace{\Phi^T \mathbf{M} \Phi}_{\text{general mass}} \right] \begin{pmatrix} \ddot{\eta}_r \\ \ddot{\eta}_e \end{pmatrix} + \left[\Phi^T \left(\underbrace{\mathbf{M} \boldsymbol{\Omega} + \boldsymbol{\Omega}^T \mathbf{M}}_{\text{centrifugal inertia}} \right) \Phi \right] \begin{pmatrix} \dot{\eta}_r \\ \dot{\eta}_e \end{pmatrix} \\ & + \left[\underbrace{\Phi^T \mathbf{K} \Phi}_{\text{general stiffness}} + \underbrace{\Phi^T \boldsymbol{\Omega}^T \mathbf{M} \boldsymbol{\Omega} \Phi}_{\text{inertial stiffness}} + \bar{q} \underbrace{\bar{\mathbf{Q}}(k)}_{\text{unsteady}} \right] \begin{pmatrix} \eta_r \\ \eta_e \end{pmatrix} \end{aligned} \quad (\text{A-23})$$

These equations have the same form as equation (4) in the main text for describing the structural dynamics, yet also include the additional terms to perform a nonlinear maneuver analysis. Structural damping can be included

with the velocity components. The inertial stiffness matrix given by $\Phi^T \Omega^T \mathbf{M} \Omega \Phi$ is of significant importance for the design of the feedback control system because this term contributes to the nonlinear stiffness property of the control surfaces.

The centrifugal inertia given by $\Phi^T [\mathbf{M} \Omega + \Omega^T \mathbf{M}] \Phi$ is nonlinear in angular velocities p , q , and r , and gives rise to the load factor imposed on the system. The equations of motion defined by equation (A-23) can be reduced to a first-order differential equation and solved for the state velocities. However, for performing a maneuver analysis the velocity and acceleration terms ($\dot{\eta}_e$ and $\ddot{\eta}_e$) of the elastic modes may be assumed to be small compared to the corresponding rigid body terms. The second set of equations in equation (A-23) can then be solved for η_e and substituted in the first set of equations resulting in the following equations of motion in the rigid body coordinates

$$\mathbf{M} \ddot{\eta}_r = \Gamma \left[\bar{q} \mathbf{F}_{air/rigid} - \mathbf{M} \mathbf{E} \vec{g} + \mathbf{F}_T - (\mathbf{M} \Omega + \Omega^T \mathbf{M}) \Phi_r \dot{\eta}_r \right] \quad (\text{A-24})$$

where Γ is the aeroelastic correction matrix

$$\Gamma = [\Phi_r^T + \bar{q} \mathbf{Q}_{re} \mathbf{B}^{-1} \Phi_e^T] \quad (\text{A-25})$$

in which

$$\mathbf{B} = \bar{\mathbf{K}}_{ee} - \bar{q} \mathbf{Q}_{ee} (k = 0) \quad (\text{A-26})$$

The stiffness matrix $\bar{\mathbf{K}}_{ee}$ is an effective stiffness including the centrifugal effects.

The expression given by equation (A-26) can be treated as an eigenvalue problem for the determination of the wing divergence speed (\bar{q}_{div}).

The rigid body velocity and acceleration vectors can be written as

$$\dot{\eta}_r = \begin{pmatrix} U \\ V \\ W \\ P \\ Q \\ R \end{pmatrix}$$

and

$$\ddot{\eta}_r = \begin{pmatrix} \dot{U} \\ \dot{V} \\ \dot{W} \\ \dot{P} \\ \dot{Q} \\ \dot{R} \end{pmatrix}$$

Thus equation (A-24) reduces to a first-order equation in the state velocities. For a given time history of the control variables, a transient maneuver performance of the aircraft can be determined.

If the inertia term $\mathbf{M} \ddot{\eta}_r$ is set to zero, equation (A-24) reduces to a nonlinear steady trim equation.

APPENDIX B

INERTIAL-TO-BODY-FIXED COORDINATE TRANSFORMATION

The inertial frame reference axes are used to compute the aerodynamic forces resulting from the free vibration modes of unconstrained elastic bodies. However, for stability and control analysis the preferred coordinate system is the body-fixed coordinate system. If the inertial frame and reference axes are inclined with respect to each other in a trim state through the Euler angles (Ψ, Θ, Φ) , then the velocities at the aircraft center of gravity in the inertial frame and body-fixed reference axes are related by

$$\begin{pmatrix} \dot{X} \\ \dot{Y} \\ \dot{Z} \end{pmatrix}_I = \Gamma(\Psi, \Theta, \Phi) \begin{pmatrix} U \\ V \\ W \end{pmatrix}_B$$

in which

$$\Gamma = \begin{bmatrix} \cos \Psi \cos \Theta & \cos \Psi \sin \Theta \sin \Phi - \sin \Psi \cos \Phi & \cos \Psi \sin \Theta \cos \Phi + \sin \Psi \sin \Phi \\ \sin \Psi \cos \Theta & \sin \Psi \sin \Theta \sin \Phi + \cos \Psi \cos \Phi & \sin \Psi \sin \Theta \cos \Phi - \cos \Psi \sin \Phi \\ -\sin \Theta & \cos \Theta \sin \Phi & \cos \Theta \cos \Phi \end{bmatrix}$$

Similarly, the accelerations in the inertial frame are given by

$$\begin{aligned} \begin{pmatrix} \ddot{X} \\ \ddot{Y} \\ \ddot{Z} \end{pmatrix}_I &= \Gamma(\Psi, \Theta, \Phi) \left[\begin{pmatrix} \dot{U} \\ \dot{V} \\ \dot{W} \end{pmatrix} + \Omega \begin{pmatrix} U \\ V \\ W \end{pmatrix} \right]_B \\ &= \Gamma(\Psi, \Theta, \Phi) \begin{pmatrix} A_x \\ A_y \\ A_z \end{pmatrix}_B \end{aligned}$$

where Ω is the skew-symmetric angular velocity matrix. Considering the accelerations in the body coordinate system

$$\begin{aligned} \begin{pmatrix} A_x \\ A_y \\ A_z \end{pmatrix}_B &= \begin{pmatrix} \dot{U} \\ \dot{V} \\ \dot{W} \end{pmatrix} + \Omega \begin{pmatrix} U \\ V \\ W \end{pmatrix} \\ &= \begin{pmatrix} \dot{U} \\ \dot{V} \\ \dot{W} \end{pmatrix} + \begin{bmatrix} 0 & -R & Q \\ R & 0 & -P \\ -Q & P & 0 \end{bmatrix} \begin{pmatrix} U \\ V \\ W \end{pmatrix} \\ &= \begin{pmatrix} \dot{U} \\ \dot{V} \\ \dot{W} \end{pmatrix} + \begin{bmatrix} -RV + QW \\ RU - PW \\ -QU + PV \end{bmatrix} \end{aligned}$$

Now with reference to a trim state at orientation $(\Psi_1, \Theta_1, \Phi_1)$,

$$\Phi = \Phi_1$$

$$\Theta = \Theta_1$$

$$\Psi = \Psi_1$$

$$U = U_1$$

$$V = V_1$$

$$W = W_1$$

$$P = P_1$$

$$Q = Q_1$$

$$R = R_1$$

the perturbations are

$$\begin{aligned}
\Phi &= \Phi_1 + \phi \\
\Theta &= \Theta_1 + \theta \\
\Psi &= \Psi_1 + \psi \\
U &= U_1 + u \\
V &= V_1 + v \\
W &= W_1 + w \\
P &= P_1 + p \\
Q &= Q_1 + q \\
R &= R_1 + r
\end{aligned}$$

The perturbed velocities in the inertial frame become

$$\begin{pmatrix} \dot{x} \\ \dot{y} \\ \dot{z} \end{pmatrix} = \Gamma_1 \begin{pmatrix} u \\ v \\ w \end{pmatrix} + \tilde{\Lambda}_1 \begin{pmatrix} \phi \\ \theta \\ \psi \end{pmatrix}$$

for $\Gamma_1 = \Gamma(\Psi_1, \Theta_1, \phi_1)$, and

$$\tilde{\Lambda}_1 = \begin{bmatrix} \Lambda_{x,\phi} & \Lambda_{x,\theta} & \Lambda_{x,\psi} \\ \Lambda_{y,\phi} & \Lambda_{y,\theta} & \Lambda_{y,\psi} \\ \Lambda_{z,\phi} & \Lambda_{z,\theta} & \Lambda_{z,\psi} \end{bmatrix}$$

The elements of $\tilde{\Lambda}_1$ are as follows

$$\begin{aligned}
\Lambda_{x,\phi} &= V_1(\cos \Phi_1 \sin \Theta_1 \cos \Psi_1 + \sin \Phi_1 \sin \Psi_1) \\
&\quad + W_1(\cos \Phi_1 \sin \Psi_1 - \sin \Phi_1 \sin \Theta_1 \cos \Psi_1) \\
\Lambda_{x,\theta} &= -U_1 \sin \Theta_1 \cos \Psi_1 + V_1 \sin \Phi_1 \cos \Theta_1 \cos \Psi_1 \\
&\quad + W_1 \cos \Phi_1 \cos \Theta_1 \cos \Psi_1 \\
\Lambda_{x,\psi} &= -U_1 \cos \Theta_1 \sin \Psi_1 - V_1(\sin \Phi_1 \sin \Theta_1 \sin \Psi_1 + \cos \Phi_1 \cos \Psi_1) \\
&\quad + W_1(\sin \Phi_1 \cos \Psi_1 - \cos \Phi_1 \sin \Theta_1 \sin \Psi_1) \\
\Lambda_{y,\phi} &= V_1(\cos \Phi_1 \sin \Theta_1 \sin \Psi_1 - \sin \Phi_1 \cos \Psi_1) \\
&\quad - W_1(\sin \Phi_1 \sin \Theta_1 \sin \Psi_1 + \cos \Phi_1 \cos \Psi_1) \\
\Lambda_{y,\theta} &= -U_1 \sin \Theta_1 \sin \Psi_1 + V_1 \sin \Phi_1 \cos \Theta_1 \sin \Psi_1 \\
&\quad + W_1 \cos \Phi_1 \cos \Theta_1 \sin \Psi_1 \\
\Lambda_{y,\psi} &= U_1 \cos \Theta_1 \cos \Psi_1 \\
&\quad + V_1(\sin \Phi_1 \sin \Theta_1 \cos \Psi_1 - \cos \Phi_1 \sin \Psi_1) \\
&\quad + W_1(\cos \Phi_1 \sin \Theta_1 \cos \Psi_1 + \sin \Phi_1 \sin \Psi_1) \\
\Lambda_{z,\phi} &= V_1 \cos \Phi_1 \cos \Theta_1 - W_1 \sin \Phi_1 \cos \Theta_1 \\
\Lambda_{z,\theta} &= -U_1 \cos \Theta_1 - V_1 \sin \Phi_1 \sin \Theta_1 - W_1 \cos \Phi_1 \sin \Theta_1 \\
\Lambda_{z,\psi} &= 0
\end{aligned}$$

These equations are consistent with the formulation contained in reference 15 for general reference conditions with the inertia axes initially oriented to coincide with the body axes through Γ_1 .

The body-axis perturbation accelerations are

$$\begin{pmatrix} a_x \\ a_y \\ a_z \end{pmatrix}_B = \begin{pmatrix} \dot{u} \\ \dot{v} \\ \dot{w} \end{pmatrix} + \tilde{\Omega} \begin{pmatrix} u \\ v \\ w \end{pmatrix} + \tilde{\Lambda} \begin{pmatrix} p \\ q \\ r \end{pmatrix}$$

where

$$\tilde{\Omega} = \begin{bmatrix} 0 & -R_1 & Q_1 \\ R_1 & 0 & -P_1 \\ -Q_1 & P_1 & 0 \end{bmatrix}$$

and

$$\tilde{\Lambda} = \begin{bmatrix} 0 & W_1 & -V_1 \\ -W_1 & 0 & U_1 \\ V_1 & -U_1 & 0 \end{bmatrix}$$

Perturbed accelerations in the inertial frame then become

$$\begin{aligned} \begin{pmatrix} \ddot{x} \\ \ddot{y} \\ \ddot{z} \end{pmatrix}_I &= \Gamma_1 \begin{pmatrix} a_x \\ a_y \\ a_z \end{pmatrix}_B \\ &= \Gamma_1 \begin{pmatrix} \dot{u} \\ \dot{v} \\ \dot{w} \end{pmatrix} + \Gamma_1 \tilde{\Omega} \begin{pmatrix} u \\ v \\ w \end{pmatrix} + \Gamma_1 \tilde{\Lambda} \begin{pmatrix} p \\ q \\ r \end{pmatrix} \end{aligned}$$

The state-space equations of motion in the inertial frame are given by

$$\dot{\mathbf{x}}_I = \mathbf{A}_I \mathbf{x}_I + \mathbf{B}_I \mathbf{u}$$

and the required state-space equations in the body-fixed coordinate system are obtained by the following transformations

$$\mathbf{x}_I = \mathbf{T}_1 \mathbf{x}_B$$

$$\begin{pmatrix} x \\ y \\ z \\ \phi \\ \theta \\ \psi \\ \dot{x} \\ \dot{y} \\ \dot{z} \\ \dot{\phi} \\ \dot{\theta} \\ \dot{\psi} \end{pmatrix} = \mathbf{T}_1 \begin{pmatrix} \dot{x} \\ \dot{y} \\ \dot{z} \\ \dot{\phi} \\ \dot{\theta} \\ \dot{\psi} \\ u \\ v \\ w \\ p \\ q \\ r \end{pmatrix}$$

where the primed coordinates denote inertial displacement components of the aircraft center of gravity projected onto the body coordinate system, and the relevant matrices are given as

$$\mathbf{T}_1 = \begin{bmatrix} \Gamma_1 & \mathbf{0} & \mathbf{0} & \mathbf{0} \\ \mathbf{0} & \mathbf{I} & \mathbf{0} & \mathbf{0} \\ \mathbf{0} & \tilde{\Lambda}_1 & \Gamma_1 & \mathbf{0} \\ \mathbf{0} & \tilde{\Lambda}_2 & \mathbf{0} & \Gamma_2 \end{bmatrix}$$

with

$$\Gamma_2 = \begin{bmatrix} 1 & \sin \Phi_1 \tan \Theta_1 & \cos \Phi_1 \tan \Theta_1 \\ 0 & \cos \Phi_1 & -\sin \Phi_1 \\ 0 & \frac{\sin \Phi_1}{\cos \Theta_1} & \frac{\cos \Phi_1}{\cos \Theta_1} \end{bmatrix}$$

and

$$\tilde{\Lambda}_2 = \begin{bmatrix} \dot{\Theta}_1 \tan \Theta_1 & \frac{\dot{\Psi}_1}{\cos \Theta_1} & 0 \\ -\dot{\Psi}_1 \cos \Theta_1 & 0 & 0 \\ \frac{\dot{\Theta}_1}{\cos \Theta_1} & \dot{\Psi}_1 \tan \Theta_1 & 0 \end{bmatrix}$$

Similarly for state-space velocities

$$\dot{\mathbf{x}}_I = \mathbf{T}_2 \dot{\mathbf{x}}_{B_r} + \mathbf{T}_3 \mathbf{x}_{B_r}$$

where

$$\mathbf{T}_2 = \begin{bmatrix} \Gamma_1 & \mathbf{0} & \mathbf{0} & \mathbf{0} \\ \mathbf{0} & \Gamma_2 & \mathbf{0} & \mathbf{0} \\ \Gamma_1 \tilde{\Omega} & \Gamma_1 \tilde{\Lambda} & \Gamma_1 & \mathbf{0} \\ \mathbf{0} & \mathbf{0} & \mathbf{0} & \Gamma_2 \end{bmatrix}$$

and

$$\mathbf{T}_3 = \begin{bmatrix} \mathbf{0} & \tilde{\Lambda}_1 & \mathbf{0} & \mathbf{0} \\ \mathbf{0} & \tilde{\Lambda}_2 & \mathbf{0} & \mathbf{0} \\ \mathbf{0} & \mathbf{0} & \mathbf{0} & \mathbf{0} \\ \mathbf{0} & \mathbf{0} & \mathbf{0} & \mathbf{0} \end{bmatrix}$$

In the following analysis no transformations are applied to elastic and aerodynamic lag state vectors. Thus the full-state vector transformations are given by

$$\begin{aligned} \tilde{\mathbf{T}}_1 &= \begin{bmatrix} \mathbf{T}_1 & \mathbf{0} \\ \mathbf{0} & \mathbf{I} \end{bmatrix} \\ \tilde{\mathbf{T}}_2 &= \begin{bmatrix} \mathbf{T}_2 & \mathbf{0} \\ \mathbf{0} & \mathbf{I} \end{bmatrix} \\ \tilde{\mathbf{T}}_3 &= \begin{bmatrix} \mathbf{T}_3 & \mathbf{0} \\ \mathbf{0} & \mathbf{0} \end{bmatrix} \end{aligned}$$

Then

$$\begin{aligned} \dot{\mathbf{x}}_I &= \hat{\mathbf{A}} \mathbf{x}_I + \hat{\mathbf{B}} \mathbf{u} \\ \tilde{\mathbf{T}}_2 \dot{\mathbf{x}}_B &= \hat{\mathbf{A}} \tilde{\mathbf{T}}_1 \mathbf{x}_B - \mathbf{T}_3 \mathbf{x}_B + \hat{\mathbf{B}} \mathbf{u} \\ \tilde{\mathbf{T}}_2 \dot{\mathbf{x}}_B &= (\hat{\mathbf{A}} \tilde{\mathbf{T}}_1 - \tilde{\mathbf{T}}_3) \mathbf{x}_B + \hat{\mathbf{B}} \mathbf{u} \end{aligned}$$

or

$$\begin{aligned} \dot{\mathbf{x}}_B &= \tilde{\mathbf{T}}_2^{-1} (\hat{\mathbf{A}} \tilde{\mathbf{T}}_1 - \tilde{\mathbf{T}}_3) \mathbf{x}_B + \tilde{\mathbf{T}}_2^{-1} \hat{\mathbf{B}} \mathbf{u} \\ &= \mathbf{A} \mathbf{x}_B + \mathbf{B} \mathbf{u} \end{aligned}$$

and outputs are given by

$$\begin{aligned} \mathbf{y} &= \hat{\mathbf{C}} \tilde{\mathbf{T}}_1 \mathbf{x}_B + \mathbf{D} \mathbf{u} \\ &= \mathbf{C} \mathbf{x}_B + \mathbf{D} \mathbf{u} \end{aligned}$$

APPENDIX C STABILITY DERIVATIVES

Determination of Static and Dynamic Stability Derivatives

Longitudinal Derivatives

A brief outline is given of the relations used in the evaluation of the longitudinal stability derivatives from unsteady generalized aerodynamic forces. For small perturbations of pitch rate, assuming a wings-level trim condition, ($q = \dot{\theta}$) and the rate of change of angle of attack ($\dot{\alpha}$), the lift and moment coefficients of an aircraft can be written in the Maclaurin series as

$$C_L = C_{L_0} + C_{L_\alpha} \alpha + C_{L_\alpha} \left(\frac{\dot{\alpha} \bar{c}}{2V} \right) + C_{L_q} \left(\frac{\dot{\theta} \bar{c}}{2V} \right) \dots \quad (C-1)$$

$$C_M = C_{M_0} + C_{M_\alpha} \alpha + C_{M_\alpha} \left(\frac{\dot{\alpha} \bar{c}}{2V} \right) + C_{M_q} \left(\frac{\dot{\theta} \bar{c}}{2V} \right) \dots \quad (C-2)$$

where \bar{c} is the mean aerodynamic chord and V is the flight velocity. For harmonically oscillating motion at reduced frequency k

$$\theta = \theta_0 e^{i\omega t}, \quad \frac{\dot{\theta} \bar{c}}{2V} = ik\theta \quad (C-3)$$

$$\alpha = \alpha_0 e^{i\omega t}, \quad \frac{\dot{\alpha} \bar{c}}{2V} = ik\alpha \quad (C-4)$$

Substituting equations (C-3) and (C-4) into (C-1) and (C-2) and omitting the constant terms C_{L_0} and C_{M_0} , the first-order lift and moment coefficients can be written as

$$C_L = C_{L_\alpha} \alpha + ikC_{L_\alpha} \alpha + ikC_{L_q} \theta \dots \quad (C-5)$$

$$C_M = C_{M_\alpha} \alpha + ikC_{M_\alpha} \alpha + ikC_{M_q} \theta \dots \quad (C-6)$$

For pure pitching motion ($\theta = \alpha$) and pure plunge (h)

$$C_L = \frac{Q_{h\theta}}{S} = [C_{L_\alpha} + ik(C_{L_\alpha} + C_{L_q})] \alpha \quad (C-7)$$

$$C_M = \frac{-Q_{\theta\theta}}{S} = [C_{M_\alpha} + ik(C_{M_\alpha} + C_{M_q})] \alpha \quad (C-8)$$

where S is the area of the wing and Q_{mn} is the generalized force acting on mode m due to mode n , written with respect to an inertial axis system aligned with the body axes (ref. 15) at $\alpha = 0$. The first rigid body mode is the pure plunge mode and the second is the pure pitch motion.

For a unit value of α , the stability coefficients are written as

$$C_{L_\alpha} = \frac{Re(Q_{h\theta})}{S} \dots \quad (C-9)$$

$$C_{M_\alpha} = \frac{-Re(Q_{\theta\theta})}{S} \dots \quad (C-10)$$

$$C_{L_\alpha} + C_{L_q} = \frac{Im(Q_{h\theta})}{kS} \dots \quad (C-11)$$

$$C_{M_\alpha} + C_{M_q} = \frac{-Im(Q_{\theta\theta})}{kS} \dots \quad (C-12)$$

For pure harmonic plunging motion $h = h_0 e^{i\omega t}$, the angle of attack (α) can be written as

$$\alpha = \frac{\dot{h}}{V} = ik \left(\frac{2h}{\bar{c}} \right) \dots \quad (C-13)$$

and

$$q = 0$$

then from equations (C-5) and (C-6), the lift and moment coefficients for plunging motion are given by

$$C_L = (ikC_{L_\alpha} - k^2 C_{L_\alpha}) \left(\frac{2h}{\bar{c}} \right) = -\frac{Q_{hh}}{S} \dots \quad (C-14)$$

$$C_M = (ikC_{M_\alpha} - k^2 C_{M_\alpha}) \left(\frac{2h}{\bar{c}} \right) = \frac{Q_{\theta h}}{S} \dots \quad (C-15)$$

Letting $\left(\frac{2h}{\bar{c}} \right) = 1$, the dynamic stability derivatives can be written as

$$C_{L_\alpha} = \frac{Re(Q_{hh})}{k^2 S} \quad (C-16)$$

$$C_{M_\alpha} = -\frac{Re(Q_{\theta h})}{k^2 S} \quad (C-17)$$

Finally from equations (C-11) and (C-12)

$$C_{L_q} = \frac{Im(Q_{h\theta})}{kS} - \frac{Re(Q_{hh})}{k^2 S} \quad (C-18)$$

$$C_{M_q} = -\frac{Im(Q_{\theta\theta})}{kS} + \frac{Re(Q_{\theta h})}{k^2 S} \quad (C-19)$$

Thus the six longitudinal stability derivatives can be determined from the pure plunge and pitching oscillatory motions at an infinitesimally small reduced frequency.

Lateral-Directional Derivatives

The side force, rolling moment, and yawing moment coefficients under small perturbation assumptions can be represented by

$$C_Y = C_{Y_\beta} \beta + C_{Y_\beta} \left(\frac{\dot{\beta} b}{2V} \right) + C_{Y_r} \left(\frac{rb}{2V} \right) + C_{Y_p} \left(\frac{pb}{2V} \right) \dots \quad (C-20)$$

$$C_\ell = C_{\ell_\beta} \beta + C_{\ell_\beta} \left(\frac{\dot{\beta} b}{2V} \right) + C_{\ell_r} \left(\frac{rb}{2V} \right) + C_{\ell_p} \left(\frac{pb}{2V} \right) \dots \quad (C-21)$$

$$C_n = C_{n_\beta} \beta + C_{n_\beta} \left(\frac{\dot{\beta} b}{2V} \right) + C_{n_r} \left(\frac{rb}{2V} \right) + C_{n_p} \left(\frac{pb}{2V} \right) \dots \quad (C-22)$$

As in the longitudinal case, Q_{mn} will be used to represent the generalized force acting upon mode m due to the motion of mode n . The rigid modes (y , ϕ , ψ) are orthogonal to each other. The area of the wing is S , b is the span, V the velocity, and k is a reduced frequency. The side force generated by pure yawing motion ($\beta = -\dot{\psi}$) is written as

$$\begin{aligned}
 C_Y(\psi) &= -\frac{yQ_{y\psi}\psi}{S} \\
 &= -y \left[\frac{ReQ_{y\psi}}{S}\psi + i\frac{ImQ_{y\psi}}{S}\psi \right] \\
 &= y \left[\frac{ReQ_{y\psi}}{S}(-\beta) + ik\frac{ImQ_{y\psi}}{kS}(-\beta) \right] \\
 &= y \left[\frac{ReQ_{y\psi}}{S}(-\beta) + \frac{ImQ_{y\psi}}{kS} \left(i\frac{\omega\bar{c}}{2V} \right) (-\beta) \right] \\
 &= y \left[\frac{ReQ_{y\psi}}{S}\beta + \frac{ImQ_{y\psi}}{kS} \left(\frac{\bar{c}}{b} \right) \left(\frac{\dot{\beta}b}{2V} \right) \right] \tag{C-23}
 \end{aligned}$$

Rewrite equation (C-20) as

$$\begin{aligned}
 C_Y &= C_{Y\beta}\beta + C_{Y\dot{\beta}} \left(\frac{\dot{\beta}b}{2V} \right) + C_{Y_r} \left(\frac{-\dot{\beta}b}{2V} \right) \dots \\
 &= C_{Y\beta}\beta + (C_{Y\dot{\beta}} - C_{Y_r}) \left(\frac{\dot{\beta}b}{2V} \right) \dots \tag{C-24}
 \end{aligned}$$

Comparing equations (C-23) and (C-24), for a unit value of y one obtains

$$C_{Y\beta} = \left(\frac{ReQ_{y\psi}}{S} \right) \tag{C-25}$$

and

$$C_{Y\dot{\beta}} - C_{Y_r} = \left(\frac{ImQ_{y\psi}}{kS} \right) \left(\frac{\bar{c}}{b} \right) \tag{C-26}$$

To evaluate $C_{Y\dot{\beta}}$ and C_{Y_r} , the side force due to pure harmonic lateral motion is considered, ($y = y_0 e^{i\omega t}$),

$$\beta = \frac{\dot{y}}{V} = ik \left(\frac{2y}{\bar{c}} \right) \dots \tag{C-27}$$

and

$$p = r = 0$$

then equation (C-20) becomes

$$C_Y = \left[ikC_{Y\dot{\beta}} - k^2 C_{Y\beta} \left(\frac{b}{\bar{c}} \right) \right] \left(\frac{2y}{\bar{c}} \right) = -\frac{Q_{yy}}{S} \dots \tag{C-28}$$

Let $\left(\frac{2y}{\bar{c}} \right) = 1$ to get

$$C_{Y\dot{\beta}} = \frac{Re(Q_{yy})}{k^2 S} \left(\frac{\bar{c}}{b} \right) \tag{C-29}$$

and from equation (C-26)

$$C_{Y_r} = \left[\frac{ReQ_{yy}}{k^2 S} - \frac{ImQ_{y\psi}}{kS} \right] \left(\frac{\bar{c}}{b} \right) \quad (C-30)$$

The side force generated by pure rolling motion ($p = \dot{\phi}$) is

$$\begin{aligned} C_{Y(\phi)} &= -\frac{yQ_{y\phi}}{S} \\ &= -y \left[\frac{ReQ_{y\phi}}{S} \phi + i \frac{ImQ_{y\phi}}{S} \phi \right] \\ &= -y \left[\frac{ReQ_{y\phi}}{S} \phi + ik \frac{ImQ_{y\phi}}{kS} \phi \right] \\ &= -y \left[\frac{ReQ_{y\phi}}{S} \phi + \frac{ImQ_{y\phi}}{kS} \left(i \frac{\omega \bar{c}}{2V} \right) \phi \right] \\ &= -y \left[\frac{ReQ_{y\phi}}{S} \phi + \frac{ImQ_{y\phi}}{kS} \left(\frac{\bar{c}}{b} \right) \left(\frac{\dot{\phi} b}{2V} \right) \right] \\ &= -y \frac{ImQ_{y\phi}}{kS} \left(\frac{\bar{c}}{b} \right) \left(\frac{pb}{2V} \right) \end{aligned} \quad (C-31)$$

since $ReQ_{y\phi}$ is zero. Now comparing the like term in equation (C-20), and unit y ,

$$C_{Y_p} = -\frac{ImQ_{y\phi}}{kS} \left(\frac{\bar{c}}{b} \right) \quad (C-32)$$

Hence, all four side-force derivatives are extracted from equations (C-25), (C-29), (C-30), and (C-32).

The rolling moment generated by pure yawing motion ($\beta = -\psi$) is written as

$$\begin{aligned} C_{\ell}(\psi) &= -\frac{\phi Q_{\phi\psi}}{S} \\ &= -\phi \left[\frac{ReQ_{\phi\psi}}{S} \psi + i \frac{ImQ_{\phi\psi}}{S} \psi \right] \\ &= \phi \left[\frac{ReQ_{\phi\psi}}{S} (-\beta) + ik \frac{ImQ_{\phi\psi}}{kS} (-\beta) \right] \\ &= \phi \left[\frac{ReQ_{\phi\psi}}{S} (-\beta) + \frac{ImQ_{\phi\psi}}{kS} \left(i \frac{\omega \bar{c}}{2V} \right) (-\beta) \right] \\ &= \phi \left[\frac{ReQ_{\phi\psi}}{S} \beta + \frac{ImQ_{\phi\psi}}{kS} \left(\frac{\bar{c}}{b} \right) \left(\frac{\dot{\beta} b}{2V} \right) \right] \end{aligned} \quad (C-33)$$

Rewrite equation (C-21) as

$$\begin{aligned} C_{\ell} &= C_{\ell_{\beta}} \beta + C_{\ell_{\dot{\beta}}} \left(\frac{\dot{\beta} b}{2V} \right) + C_{\ell_r} \left(\frac{-\dot{\beta} b}{2V} \right) \dots \\ &= C_{\ell_{\beta}} \beta + (C_{\ell_{\dot{\beta}}} - C_{\ell_r}) \left(\frac{\dot{\beta} b}{2V} \right) \dots \end{aligned} \quad (C-34)$$

Comparing equations (C-33) and (C-34), for ϕ one obtains

$$C_{\ell_\beta} = \left(\frac{ReQ_{\phi\psi}}{S} \right) \quad (C-35)$$

and

$$C_{\ell_\beta} - C_{\ell_r} = \left(\frac{ImQ_{\phi\psi}}{kS} \right) \left(\frac{\bar{c}}{b} \right) \quad (C-36)$$

From equation (C-27), equation (C-21) becomes

$$C_\ell = \left[ikC_{\ell_\beta} - k^2C_{\ell_\beta} \left(\frac{b}{\bar{c}} \right) \right] \left(\frac{2y}{\bar{c}} \right) = -\frac{Q_{\phi\phi}}{S} \dots \quad (C-37)$$

Let $\left(\frac{2y}{\bar{c}} \right) = 1$ to get

$$C_{\ell_\beta} = \frac{Re(Q_{\phi\phi})}{k^2S} \left(\frac{\bar{c}}{b} \right) \quad (C-38)$$

and from equation (C-36)

$$C_{\ell_r} = \left[\frac{ReQ_{\phi\phi}}{k^2S} - \frac{ImQ_{\phi\psi}}{kS} \right] \left(\frac{\bar{c}}{b} \right) \quad (C-39)$$

The rolling moment generated by pure rolling motion ($p = \dot{\phi}$) is

$$\begin{aligned} C_\ell(\phi) &= -\frac{\phi Q_{\phi\phi}}{S} \\ &= -\phi \left[\frac{ReQ_{\phi\phi}}{S} \phi + i \frac{ImQ_{\phi\psi}}{S} \phi \right] \\ &= -\phi \left[\frac{ReQ_{\phi\phi}}{S} \phi + ik \frac{ImQ_{\phi\psi}}{kS} \phi \right] \\ &= -\phi \left[\frac{ReQ_{\phi\phi}}{S} \phi + \frac{ImQ_{\phi\psi}}{kS} \left(i \frac{\omega \bar{c}}{2V} \right) \phi \right] \\ &= -\phi \left[\frac{ReQ_{\phi\phi}}{S} \phi + \frac{ImQ_{\phi\psi}}{kS} \left(\frac{\bar{c}}{b} \right) \left(\frac{\dot{\phi} b}{2V} \right) \right] \\ &= -\phi \frac{ImQ_{\phi\psi}}{kS} \left(\frac{\bar{c}}{b} \right) \left(\frac{pb}{2V} \right) \end{aligned} \quad (C-40)$$

since $ReQ_{\phi\phi}$ is zero. Now comparing the like terms in equations (C-21) and (C-40), and unit ϕ ,

$$C_{\ell_p} = -\frac{ImQ_{\phi\psi}}{kS} \left(\frac{\bar{c}}{b} \right) \quad (C-41)$$

Hence, all four rolling moment derivatives are extracted from equations (C-35), (C-38), (C-39), and (C-41).

The yawing moment generated by pure yawing motion ($\beta = -\psi$) is written as

$$\begin{aligned} C_n(\psi) &= -\frac{\psi Q_{\psi\psi}}{S} \\ &= -\psi \left[\frac{ReQ_{\psi\psi}}{S} \psi + i \frac{ImQ_{\psi\psi}}{S} \psi \right] \\ &= \psi \left[\frac{ReQ_{\psi\psi}}{S} (-\beta) + ik \frac{ImQ_{\psi\psi}}{kS} (-\beta) \right] \\ &= \psi \left[\frac{ReQ_{\psi\psi}}{S} (-\beta) + \frac{ImQ_{\psi\psi}}{kS} \left(i \frac{\omega \bar{c}}{2V} \right) (-\beta) \right] \\ &= \psi \left[\frac{ReQ_{\psi\psi}}{S} \beta + \frac{ImQ_{\psi\psi}}{kS} \left(\frac{\bar{c}}{b} \right) \left(\frac{\dot{\beta} b}{2V} \right) \right] \end{aligned} \quad (C-42)$$

Rewrite equation (C-22) as

$$\begin{aligned} C_n &= C_{n\beta}\beta + C_{n\dot{\beta}}\left(\frac{\dot{\beta}b}{2V}\right) + C_{n\ddot{\beta}}\left(\frac{-\dot{\beta}b}{2V}\right) \dots \\ &= C_{n\beta}\beta + (C_{n\dot{\beta}} - C_{n\ddot{\beta}})\left(\frac{\dot{\beta}b}{2V}\right) \dots \end{aligned} \quad (C-43)$$

Comparing equations (C-42) and (C-43), for a unit value of ψ one obtains

$$C_{n\beta} = \left(\frac{ReQ_{\psi\psi}}{S}\right) \quad (C-44)$$

and

$$C_{n\dot{\beta}} - C_{n\ddot{\beta}} = \left(\frac{ImQ_{\psi\psi}}{kS}\right)\left(\frac{\bar{c}}{b}\right) \quad (C-45)$$

Again from equation (C-27), equation (C-22) becomes

$$C_n = \left[ikC_{n\beta} - k^2C_{n\dot{\beta}}\left(\frac{b}{\bar{c}}\right) \right] \left(\frac{2y}{\bar{c}}\right) = -\frac{Q_{\psi\psi}}{S} \dots \quad (C-46)$$

Let $\left(\frac{2y}{\bar{c}}\right) = 1$ to get

$$C_{n\beta} = \frac{Re(Q_{\psi\psi})}{k^2S} \left(\frac{\bar{c}}{b}\right) \quad (C-47)$$

and from equation (C-26)

$$C_{n\dot{\beta}} = \left[\frac{ReQ_{\psi\psi}}{k^2S} - \frac{ImQ_{\psi\psi}}{kS} \right] \left(\frac{\bar{c}}{b}\right) \quad (C-48)$$

The yawing moment generated by pure rolling motion ($p = \dot{\phi}$) is

$$\begin{aligned} C_n(\phi) &= -\frac{\psi Q_{\psi\phi}\phi}{S} \\ &= -\psi \left[\frac{ReQ_{\psi\phi}}{S}\phi + i\frac{ImQ_{\psi\phi}}{S}\phi \right] \\ &= -\psi \left[\frac{ReQ_{\psi\phi}}{S}\phi + ik\frac{ImQ_{\psi\phi}}{kS}\phi \right] \\ &= -\psi \left[\frac{ReQ_{\psi\phi}}{S}\phi + \frac{ImQ_{\psi\phi}}{kS} \left(i\frac{\omega\bar{c}}{2V}\right)\phi \right] \\ &= -\psi \left[\frac{ReQ_{\psi\phi}}{S}\phi + \frac{ImQ_{\psi\phi}}{kS} \left(\frac{\bar{c}}{b}\right) \left(\frac{\dot{\phi}b}{2V}\right) \right] \\ &= -\psi \frac{ImQ_{\psi\phi}}{kS} \left(\frac{\bar{c}}{b}\right) \left(\frac{pb}{2V}\right) \end{aligned} \quad (C-49)$$

since $ReQ_{\psi\phi}$ is zero. Now comparing the like term in equation (C-22), and unit ϕ ,

$$C_{n\dot{p}} = -\frac{ImQ_{\psi\phi}}{kS} \left(\frac{\bar{c}}{b}\right) \quad (C-50)$$

Hence, all four yawing moment derivatives are extracted from equations (C-44), (C-47), (C-48), and (C-50).

Aerodynamic Derivative Representation

The relationship between airplane forces and moments in the inertial axis system and airplane stability derivatives is summarized in tables C-1 and C-2 for the longitudinal (symmetric) and lateral-directional (antisymmetric) analyses, respectively. The quantity α_1 is the trim angle of attack. Column headings designate rigid body deflection dof, and row labels represent direction of resulting air loads whether they be linear forces or angular moments caused by the deflections. The generalized forces at a very low reduced frequency ($k < 0.01$) define the generalized aerodynamic stiffness and damping matrices from which stability derivatives can be evaluated. If the derivatives are available from other sources, such as wind-tunnel or flight-test results, they may be incorporated in preference to the theoretically derived values. For coefficients pertaining to different reference points on the aircraft, corrections must be made to the derivatives (ref. 16). The inertial and body axis coordinate systems are aligned with each other at trim α_1 .

It is implicitly assumed in tables C-1 and C-2 that the derivatives are defined with reference to the body axes. Longitudinal stability coefficients defined with respect to the stability axes remain unchanged, yet lateral-directional coefficients must be adjusted as a function of angle of attack, as in table C-3, for a proper implementation into the generalized aerodynamic matrices defined in the inertial axis system.

Whether or not elastic modes are included will determine which stability derivatives (rigid or flexibilized) should be implemented into the matrices of tables C-1, C-2, or C-3. When all elastic modal dof (elastic generalized coordinates) are included in the dynamic analysis, the derivatives used should be only rigid coefficients (not flexibilized). The elastic modes included in the analysis will include the elastic increments to the rigid body derivatives through the generalized displacements at low values of reduced frequency. A rigid body analysis, without elastic modal dof, requires using the flexibilized derivatives from another source to account for elastic static deformation. No x -dof aeroelastic forces exist since the panel aerodynamics that are not perpendicular to lifting surfaces are not computed. Hence, the generalized matrix coefficients for the x -dof generalized coordinate must include the elastic increment for rigid and elastic analyses. The forces corresponding to the x -dof are therefore zero for all but the lowest reduced frequency. When a combined rigid-elastic analysis is required with a small subset of elastic modes included, such as when closed-loop roots are desired in a digital system, the rigid coefficients from another source should be used. In all analyses, the correction rigid body data is smoothed into the real and imaginary force matrices at the lowest reduced frequencies.

Flight control applications require an accurate description of stability characteristics over a frequency range dependent on the dynamics of the controller. In the STARS formulation, the three symmetric dof (x, z, θ) and three antisymmetric dof (y, ϕ, ψ) are combined to model linear six-dof motion about a reference flight condition. Various methods exist to approximate flexibilized dynamics with residual approximations when some modes are deleted from the analysis. Presently STARS can be run with all flexible modes included or some truncated, but residual stiffness or flexibility effects are not used as a reduced order approximation of elastic dynamics.

Table C-1. Stability derivative representation in the rigid-body symmetric generalized aerodynamic stiffness and damping matrix elements.

(a) Rigid body, symmetric generalized aerodynamic stiffness matrix.

	x	z	θ	δ
x	0	0	$S(C_{D_\alpha} - \alpha_1 C_{D_w} - \alpha_1 C_{L_{\alpha_1}} + \alpha_1^2 C_{L_w})$	$S(C_{D_\delta} - \alpha_1 C_{L_\delta})$
z	0	0	$S(C_{L_\alpha} - \alpha_1 C_{L_w} + \alpha_1 C_{D_\alpha} - \alpha_1^2 C_{D_w})$	$S(C_{L_\delta} + \alpha_1 C_{D_\delta})$
θ	0	0	$S\bar{c}(-C_{m_\alpha} + \alpha_1 C_{m_w})$	$-S\bar{c}C_{m_\delta}$

(b) Rigid body, symmetric generalized aerodynamic damping matrix.

	x	z	θ	δ
x	$\frac{S}{U_1}(C_{D_w} - \alpha_1 C_{L_w})$	$\frac{S}{U_1}(C_{D_\alpha} - \alpha_1 C_{L_\alpha} - C_L)$	$\frac{S\bar{c}}{2U_1}(C_{D_q} + C_{D_\alpha} - \alpha_1 C_{L_q} - \alpha_1 C_{L_{\alpha_1}})$	0
z	$\frac{S}{U_1}(C_{L_w} + \alpha_1 C_{D_w})$	$\frac{S}{U_1}(C_{L_\alpha} + \alpha_1 C_{D_\alpha})$	$\frac{S\bar{c}}{2U_1}(C_{L_q} + C_{L_\alpha} + \alpha_1 C_{D_q} + \alpha_1 C_{D_\alpha})$	0
θ	$-\frac{S}{U_1}\bar{c}C_{m_w}$	$-\frac{S}{U_1}\bar{c}C_{m_\alpha}$	$\frac{S\bar{c}}{2U_1}\bar{c}(-C_{m_q} - C_{m_\alpha})$	0

Table C-2. Body axis derivative representation in the rigid-body antisymmetric generalized aerodynamic stiffness and damping matrix elements.

(a) Rigid body, antisymmetric generalized aerodynamic stiffness matrix.

	y	ϕ	ψ	δ
y	0	$S(-C_L - \alpha_1 C_{Y_\beta})\alpha_1$	SC_{Y_β}	$-SC_{Y_\delta}$
ϕ	0	$-SbC_{\ell_\beta}\alpha_1$	SbC_{ℓ_β}	$-SbC_{\ell_\delta}$
ψ	0	$-SbC_{n_\beta}\alpha_1$	SbC_{n_β}	$-SbC_{n_\delta}$

(b) Rigid body, antisymmetric generalized aerodynamic damping matrix.

	y	ϕ	ψ	δ
y	$-\frac{S}{U_1}C_{Y_\beta}$	$\frac{Sb}{2U_1}(-C_{Y_p} - \alpha_1 C_{Y_\beta})$	$\frac{Sb}{2U_1}(-C_{Y_r} + C_{Y_\beta})$	0
ϕ	$-\frac{S}{U_1}bC_{\ell_\beta}$	$\frac{Sb}{2U_1}b(-C_{\ell_p} - C_{\ell_\beta}\alpha_1)$	$\frac{Sb}{2U_1}b(-C_{\ell_r} + C_{\ell_\beta})$	0
ψ	$-\frac{S}{U_1}bC_{n_\beta}$	$\frac{Sb}{2U_1}b(-C_{n_p} - C_{n_\beta}\alpha_1)$	$\frac{Sb}{2U_1}b(-C_{n_r} + C_{n_\beta})$	0

Table C-3. Stability axis derivative representation in the rigid-body antisymmetric generalized aerodynamic stiffness and damping matrix elements.

(a) Rigid body, antisymmetric generalized aerodynamic stiffness matrix.

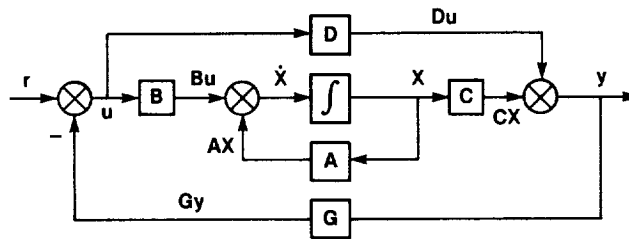
y	ϕ	ψ	δ	
y	0	$S(-C_L - \alpha_1 C_{Y_\beta}) \alpha_1$	SC_{Y_β}	$-SC_{Y_\delta}$
ϕ	0	$Sb(-C_{\ell_\beta} \cos \alpha_1 + C_{n_\beta} \sin \alpha_1) \alpha_1$	$Sb(C_{\ell_\beta} \cos \alpha_1 - C_{n_\beta} \sin \alpha_1)$	$Sb(-C_{\ell_\delta} \cos \alpha_1 + C_{n_\delta} \sin \alpha_1)$
ψ	0	$Sb(-C_{n_\beta} \cos \alpha_1 - C_{\ell_\beta} \sin \alpha_1) \alpha_1$	$Sb(C_{n_\beta} \cos \alpha_1 + C_{\ell_\beta} \sin \alpha_1)$	$Sb(-C_{n_\delta} \cos \alpha_1 - C_{\ell_\delta} \sin \alpha_1)$

(b) Rigid body, antisymmetric generalized aerodynamic damping matrix.

y	ϕ	ψ	δ	
y	$-\frac{S}{U_1} C_{Y_\beta}$	$\frac{Sb}{2U_1} (-C_{Y_p} - \alpha_1 C_{Y_\beta})$	$\frac{Sb}{2U_1} (-C_{Y_r} + C_{Y_\beta})$	0
ϕ	$\frac{S}{U_1} b (-C_{\ell_\beta} \cos \alpha_1)$ $+\frac{S}{U_1} b (C_{n_\beta} \sin \alpha_1)$	$\frac{Sb}{2U_1} b (-C_{\ell_p} \cos \alpha_1)$ $+\frac{Sb}{2U_1} b (C_{n_p} \sin \alpha_1)$ $-\frac{Sb}{2U_1} b (C_{\ell_\beta} (\cos \alpha_1) \alpha_1)$ $+\frac{Sb}{2U_1} b (C_{n_\beta} (\sin \alpha_1) \alpha_1)$	$\frac{Sb}{2U_1} b (-C_{\ell_r} \cos \alpha_1)$ $+\frac{Sb}{2U_1} b (C_{n_r} \sin \alpha_1)$ $+\frac{Sb}{2U_1} b (C_{\ell_\beta} \cos \alpha_1)$ $-\frac{Sb}{2U_1} b (C_{n_\beta} \sin \alpha_1)$	0
ψ	$\frac{S}{U_1} b (-C_{n_\beta} \cos \alpha_1)$ $-\frac{S}{U_1} b (C_{\ell_\beta} \sin \alpha_1)$	$\frac{Sb}{2U_1} b (-C_{n_p} \cos \alpha_1)$ $-\frac{Sb}{2U_1} b (C_{\ell_p} \sin \alpha_1)$ $-\frac{Sb}{2U_1} b (C_{n_\beta} (\cos \alpha_1) \alpha_1)$ $-\frac{Sb}{2U_1} b (C_{\ell_\beta} (\sin \alpha_1) \alpha_1)$	$\frac{Sb}{2U_1} b (-C_{n_r} \cos \alpha_1)$ $-\frac{Sb}{2U_1} b (C_{\ell_r} \sin \alpha_1)$ $+\frac{Sb}{2U_1} b (C_{n_\beta} \cos \alpha_1)$ $+\frac{Sb}{2U_1} b (C_{\ell_\beta} \sin \alpha_1)$	0

REFERENCES

1. Gupta, K.K., *STARS - A General-Purpose Finite Element Computer Program for Analysis of Engineering Structures*, NASA RP-1129, 1984.
2. *The NASTRAN Theoretical Manual*, NASA SP-221(06), 1981.
3. Noll, T., M. Blair, and J. Cerra, "ADAM-An Aeroservoelastic Analysis Method for Analog or Digital System," *J. Aircraft*, vol. 23, no. 11, Nov. 1986, pp. 852-858.
4. Zislin, A., E. Laurie, K. Wilkinson, and R. Goldstein, "X-29 Aeroservoelastic Analysis and Ground Test Validation Procedures," AIAA-85-3091, Oct. 1985.
5. Taylor, R.F., K.L. Miller, and R.A. Brockman, "A Procedure for Flutter Analysis of FASTOP-3 Compatible Mathematical Models, Vol. 1 - Theory and Application," AFWAL-TR81-3063, June 1981.
6. Gupta, K.K. and C.L. Lawson, "Development of a Block Lanczos Algorithm for Free Vibration Analysis of Spinning Structures," AIAA-87-0946-CP, Apr. 1987.
7. Abel, I., *An Analytical Technique for Predicting the Characteristics of a Flexible Wing Equipped with an Active Flutter-Suppression System and Comparison with Wind-Tunnel Data*, NASA TP-1367, 1979.
8. Whitbeck, R.F., D.G.J. Didaleusky, and L.G. Hofman, "Frequency Response of Digitally Controlled Systems," *J. Guidance Control*, vol. 4, no. 4, July-Aug. 1981, pp. 423-427.
9. Appa, K., "Constant Pressure Panel Method for Supersonic Unsteady Airload Analysis," *J. Aircraft*, vol. 24, no. 10, Oct. 1987, pp. 696-702.
10. Sefic, Walter J. and Cleo M. Maxwell, *X-29A Technology Demonstrator Flight Test Program Overview*, NASA TM-86809, 1986.
11. Whitaker, A. and J. Chin, "X-29 Digital Flight Control System Design," AGARD-CP-384, Active Control Systems - Review, Evaluation, and Projections, Oct. 1984.
12. Gupta, K.K., *STARS - An Integrated General Purpose Finite Element Structural, Aeroelastic, and Aeroservoelastic Analysis Computer Program*, NASA TM-101709, 1990.
13. Waszak, Martin R. and David K. Schmidt, "On the Flight Dynamics of Aeroelastic Vehicles," AIAA-86-2077, 1986.
14. Gera, Joseph and John T. Bosworth, *Dynamic Stability and Handling Qualities Tests on a Highly Augmented, Statically Unstable Airplane*, NASA TM-88297, 1987.
15. Miller, R.D., R.J. Fraser, M.Y. Hirayama, and R.E. Clemmons, *Equation Modifying Program L219 (EQMOD), Vol. 1: Engineering and Usage*, NASA CR-2855, 1979.



Summing junction outputs

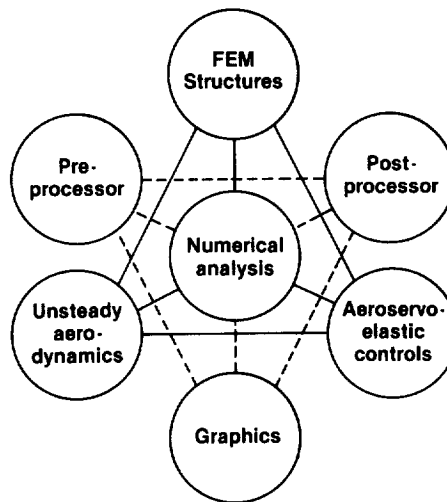
$$u = r - Gy$$

$$\dot{X} = AX + Bu$$

$$y = CX + Du$$

7005

Figure 1. Feedback control system.



Finite element modeling
 Spinning structures
 Mechanical and thermal loading
 General and composite materials

Preprocessor – automatic FEM
 model data generation
 Postprocessor – graphical
 depiction of analysis results

Statics
 Buckling
 Vibration
 Dynamic responses

Aeroelasticity
 Flutter and divergence

Aeroservoelasticity
 Frequency responses, digital
 and analog controllers
 Damping and frequencies

Hydrodynamics

7003

Figure 2. Major modules and capabilities of STARS.

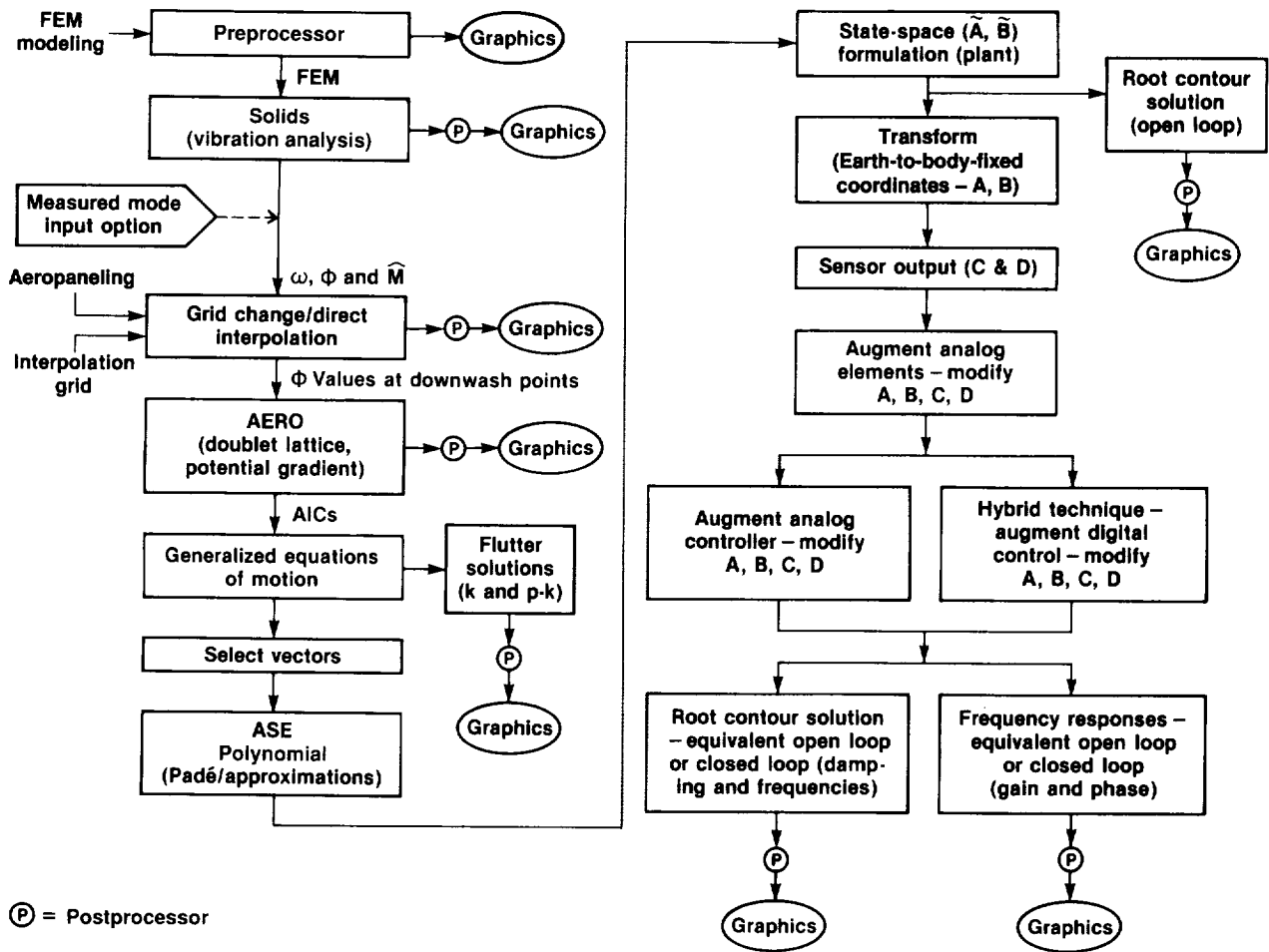
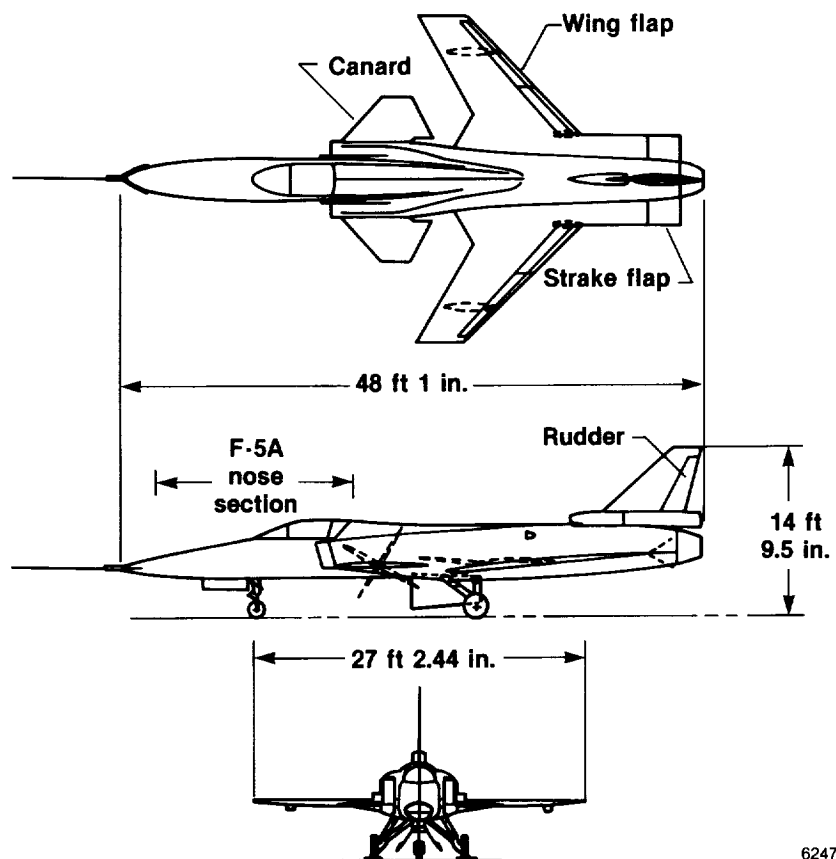


Figure 3. STARS aeroservoelastic analysis flow chart.

9398



6247

Figure 4. X-29A aircraft.

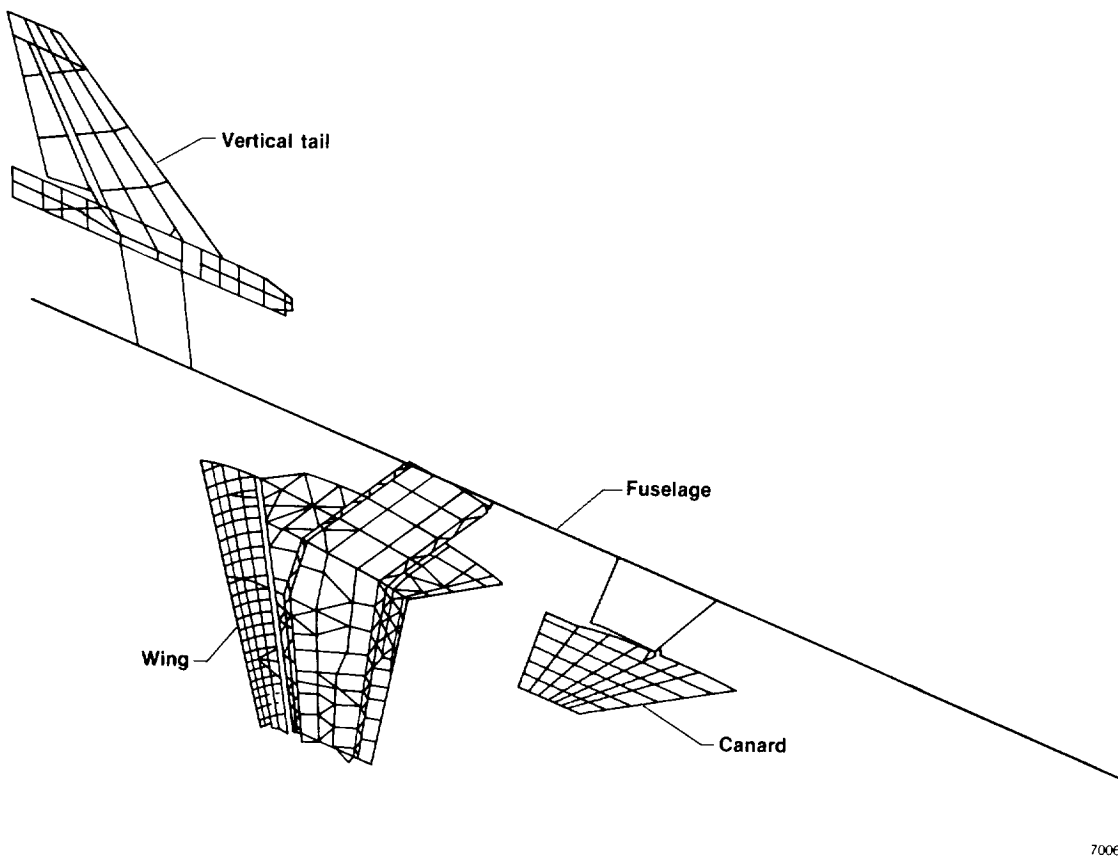


Figure 5. Finite-element dynamics model of symmetric half of X-29A aircraft.

7006

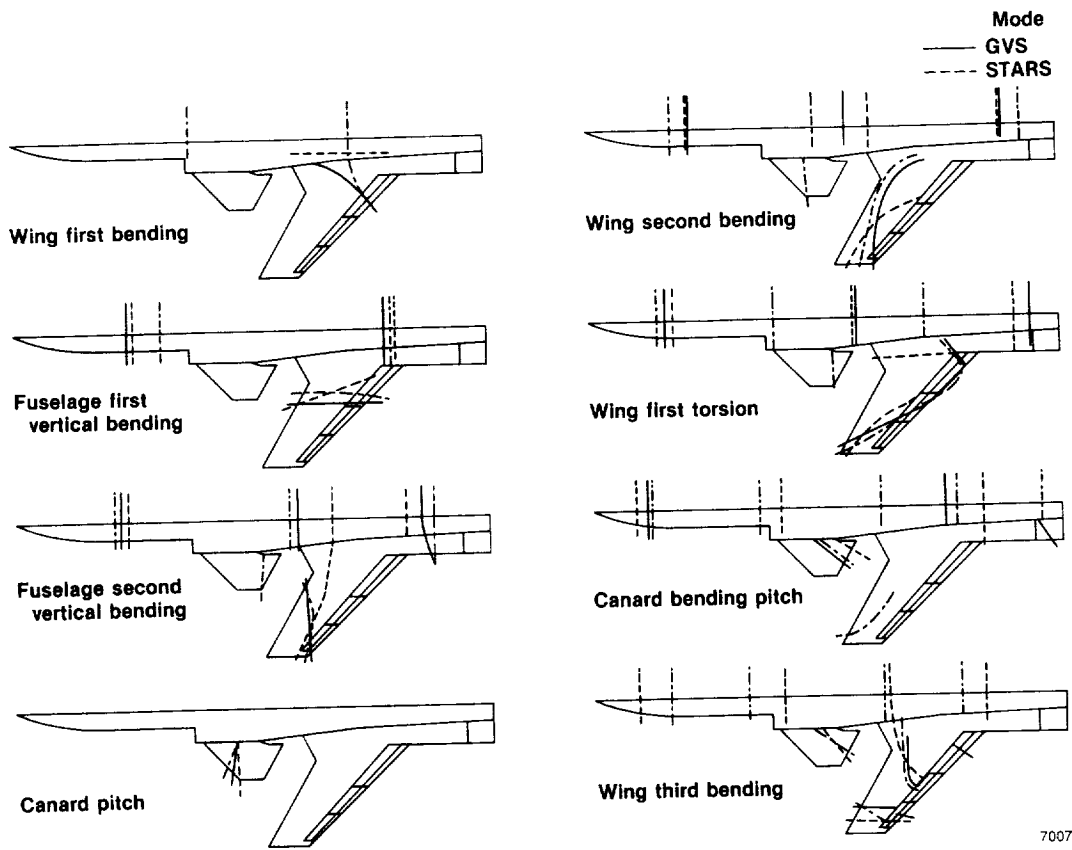
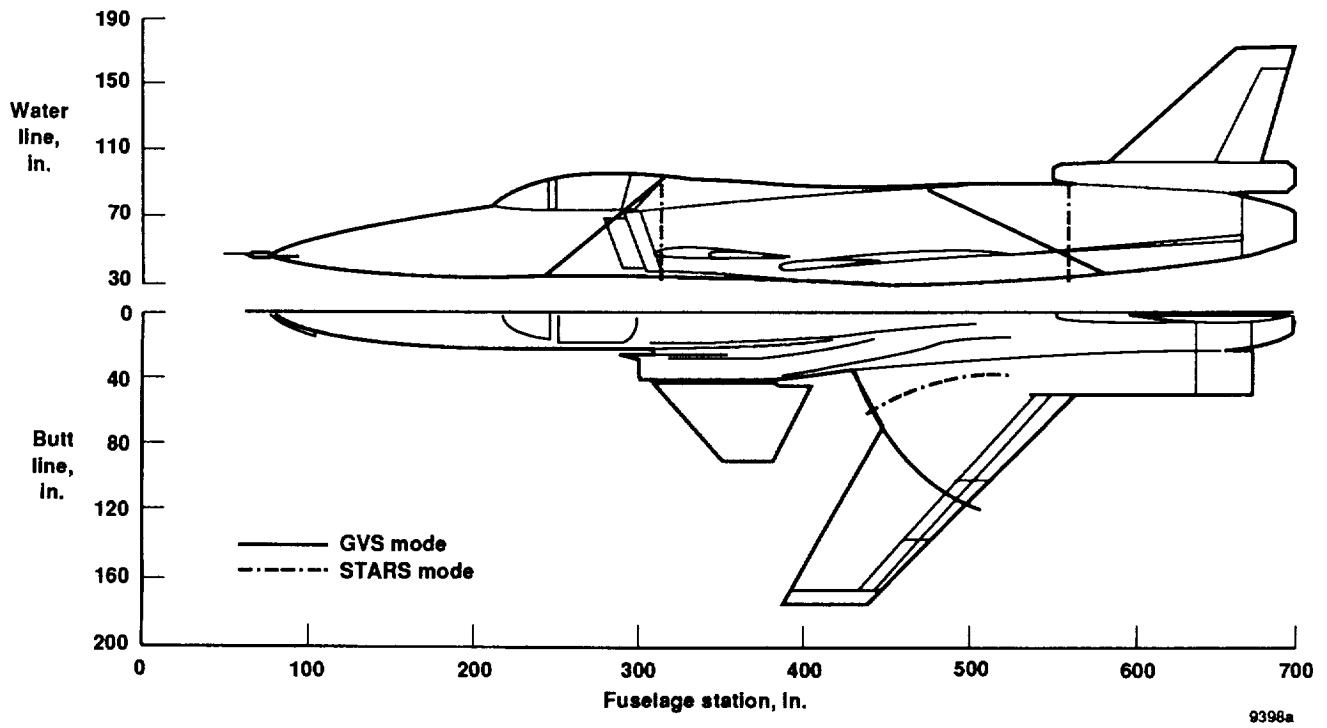
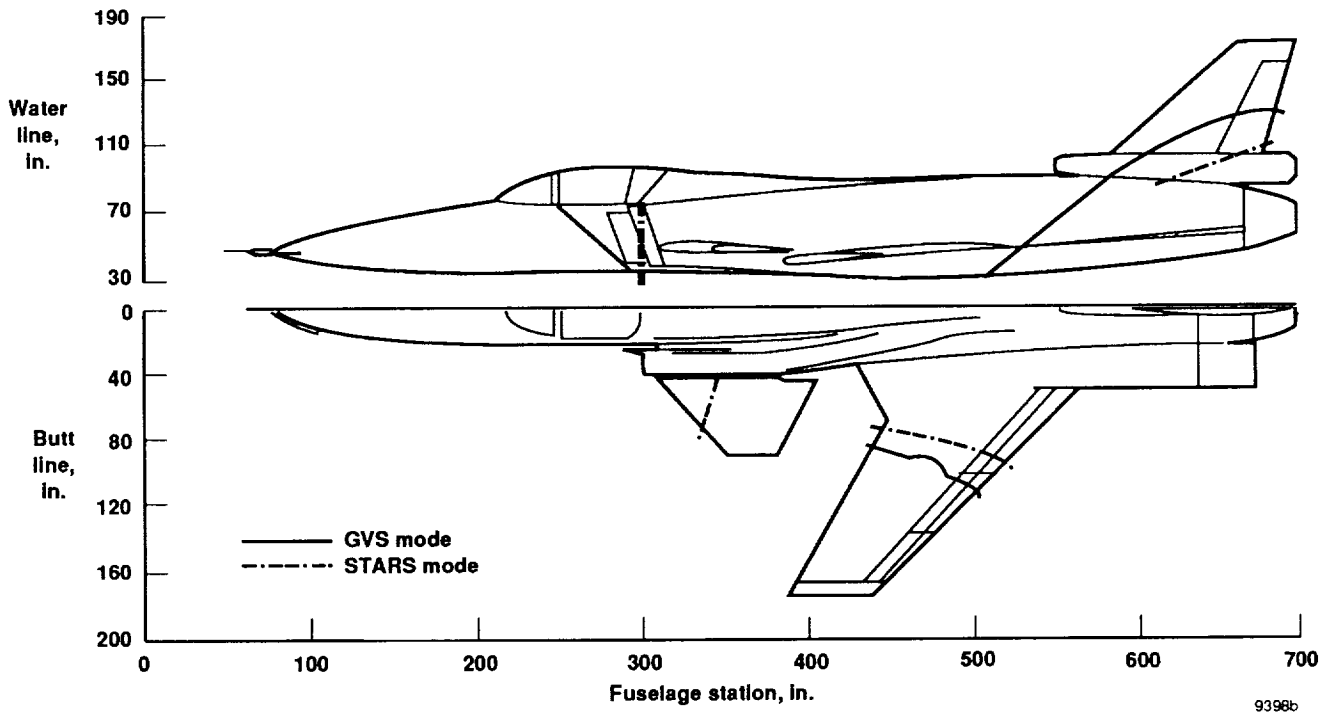


Figure 6. Node line comparisons for GVS and STARS analyses for various modes for the X-29A aircraft, symmetric case.



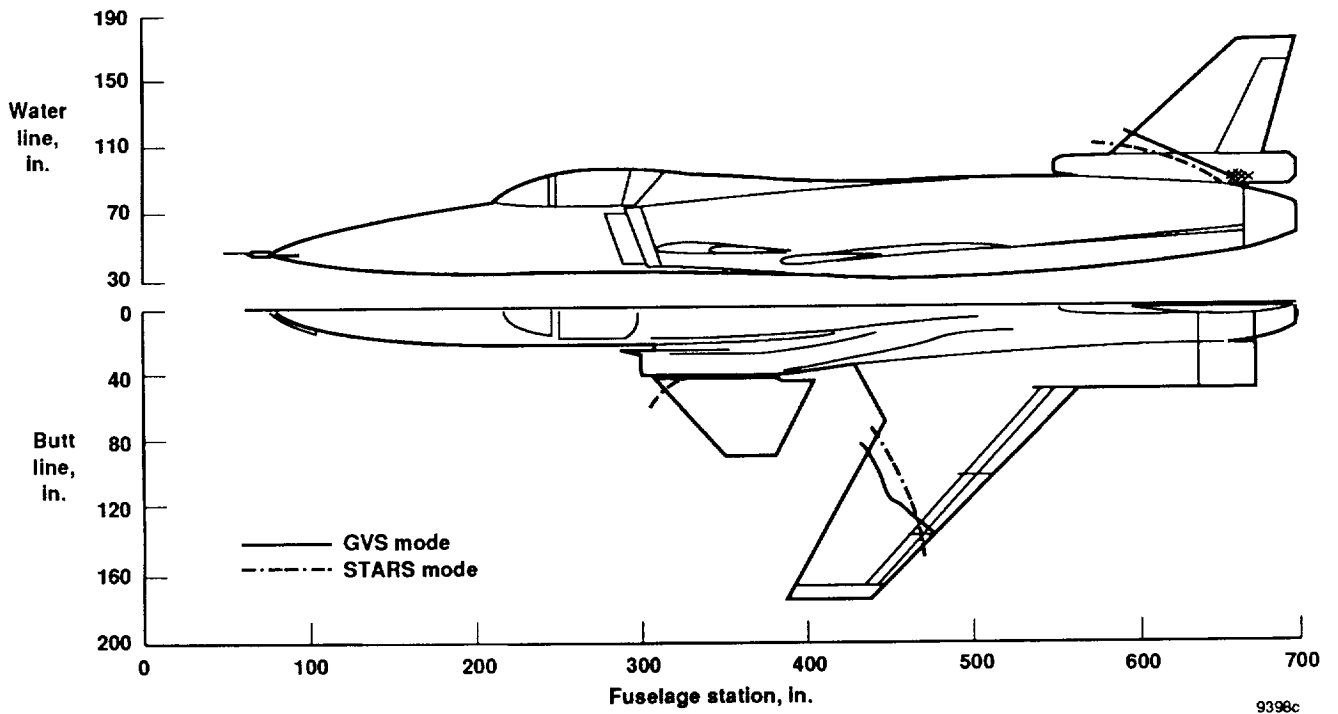
(a)

Figure 7. X-29A aircraft antisymmetric case node line comparisons between GVS and STARS analyses.



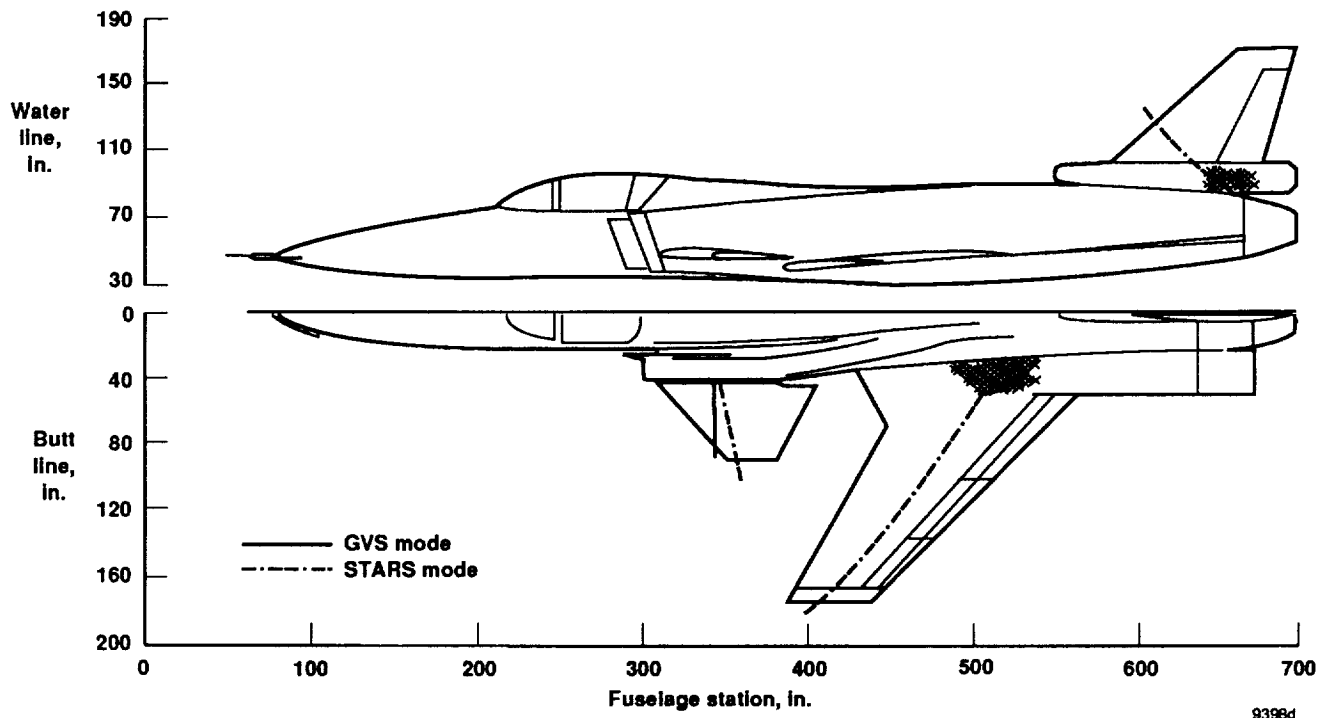
(b)

Figure 7. Continued.



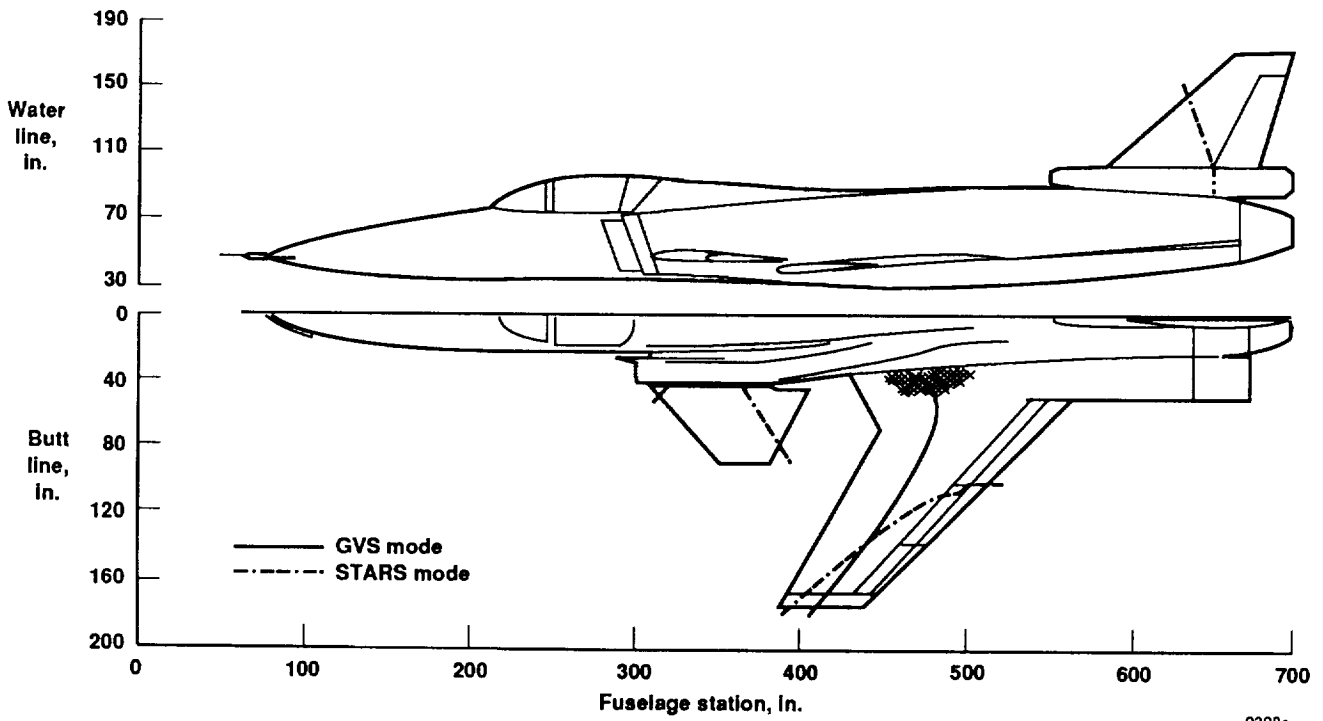
(c)

Figure 7. Continued.



(d)

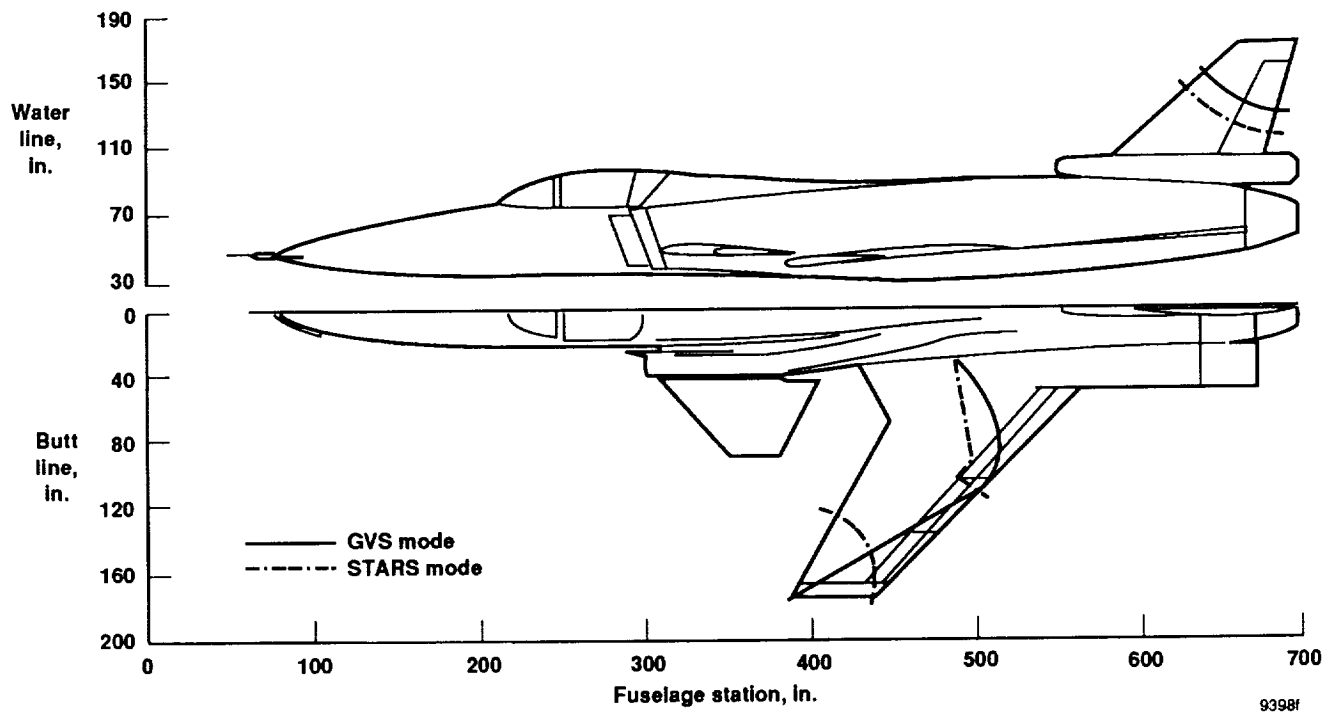
Figure 7. Continued.



9398e

(e)

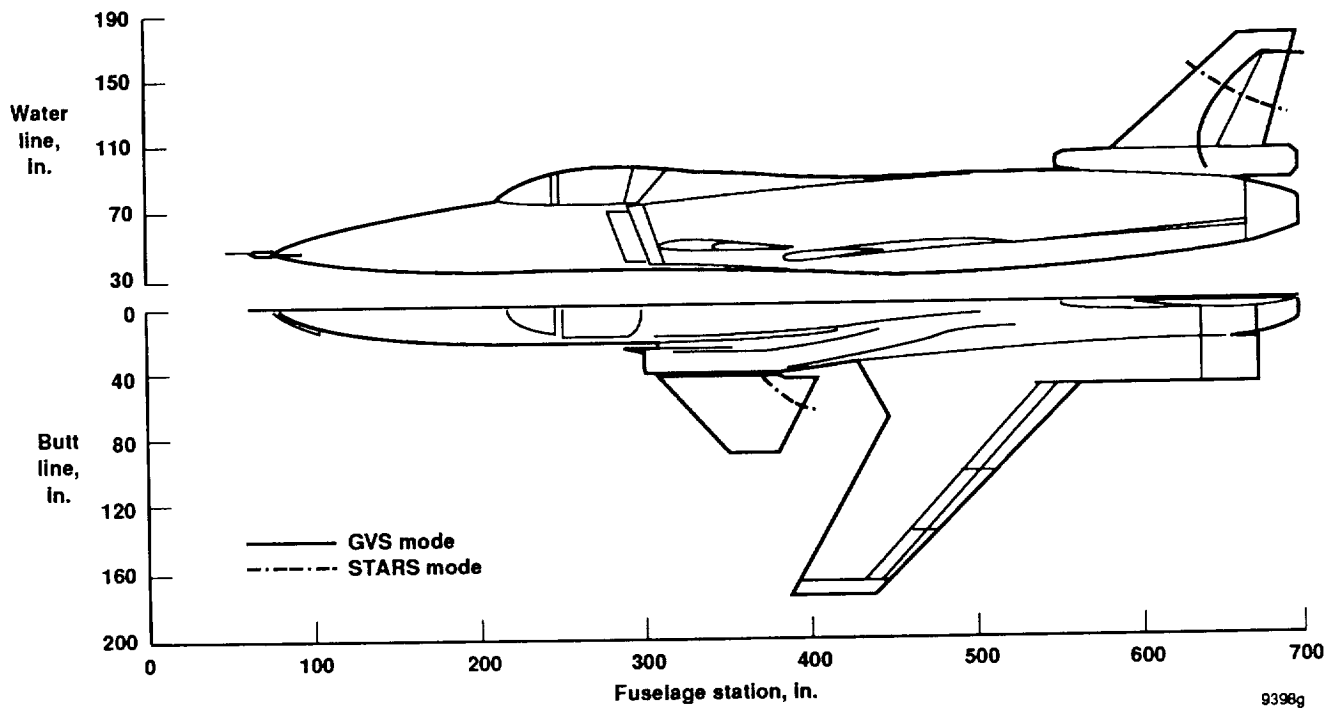
Figure 7. Continued.



9398f

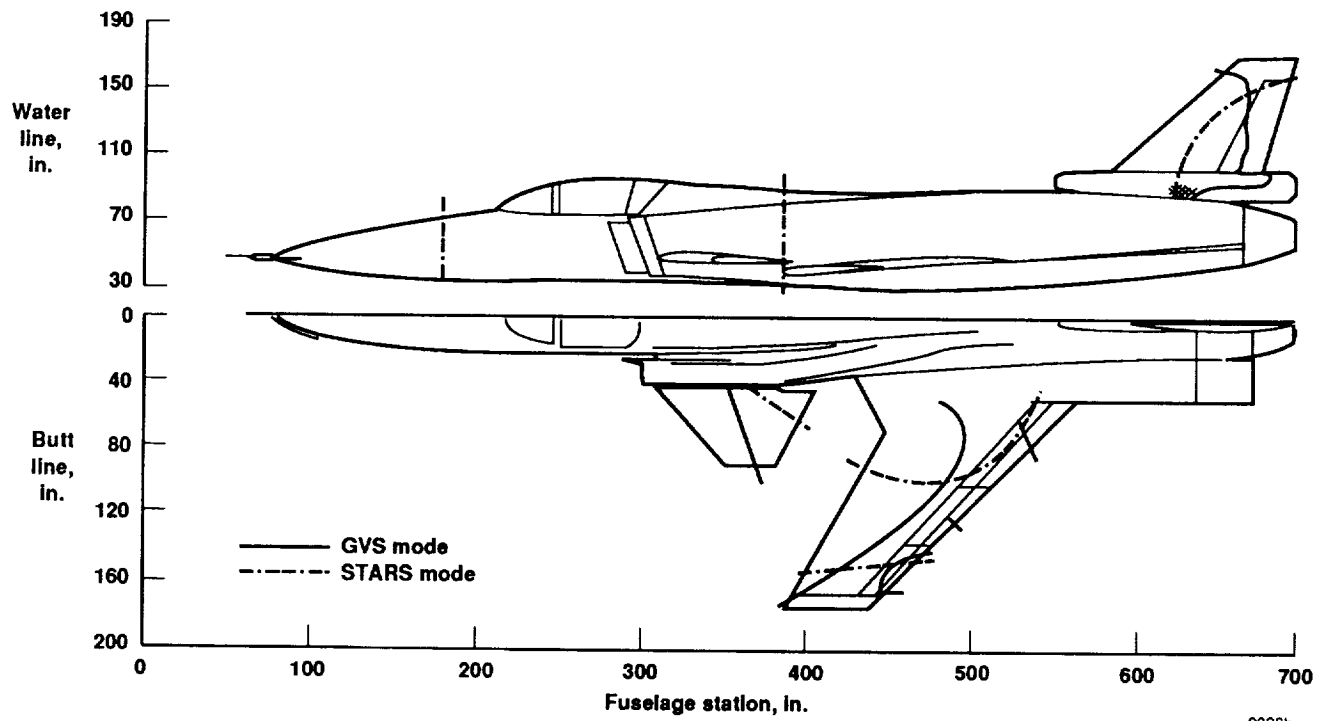
(f)

Figure 7. Continued.



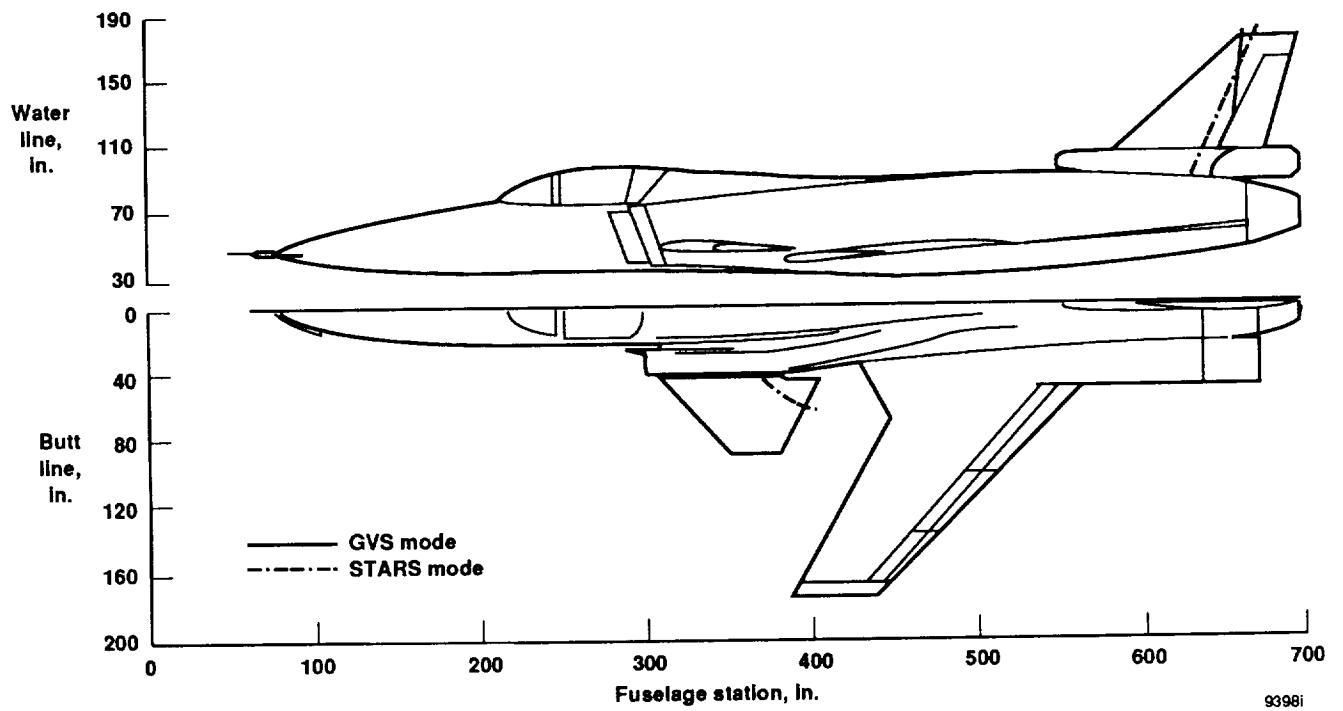
(g)

Figure 7. Continued.



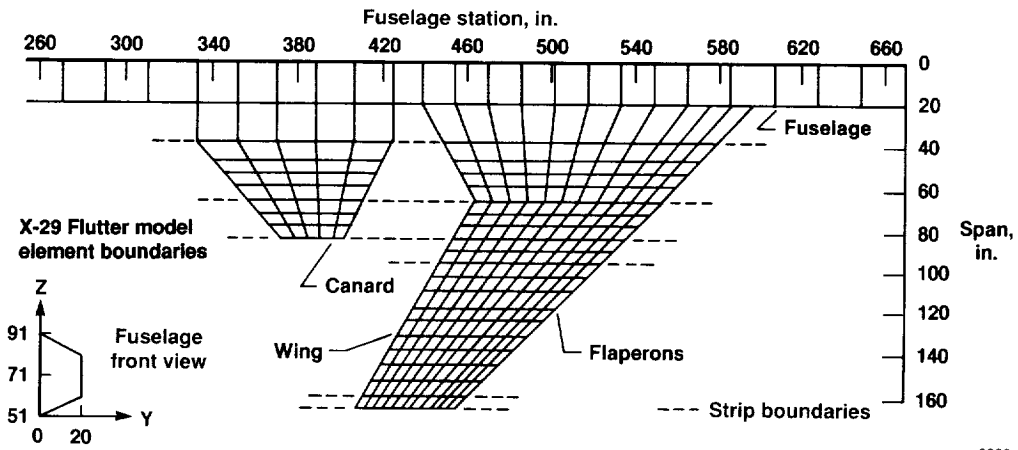
(h)

Figure 7. Continued.



(i)

Figure 7. Concluded.



9399

Figure 8. Unsteady aerodynamic paneling idealization (DLM and CPM).

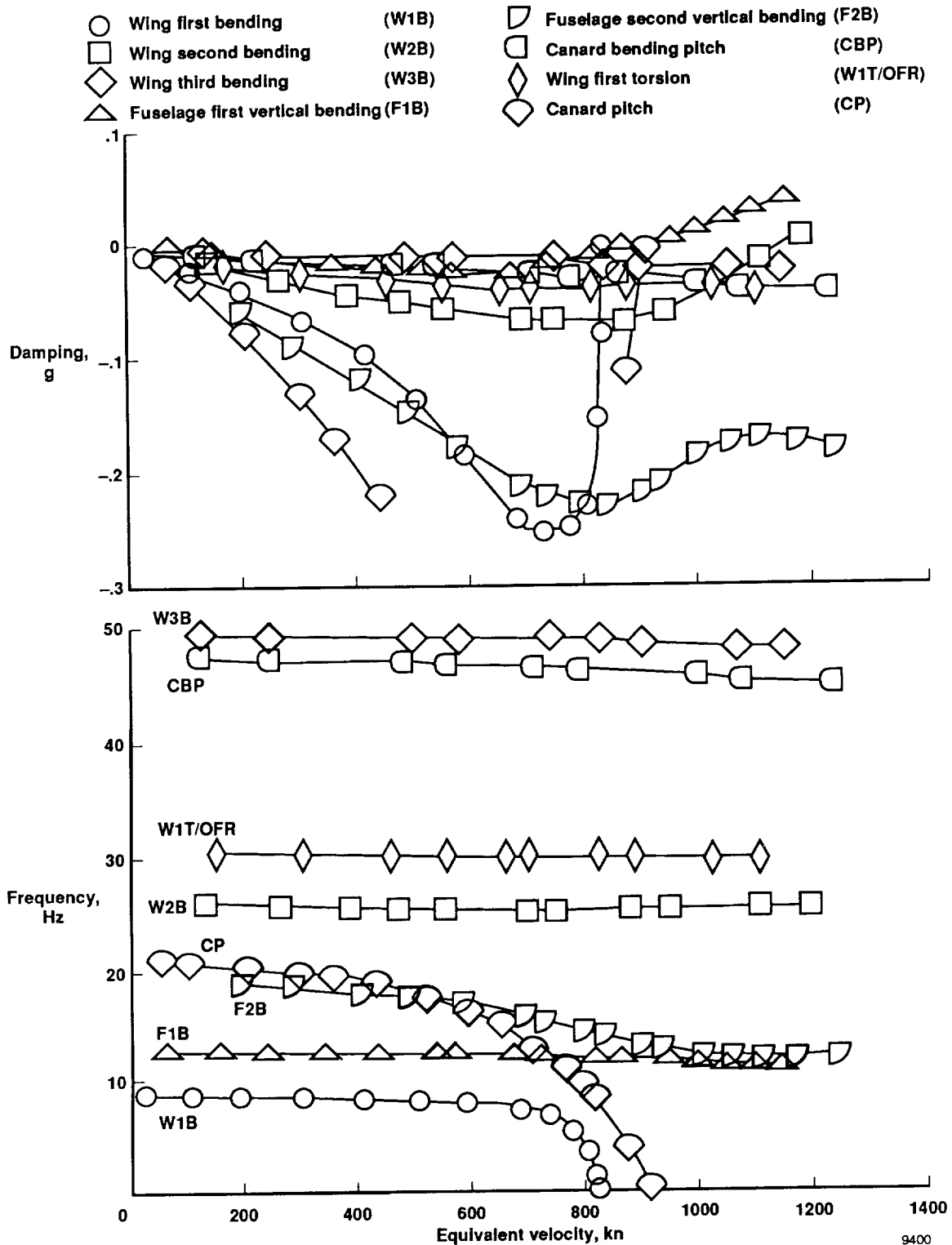


Figure 9. X-29A aircraft flutter solution plots using STARS calculated modal data (symmetric case).

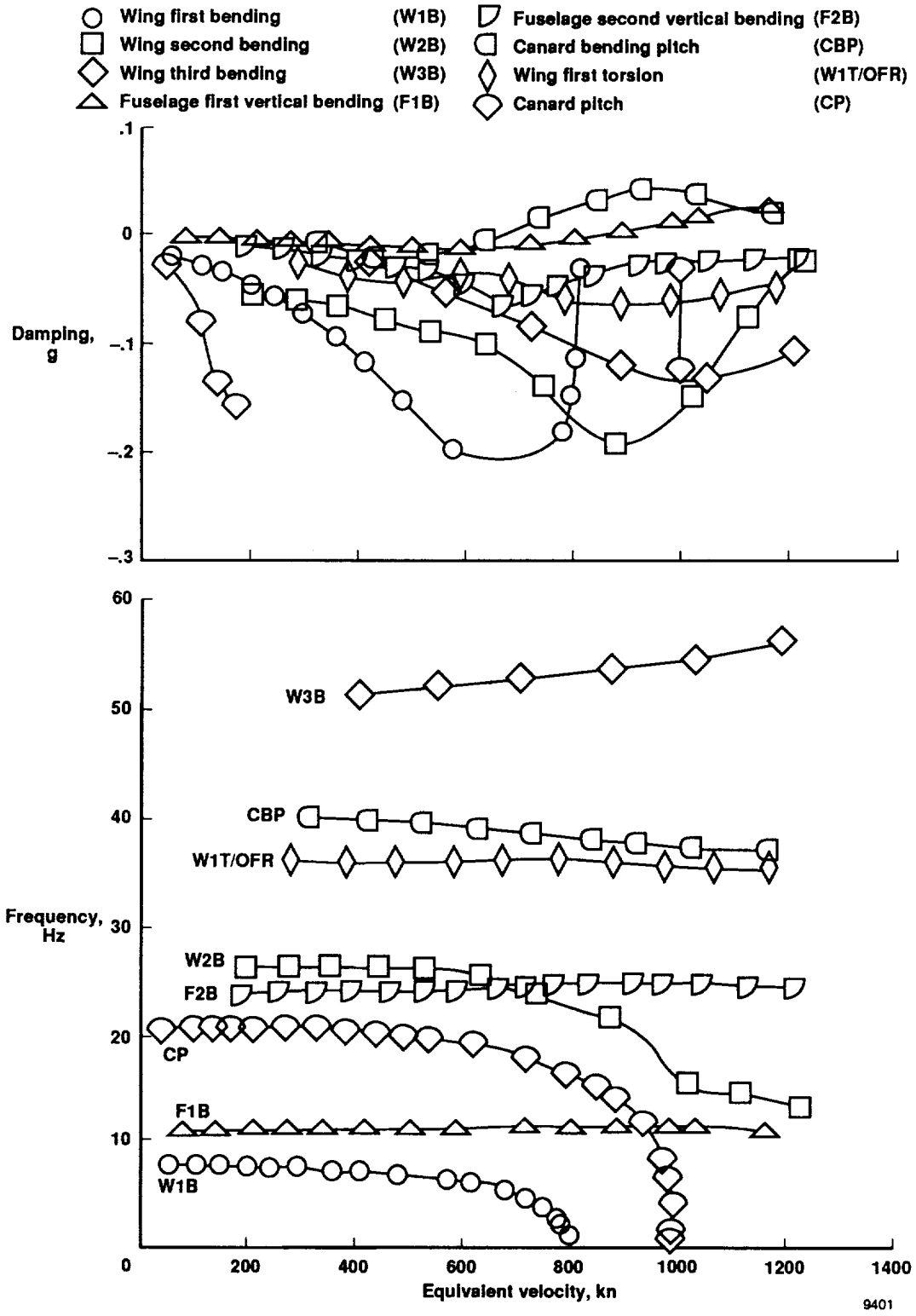


Figure 10. X-29A aircraft flutter solution plots using GVS measured modal data (symmetric case).

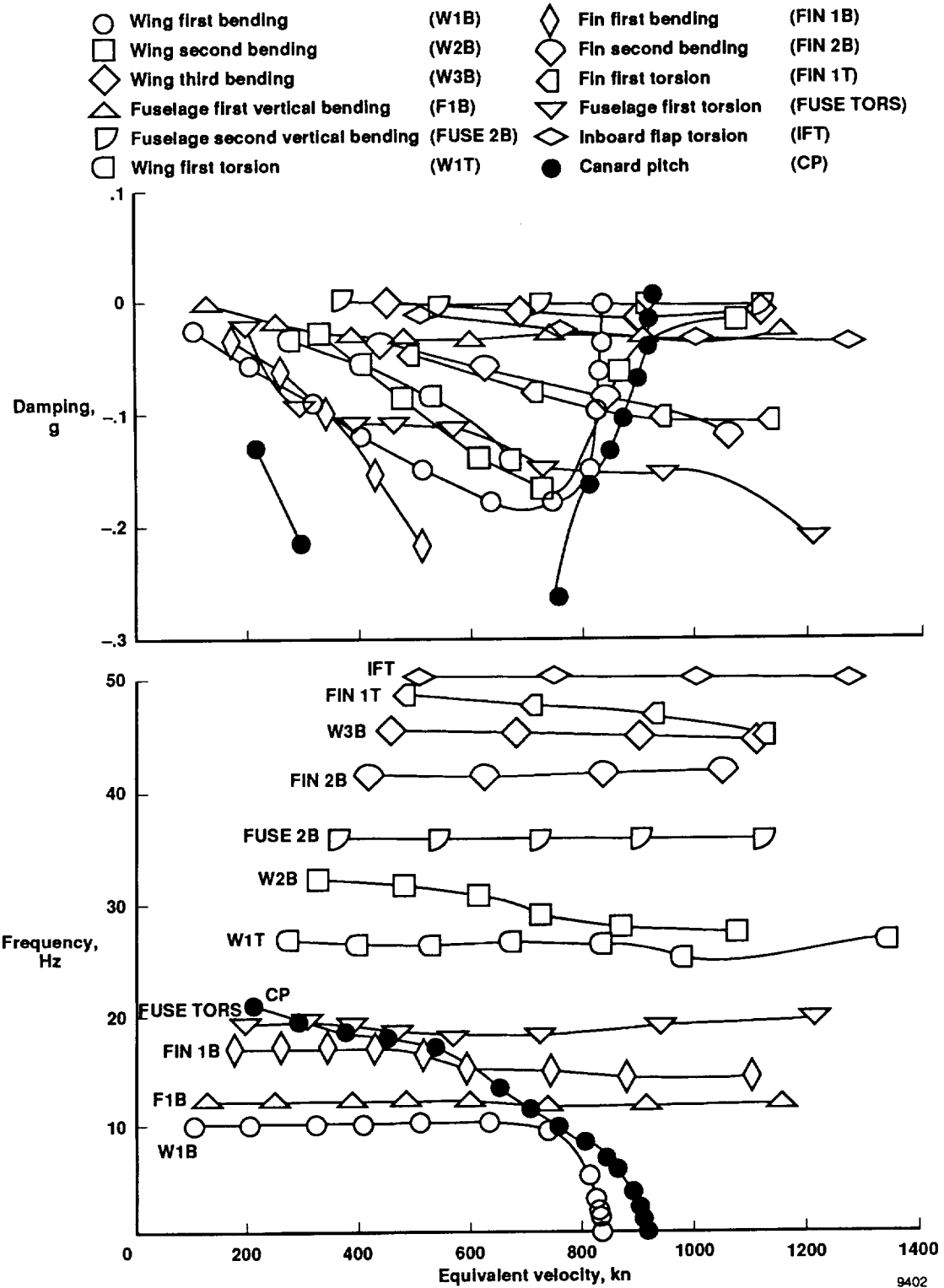


Figure 11. X-29A aircraft flutter solution plots using STARS calculated modal data (antisymmetric case).

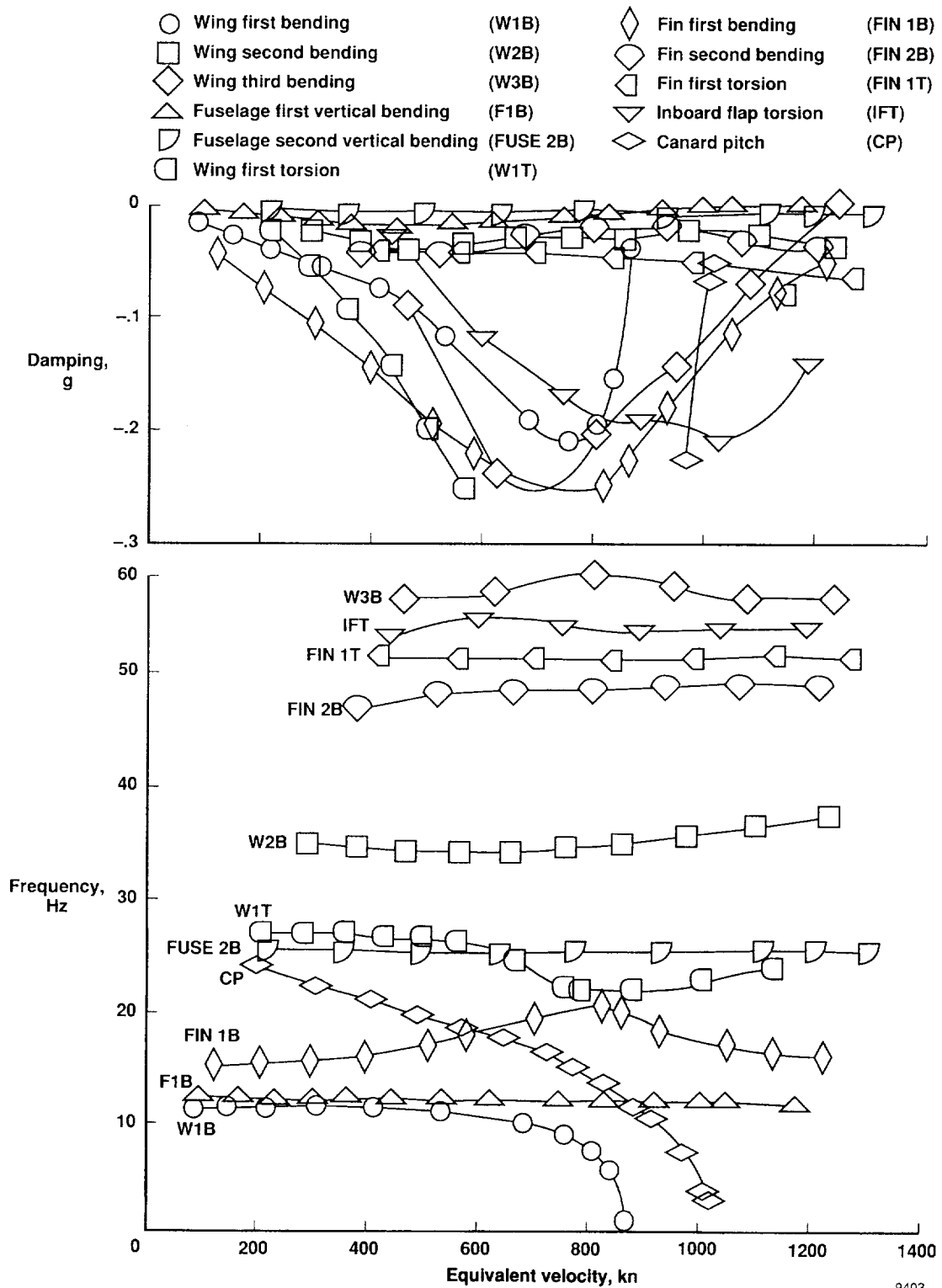


Figure 12. X-29A aircraft flutter solution plots using GVS measured modal data (antisymmetric case).

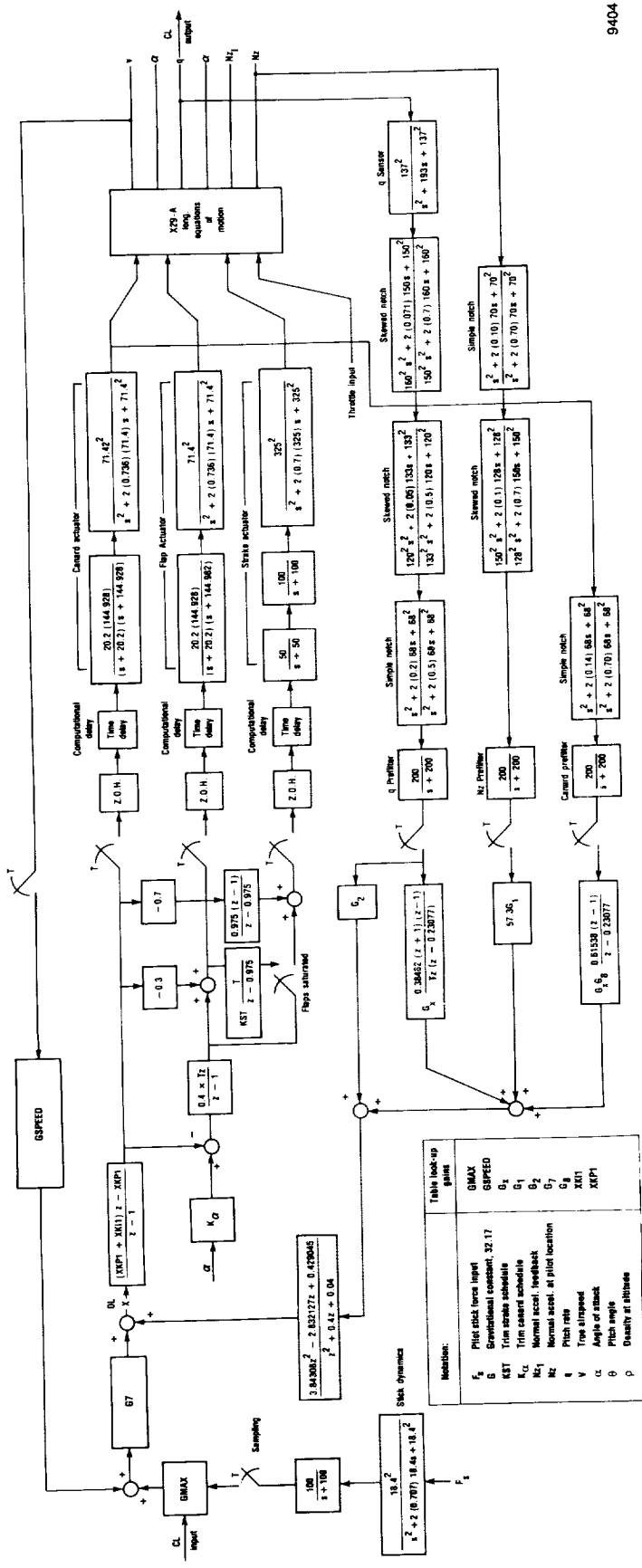


Figure 13. Longitudinal normal digital mode control law block diagram for X-29A.

9404

Table look-up gains	
GMAX	GSPEED
G1	G1
G2	G2
G7	G7
G8	G8
XK1	XK1
XRP1	XRP1

Notations:	
F_s	Pilot stick force input
G	Gravitational constant, 32.17
GSPEED	Trim airspeed schedule
KST	Trim airspeed schedule
KCL	Normal accel. feedback
Nz1	Normal accel. at pilot location
Nz	Pitch rate
v	Trim airspeed
O	Angle of attack
theta	Pitch angle
p	Quasi-stiffness

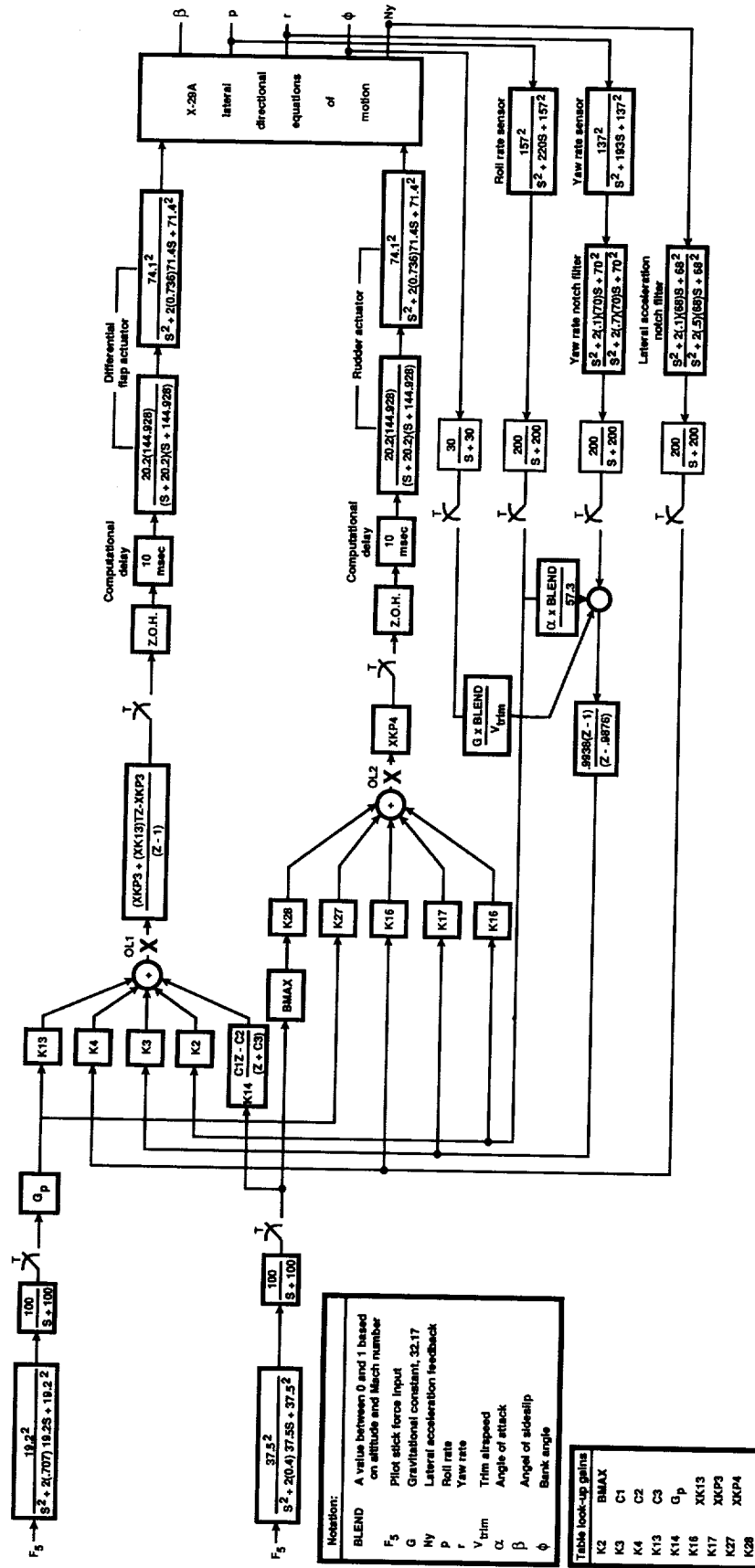
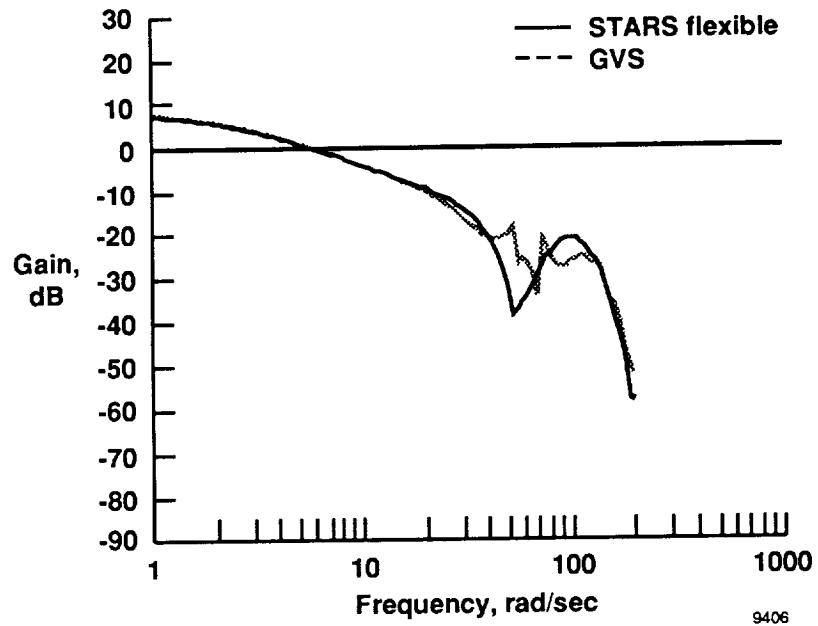
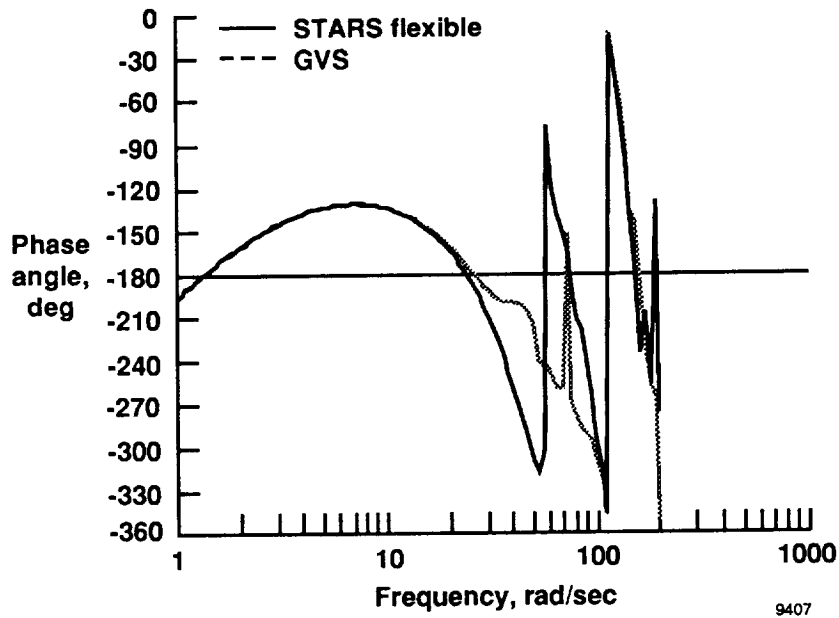


Figure 14. Lateral-directional normal digital mode control law block diagram for X-29A.

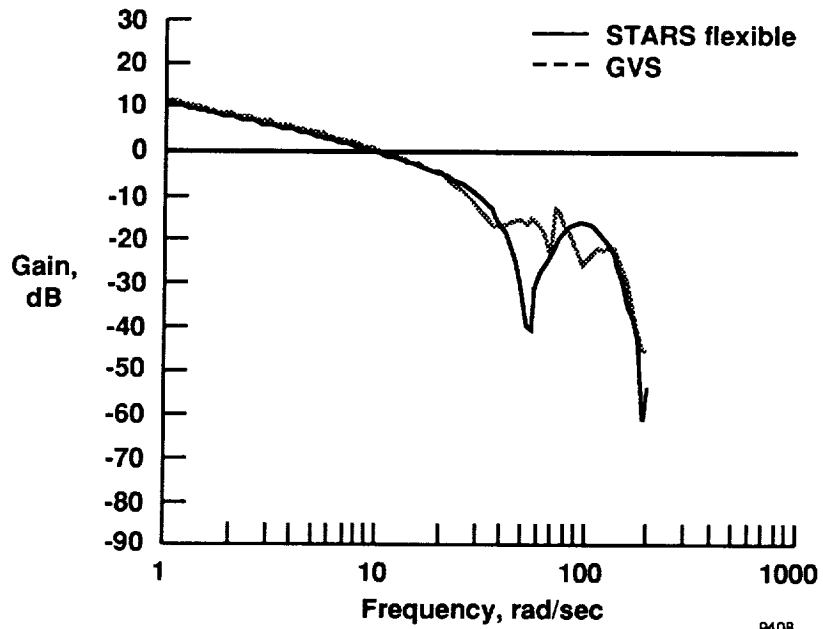


(a) Gain, dB.

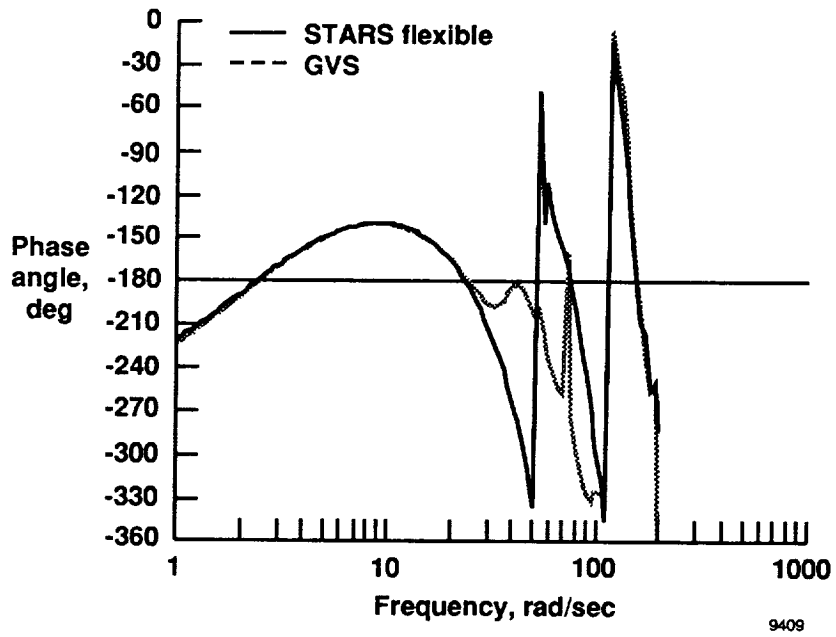


(b) Phase angle, deg.

Figure 15. Longitudinal loop gains computed with GVS and STARS models for flight condition 1.

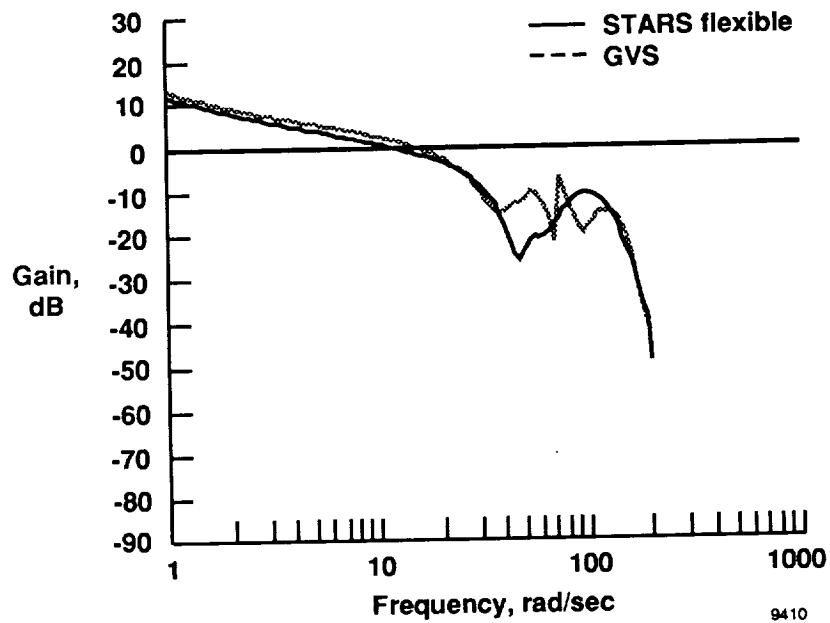


(a) Gain, dB.

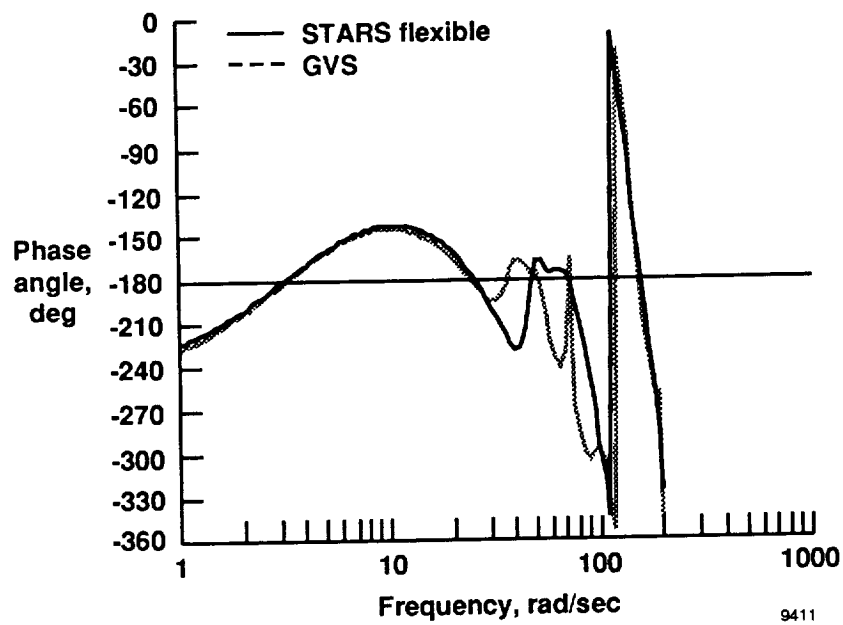


(b) Phase angle, deg.

Figure 16. Longitudinal loop gains computed with GVS and STARS models for flight condition 2.

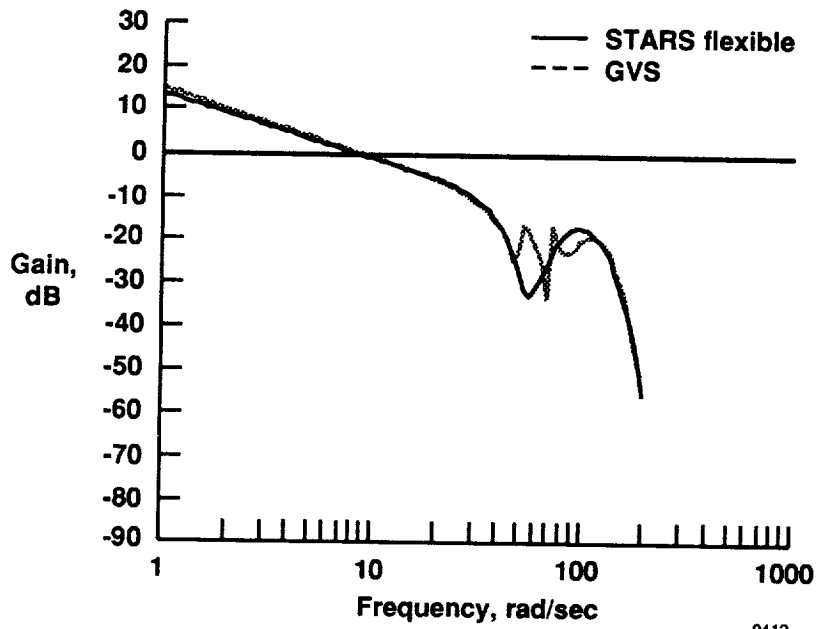


(a) Gain, dB.

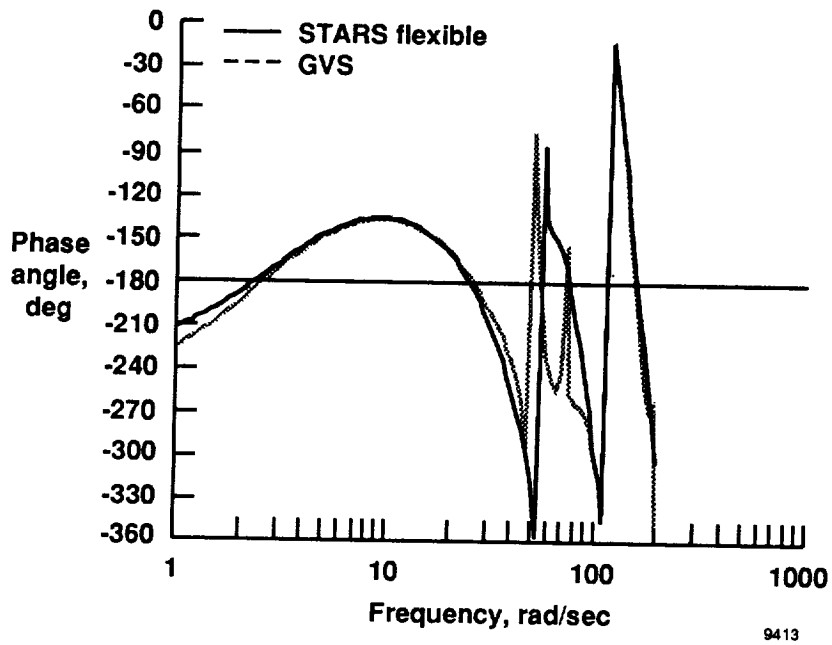


(b) Phase angle, deg.

Figure 17. Longitudinal loop gains computed with GVS and STARS models for flight condition 3.

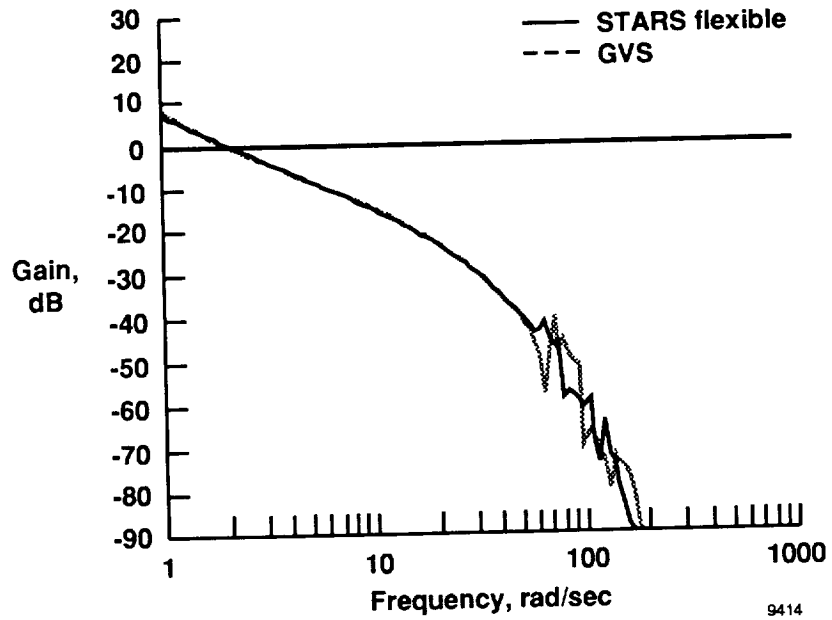


(a) Gain, dB.

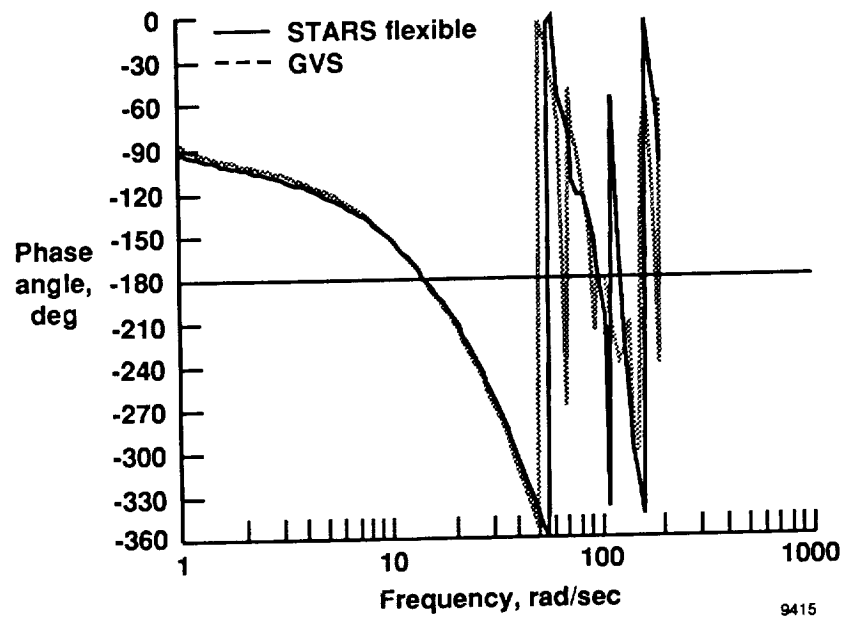


(b) Phase angle, deg.

Figure 18. Longitudinal loop gains computed with GVS and STARS models for flight condition 4.

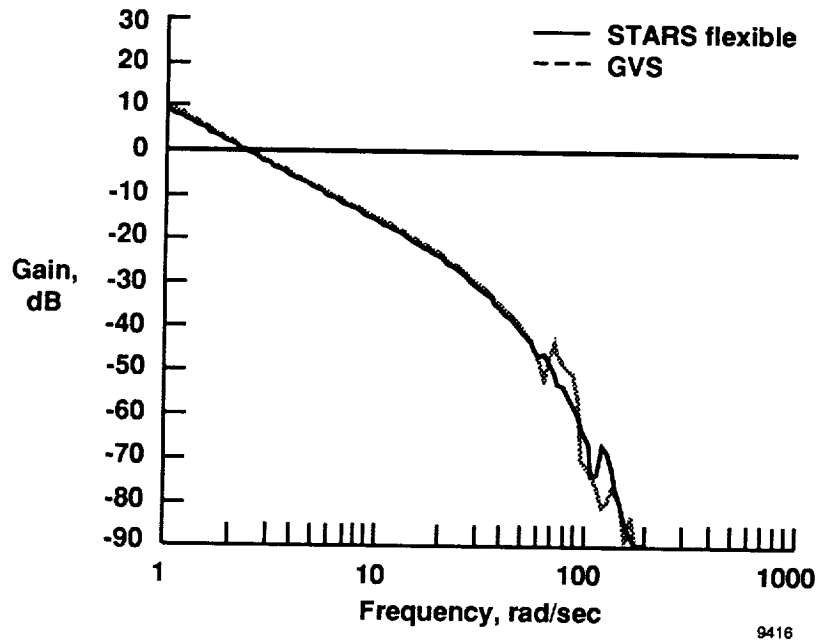


(a) Gain, dB.

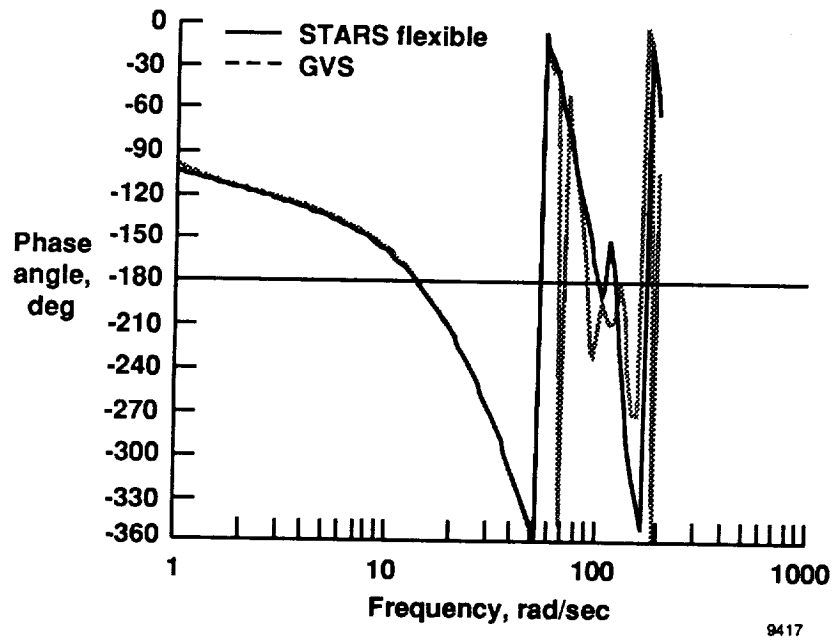


(b) Phase angle, deg.

Figure 19. Lateral loop gains computed with GVS and STARS models for flight condition 1.

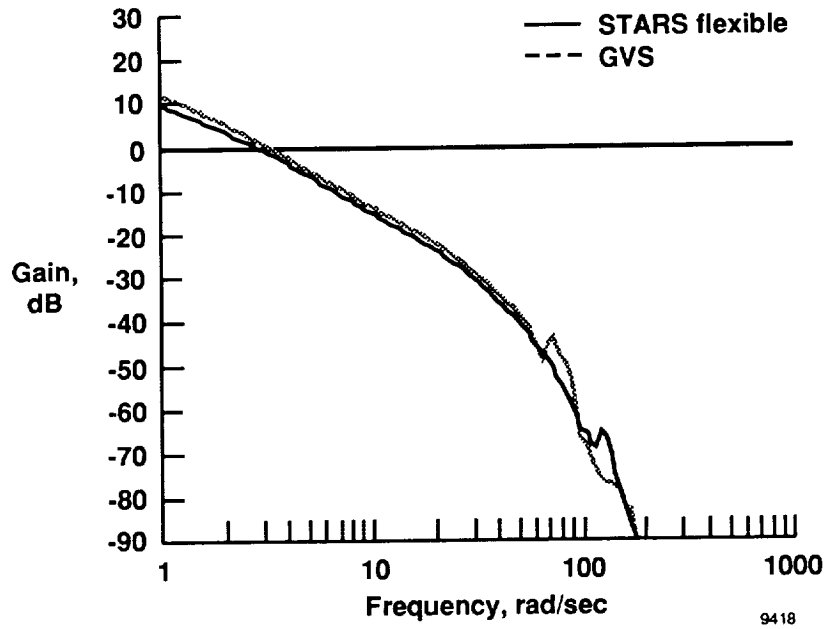


(a) Gain, dB.

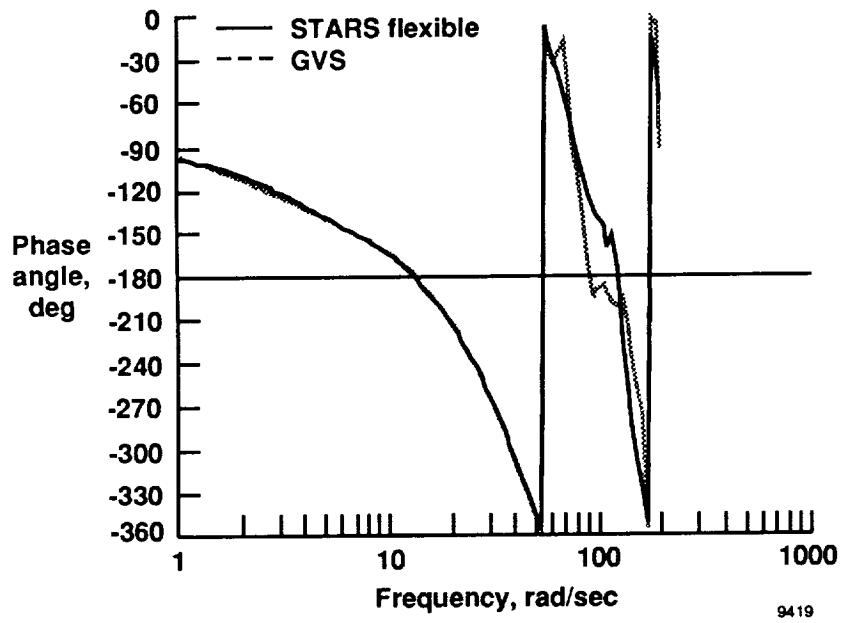


(b) Phase angle, deg.

Figure 20. Lateral loop gains computed with GVS and STARS models for flight condition 2.

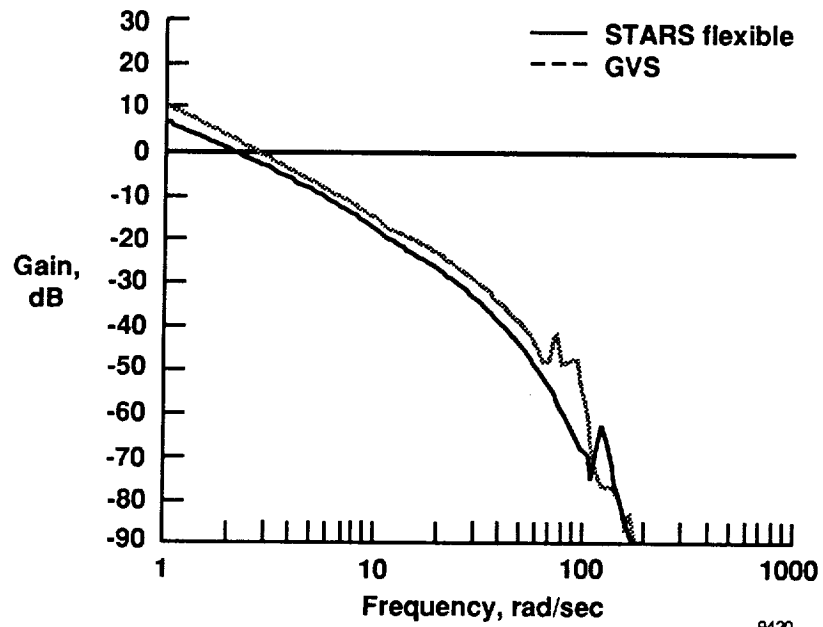


(a) Gain, dB.

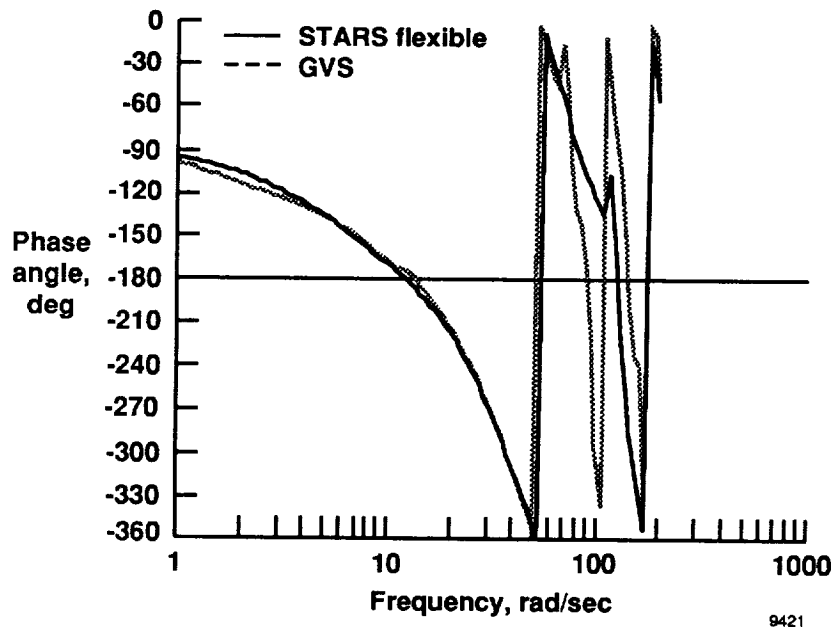


(b) Phase angle, deg.

Figure 21. Lateral loop gains computed with GVS and STARS models for flight condition 3.

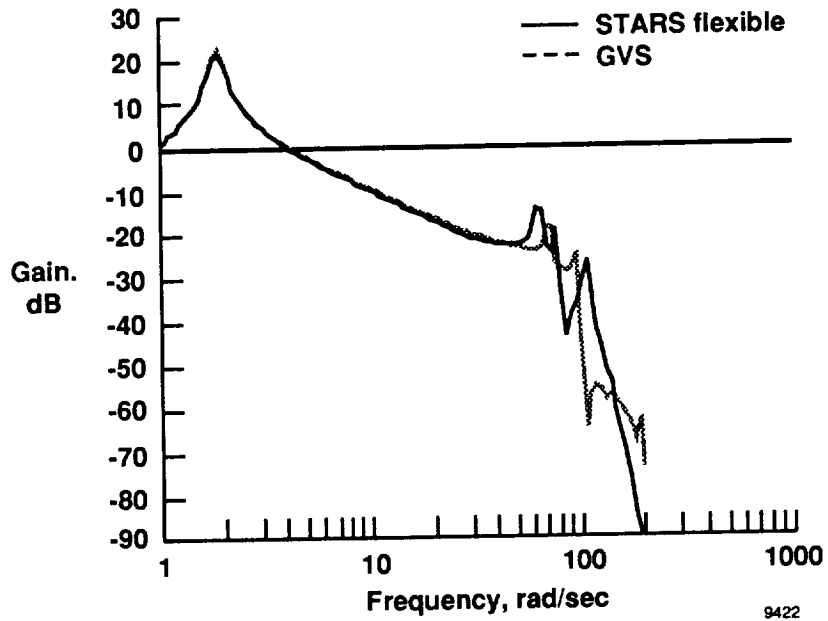


(a) Gain, dB.

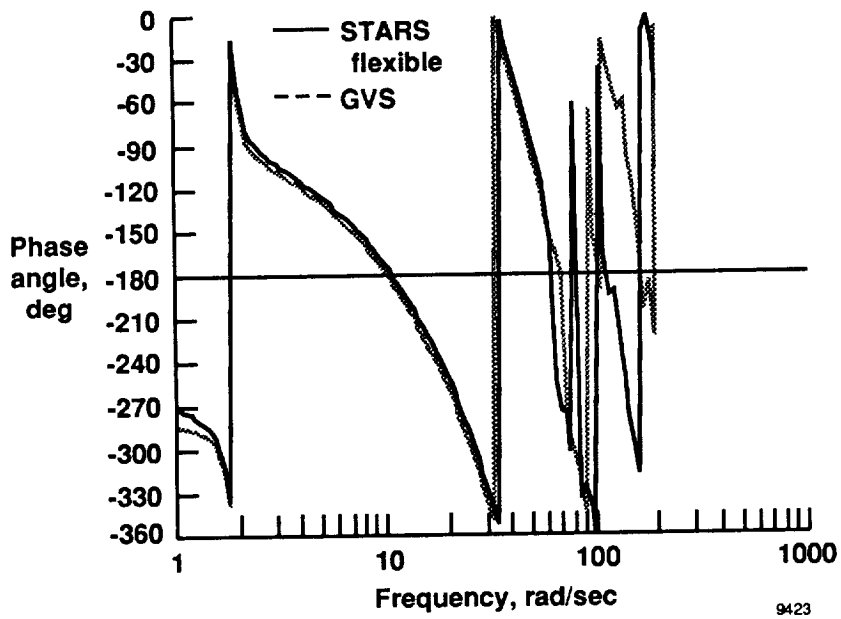


(b) Phase angle, deg.

Figure 22. Lateral loop gains computed with GVS and STARS models for flight condition 4.

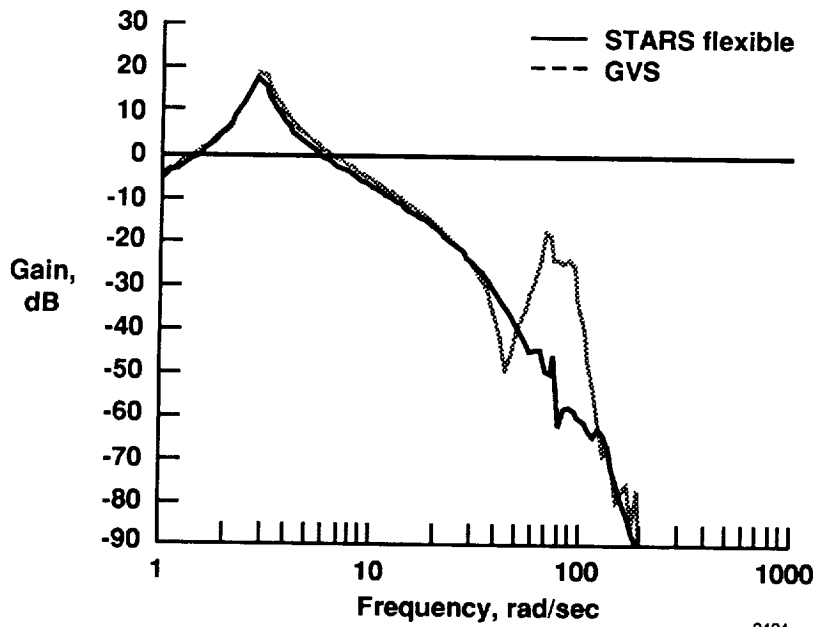


(a) Gain, dB.

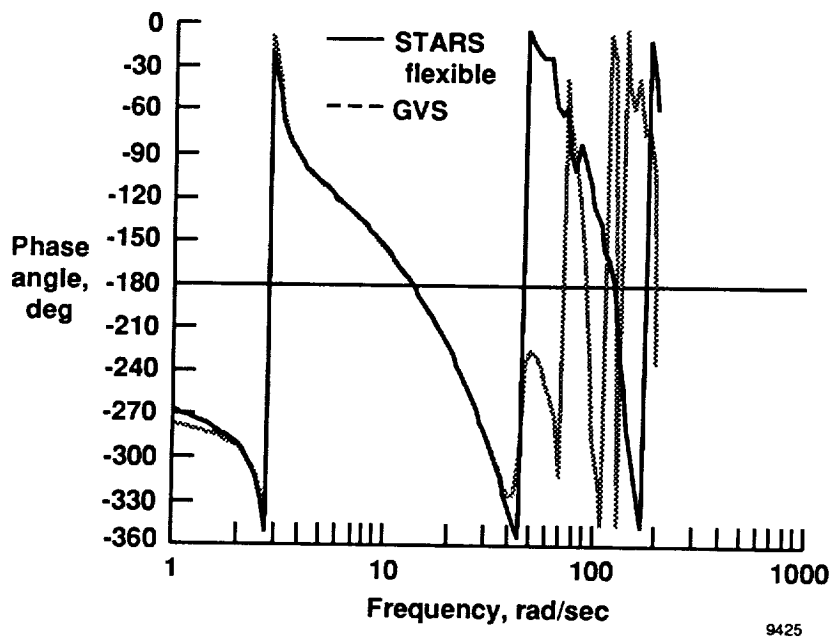


(b) Phase angle, deg.

Figure 23. Directional loop gains computed with GVS and STARS models for flight condition 1.

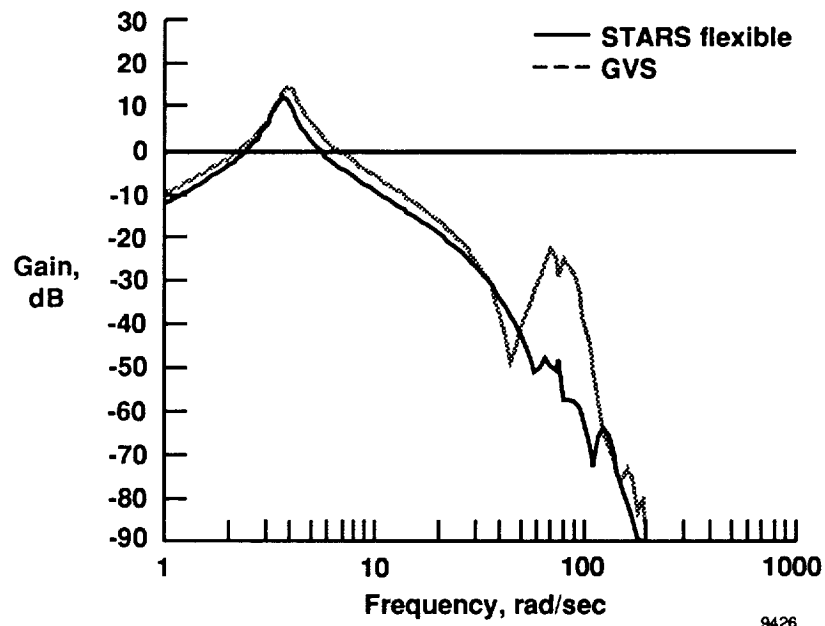


(a) Gain, dB.

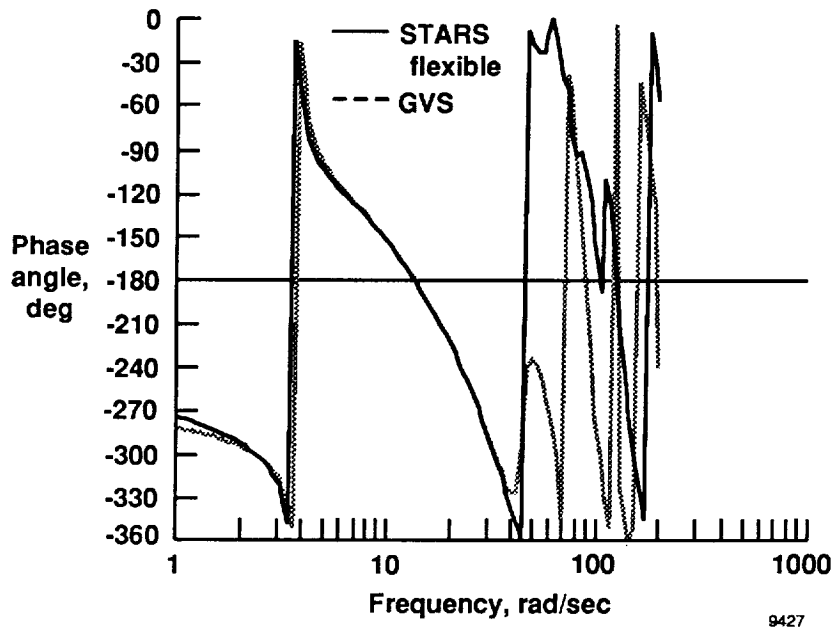


(b) Phase angle, deg.

Figure 24. Directional loop gains computed with GVS and STARS models for flight condition 2.

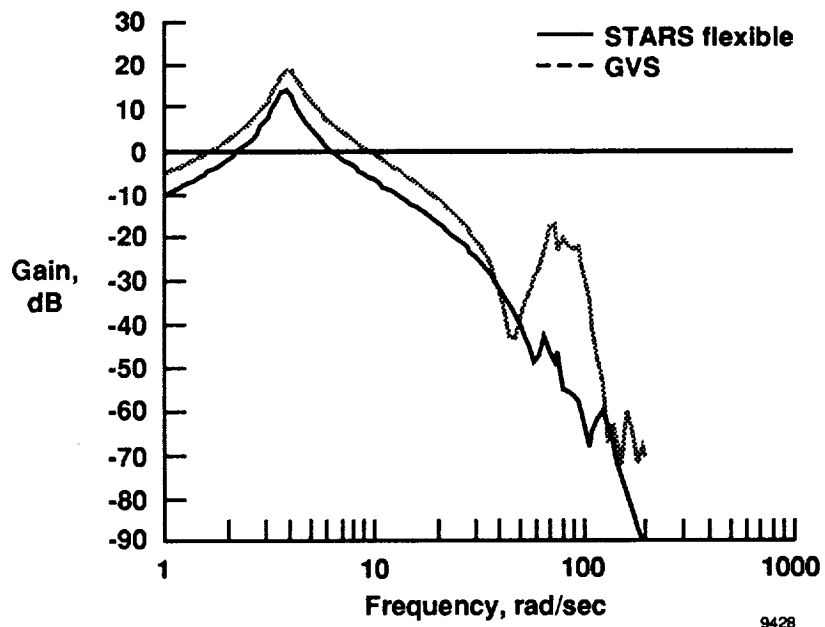


(a) Gain, dB.

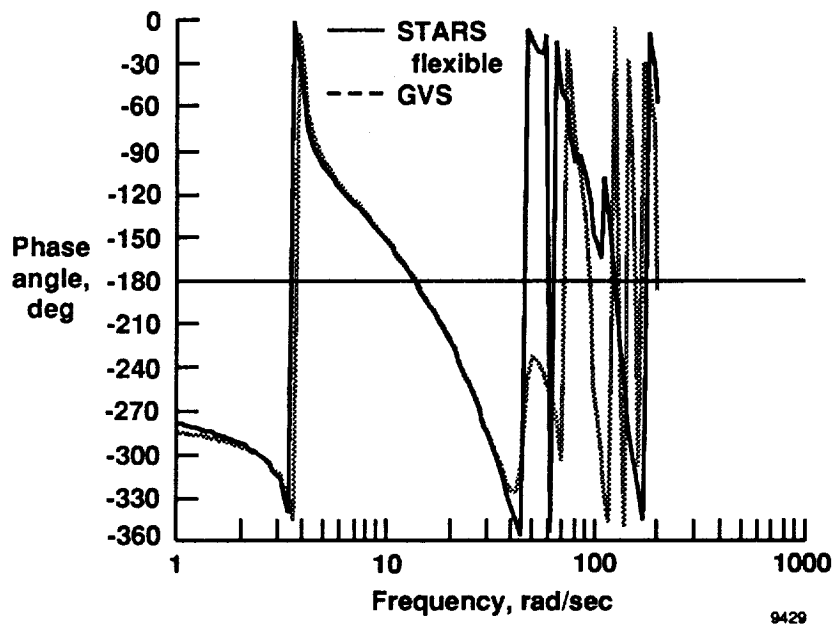


(b) Phase angle, deg.

Figure 25. Directional loop gains computed with GVS and STARS models for flight condition 3.

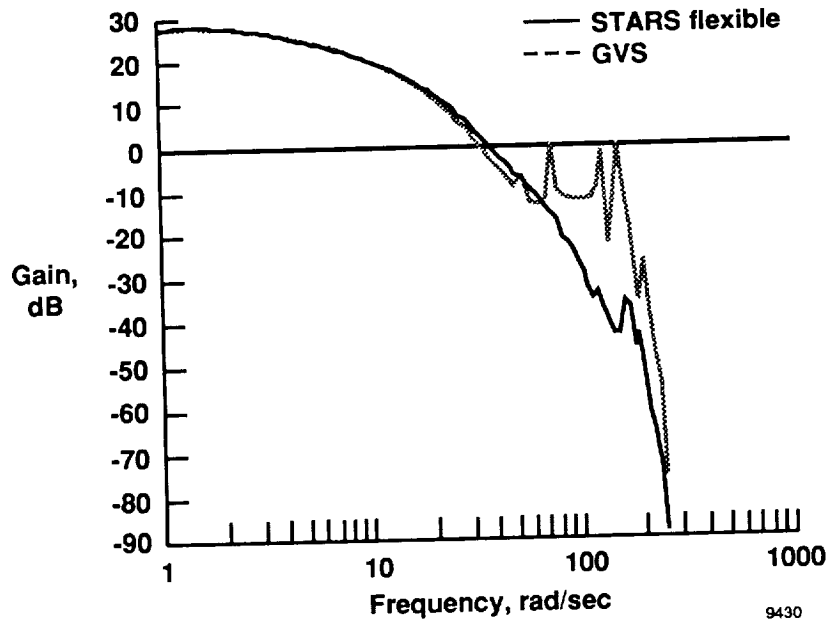


(a) Gain, dB.

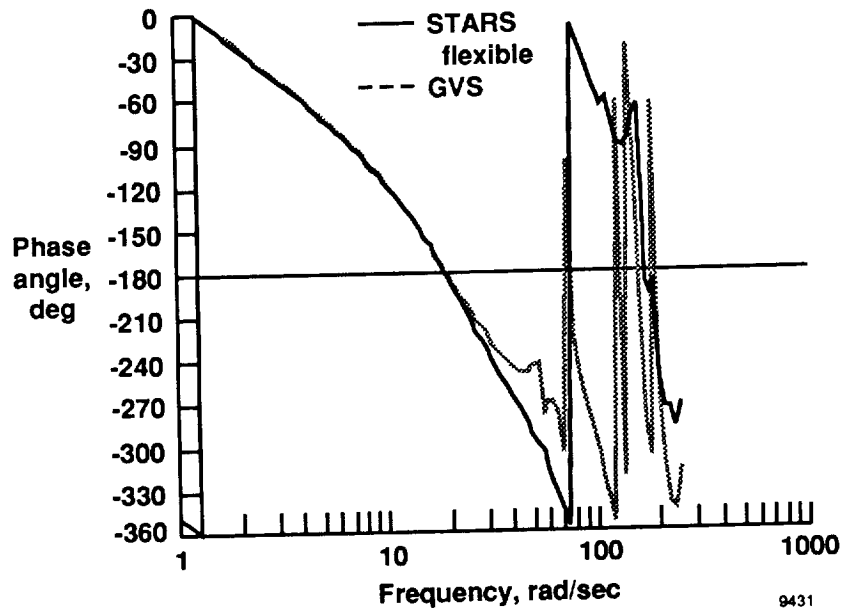


(b) Phase angle, deg.

Figure 26. Directional loop gains computed with GVS and STARS models for flight condition 4.

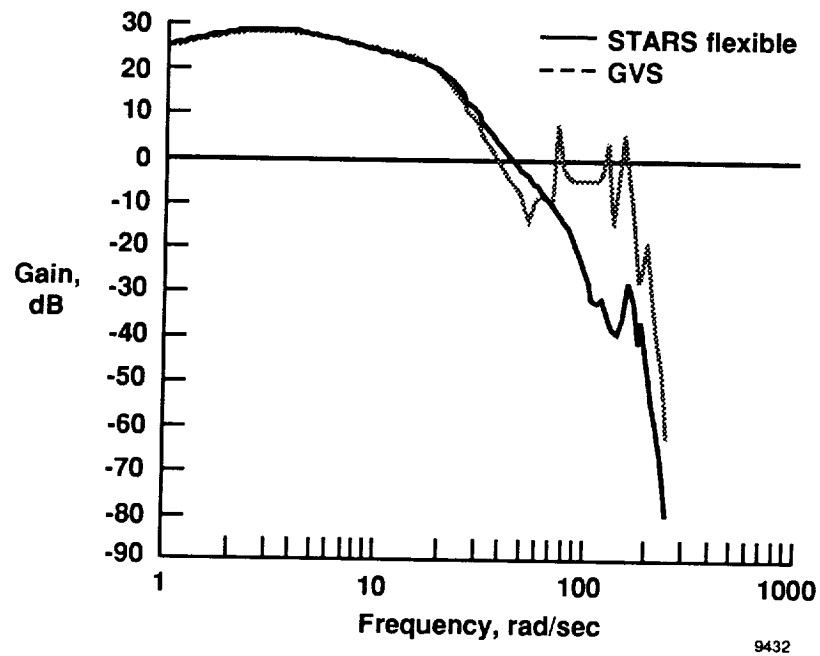


(a) Gain, dB.

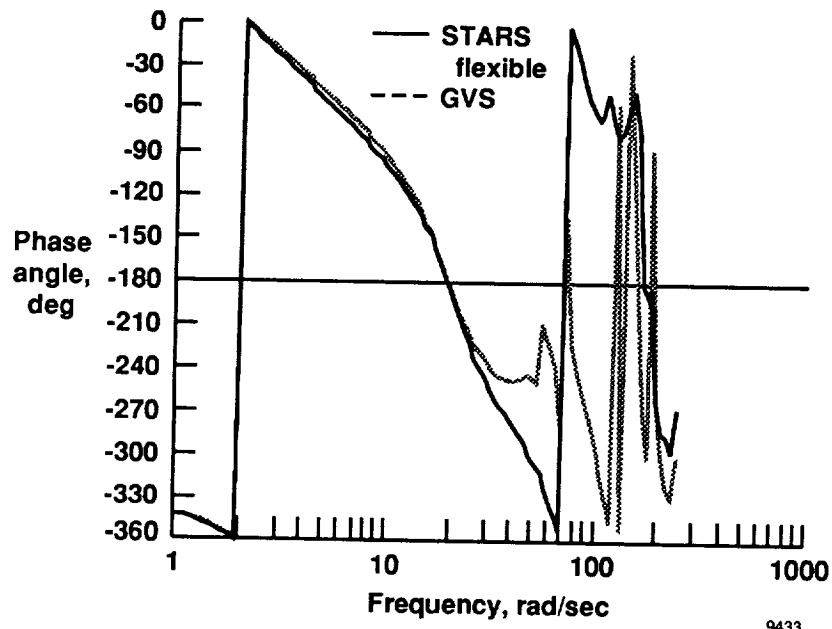


(b) Phase angle, deg.

Figure 27. Longitudinal closed-loop responses calculated using GVS and STARS flexible models for flight condition 1.

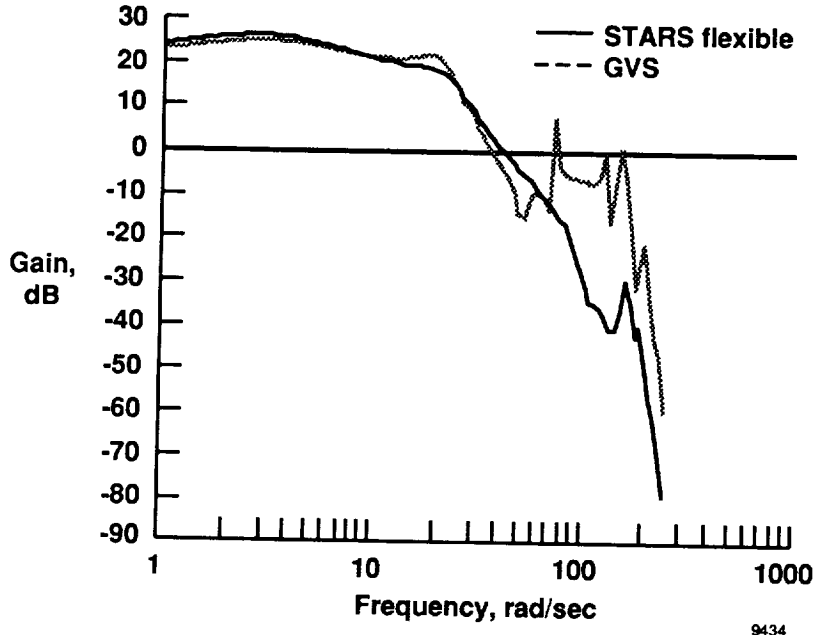


(a) Gain, dB.

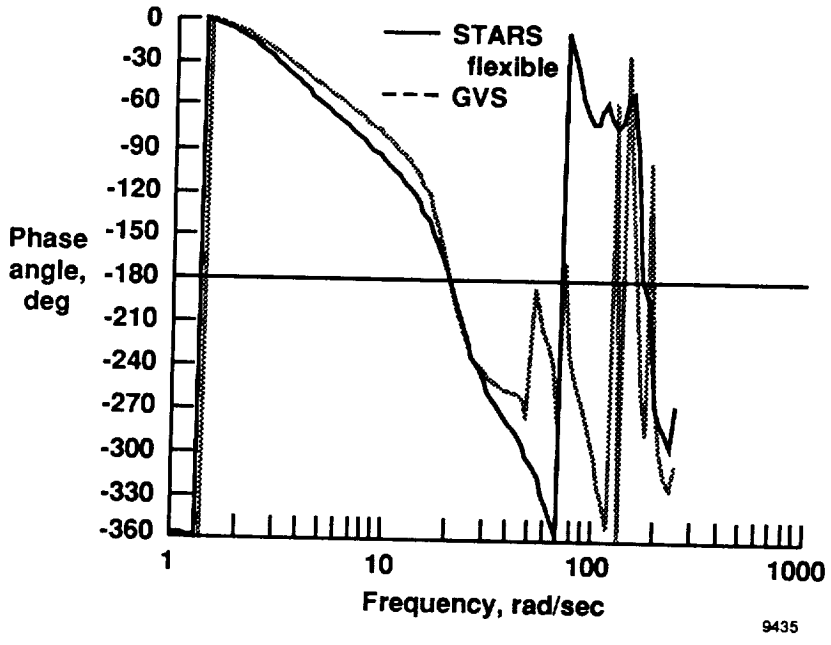


(b) Phase angle, deg.

Figure 28. Longitudinal closed-loop responses calculated using GVS and STARS flexible models for flight condition 2.

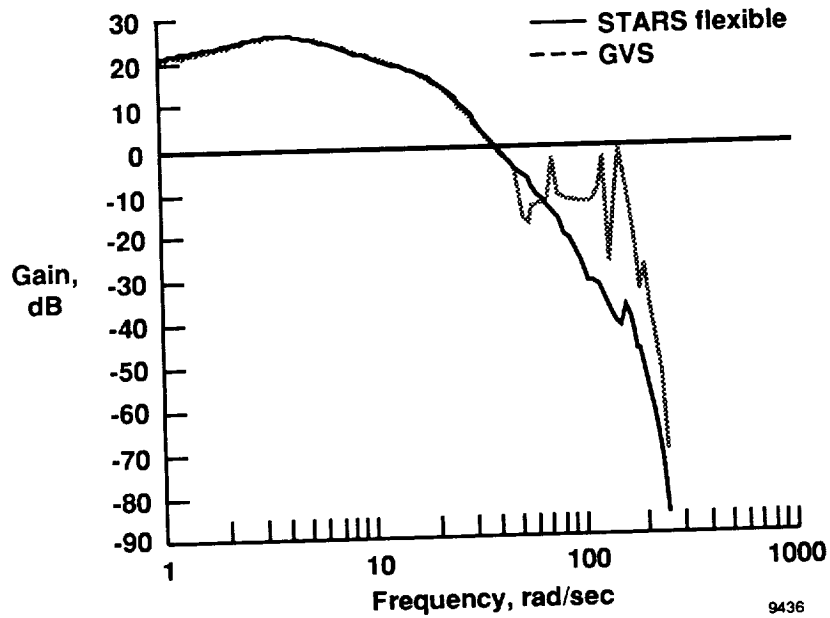


(a) Gain, dB.

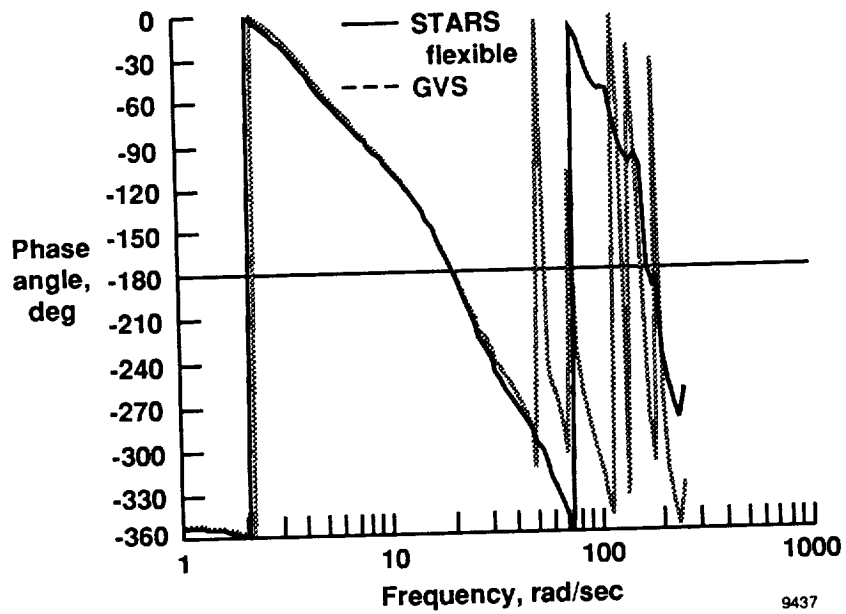


(b) Phase angle, deg.

Figure 29. Longitudinal closed-loop responses calculated using GVS and STARS flexible models for flight condition 3.

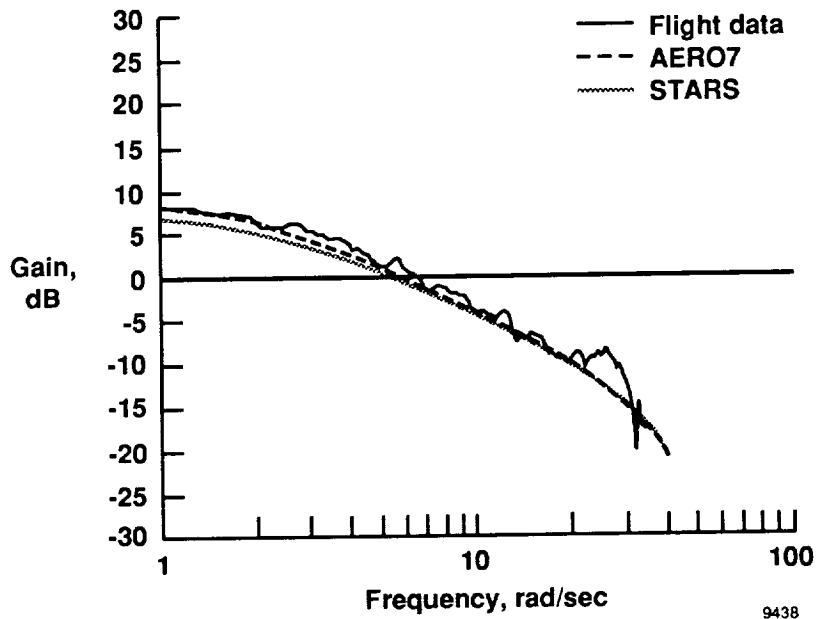


(a) Gain, dB.

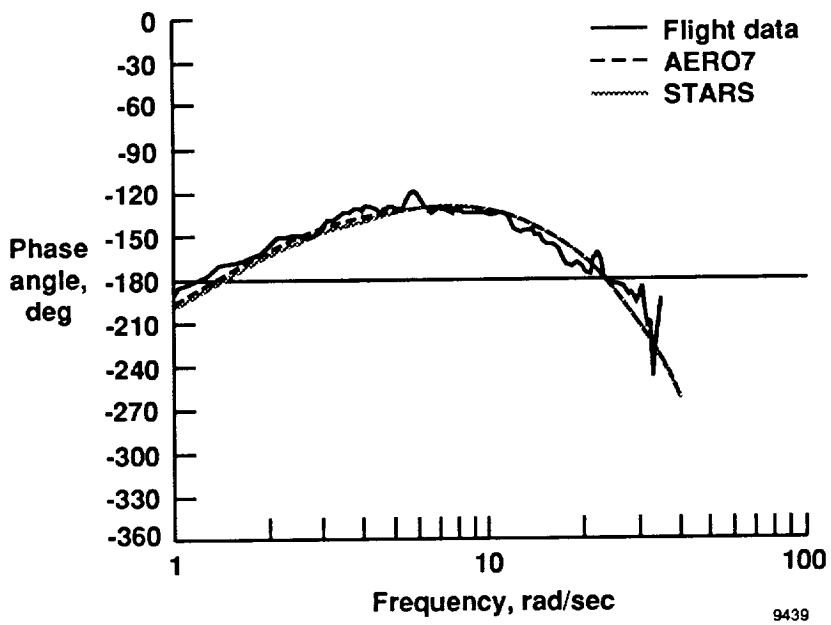


(b) Phase angle, deg.

Figure 30. Longitudinal closed-loop responses calculated using GVS and STARS flexible models for flight condition 4.

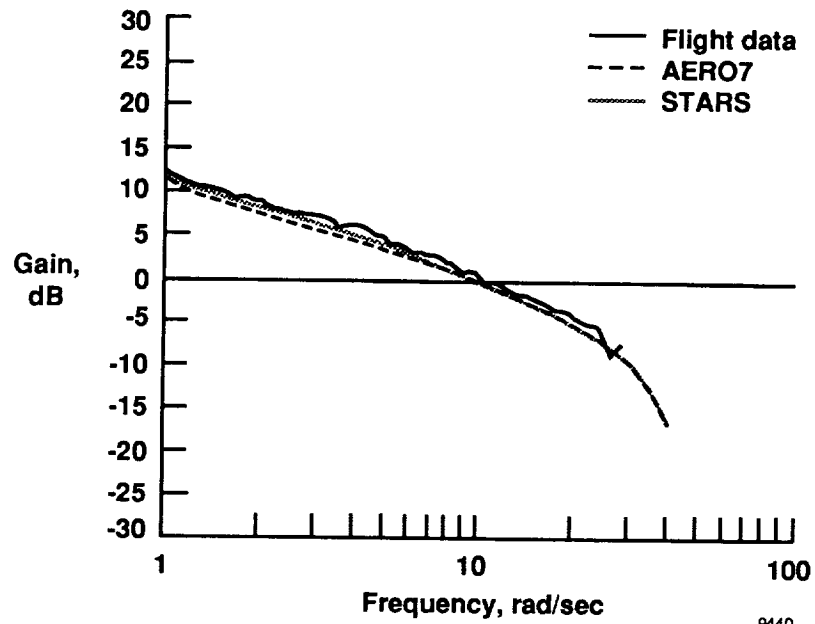


(a) Gain, dB.

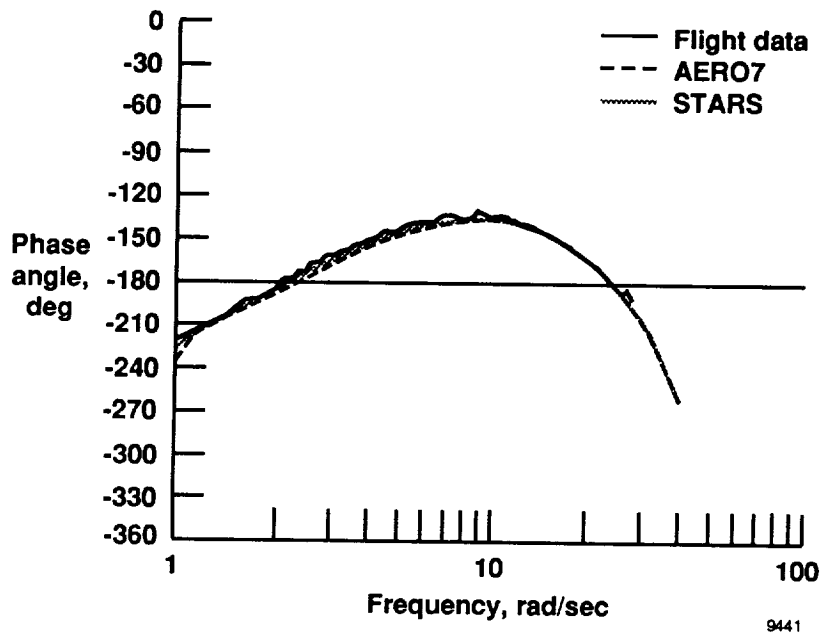


(b) Phase angle, deg.

Figure 31. Longitudinal loop gains from flight data, AERO7, and STARS for flight condition 1.

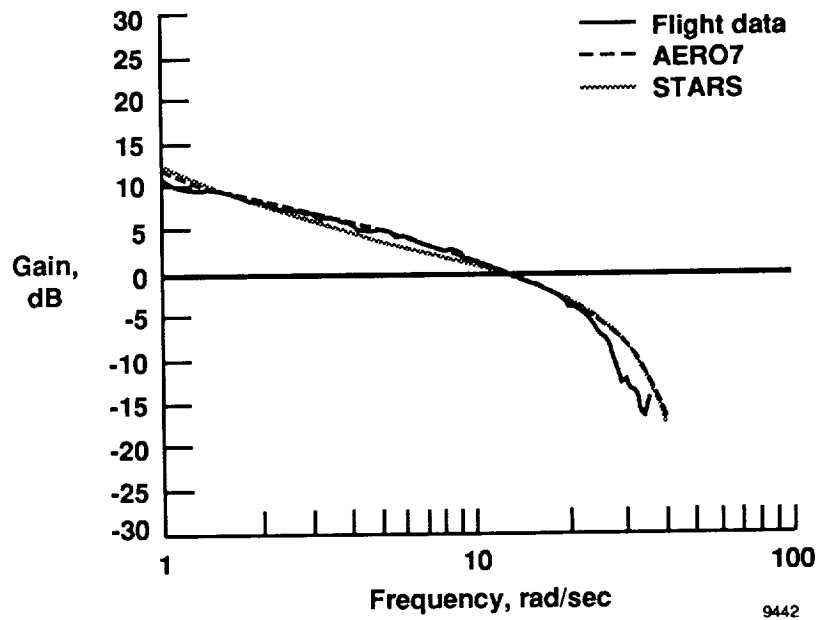


(a) Gain, dB.

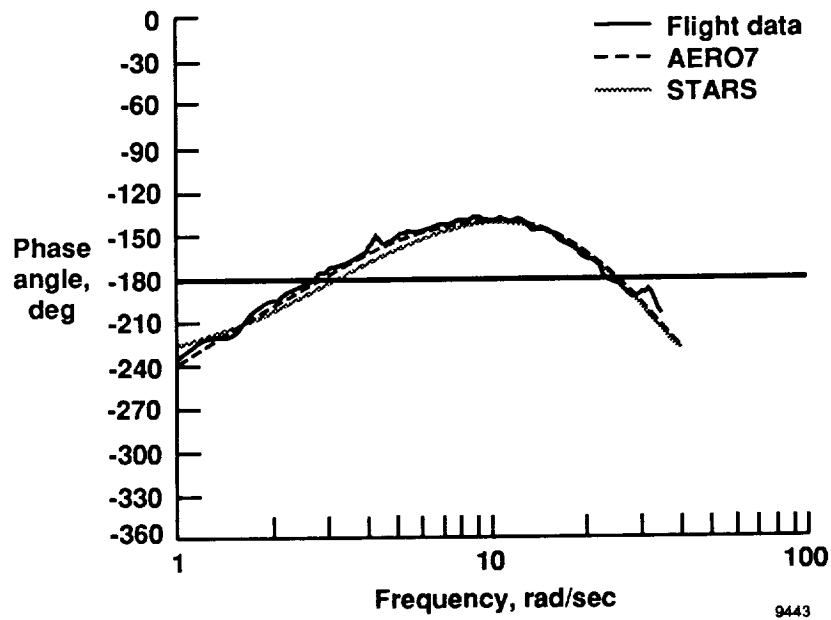


(b) Phase angle, deg.

Figure 32. Longitudinal loop gains from flight data, AERO7, and STARS for flight condition 2.

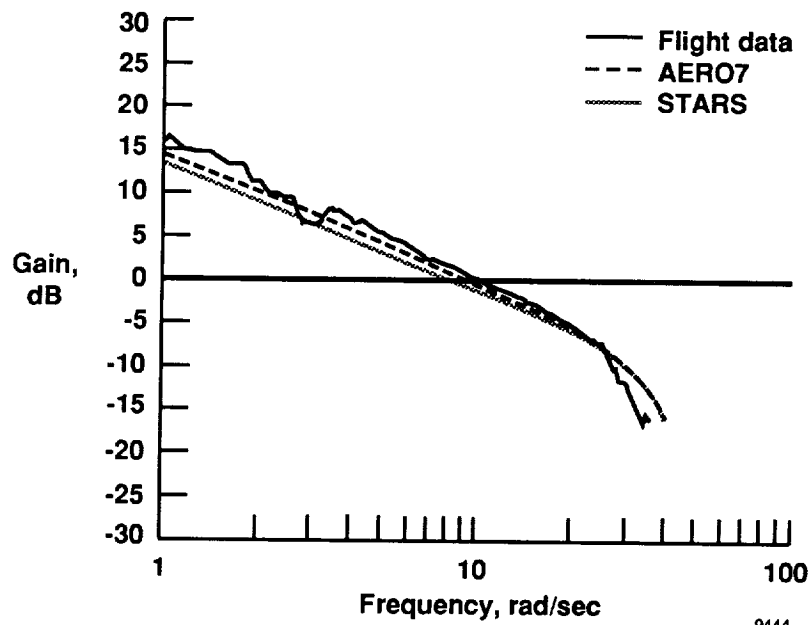


(a) Gain, dB.

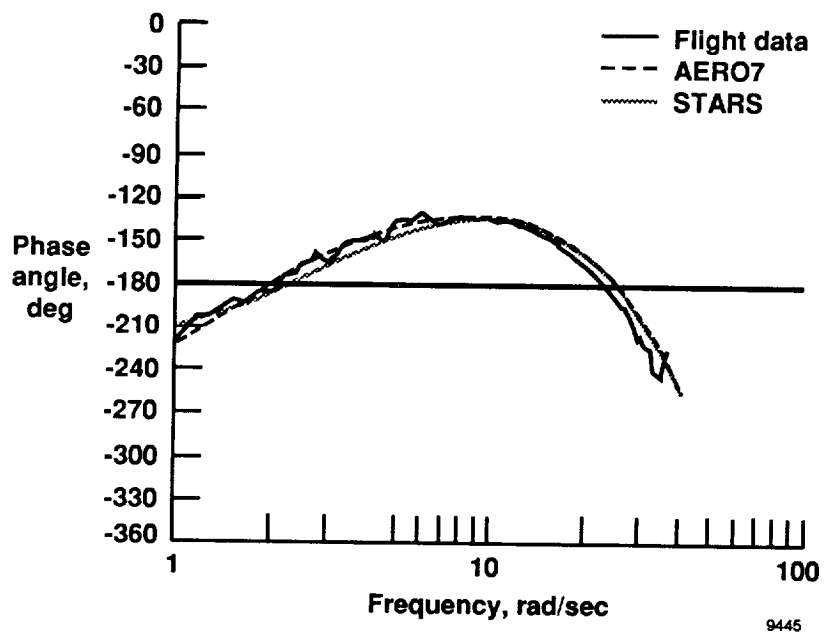


(b) Phase angle, deg.

Figure 33. Longitudinal loop gains from flight data, AERO7, and STARS for flight condition 3.

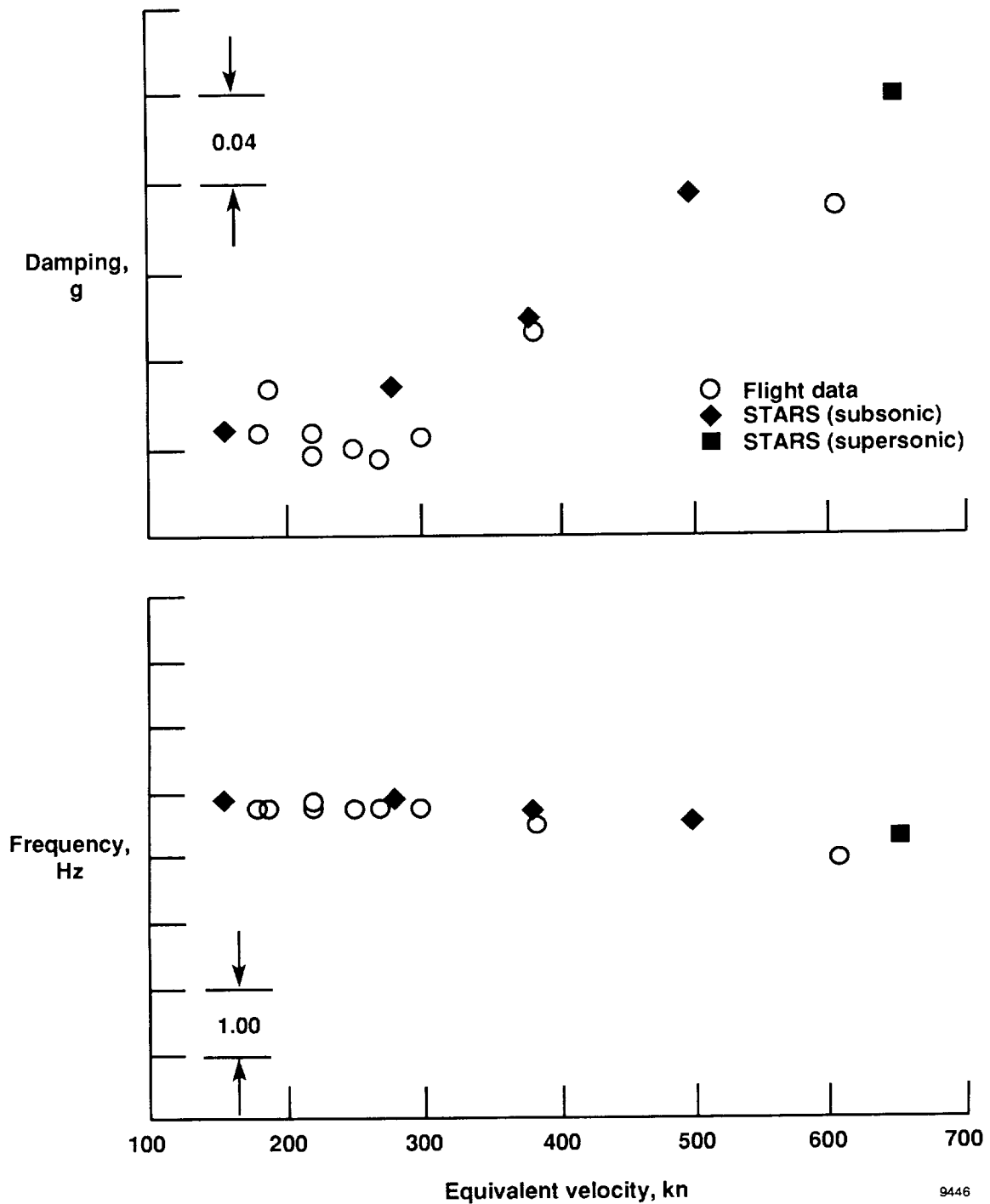


(a) Gain, dB.



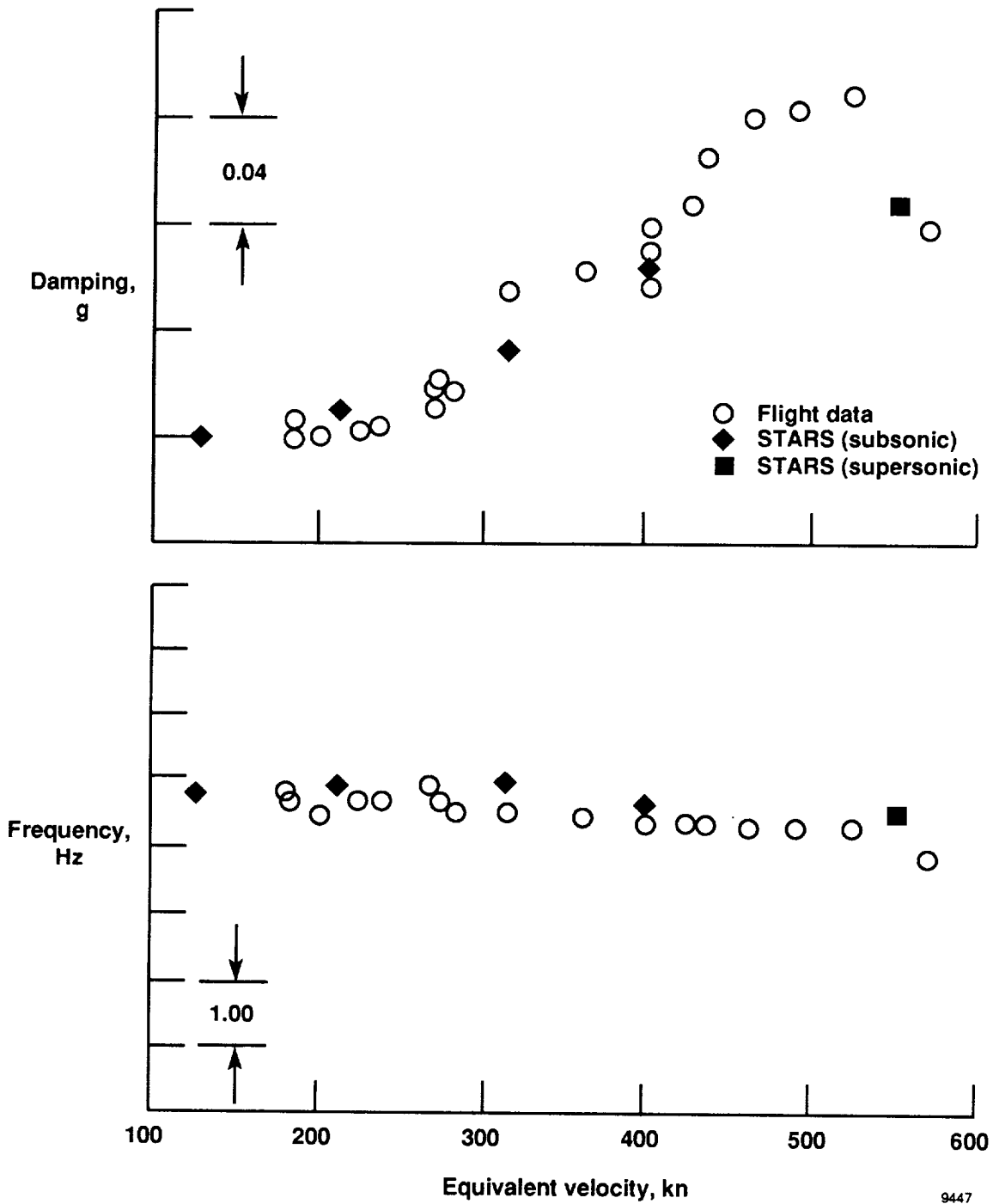
(b) Phase angle, deg.

Figure 34. Longitudinal loop gains from flight data, AERO7, and STARS for flight condition 4.



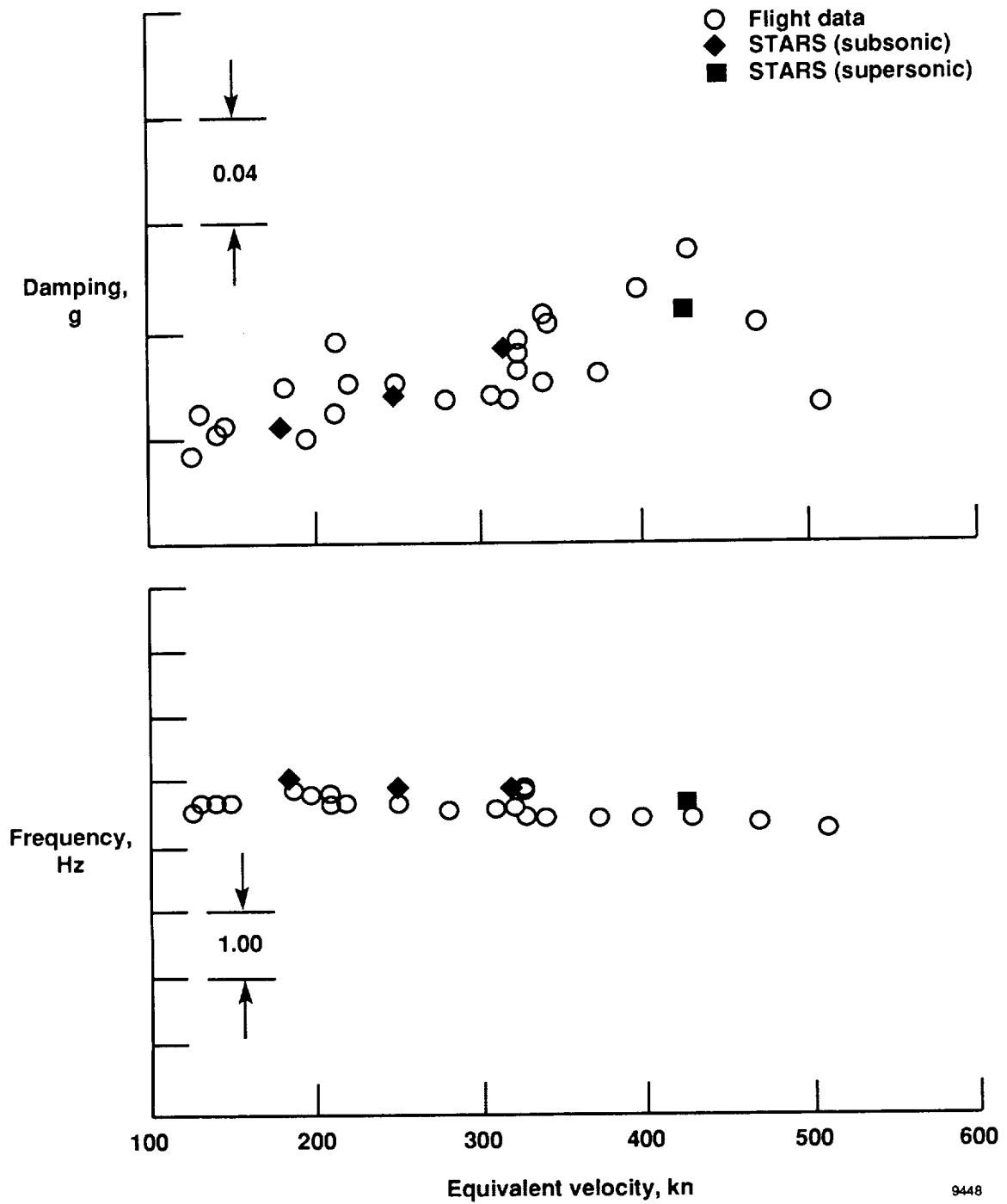
(a) 10,000 ft.

Figure 35. Modal damping and frequency comparisons between flight measured data and STARS for symmetric wing first bending.



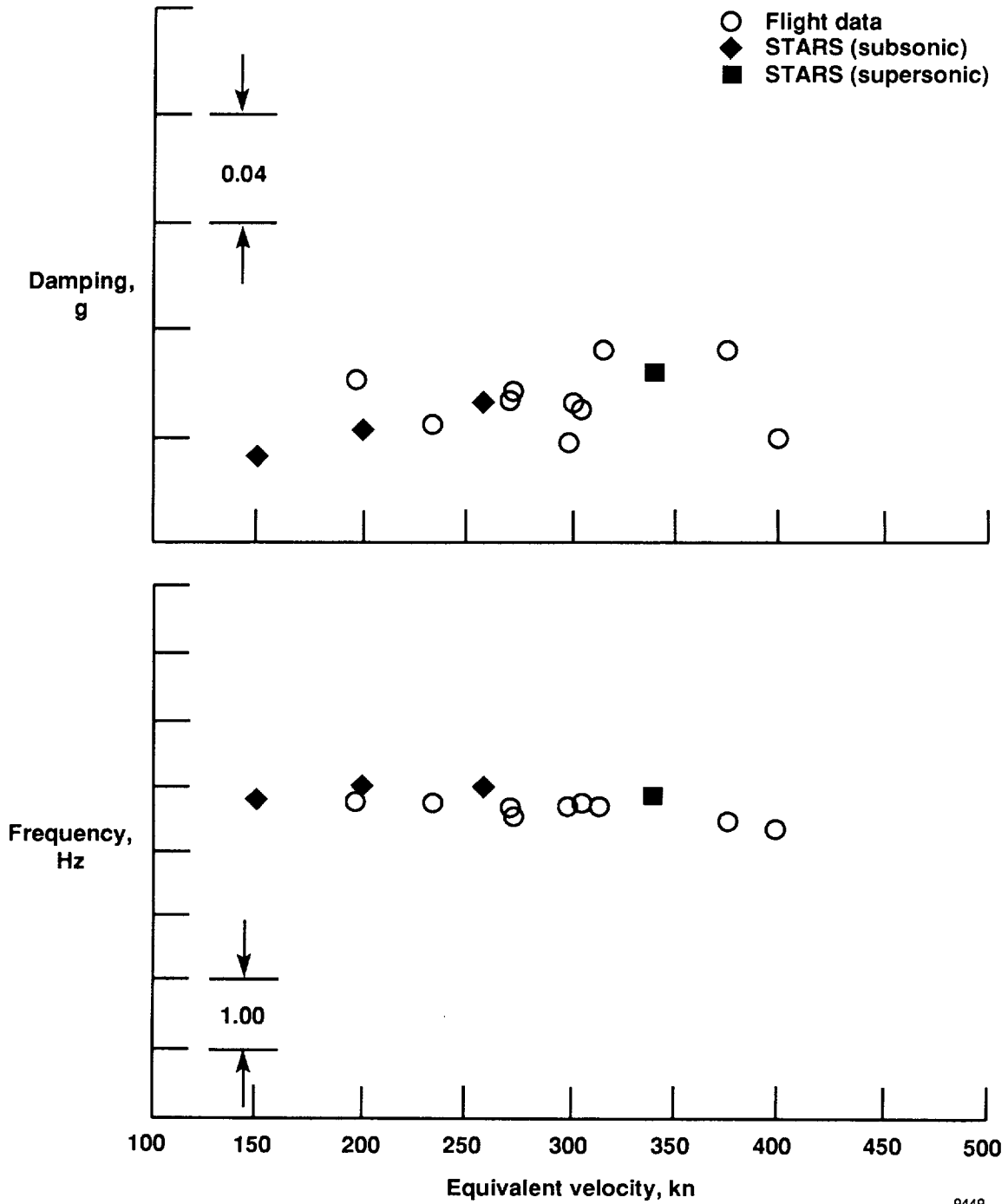
(b) 20,000 ft.

Figure 35. Continued.



(c) 30,000 ft.

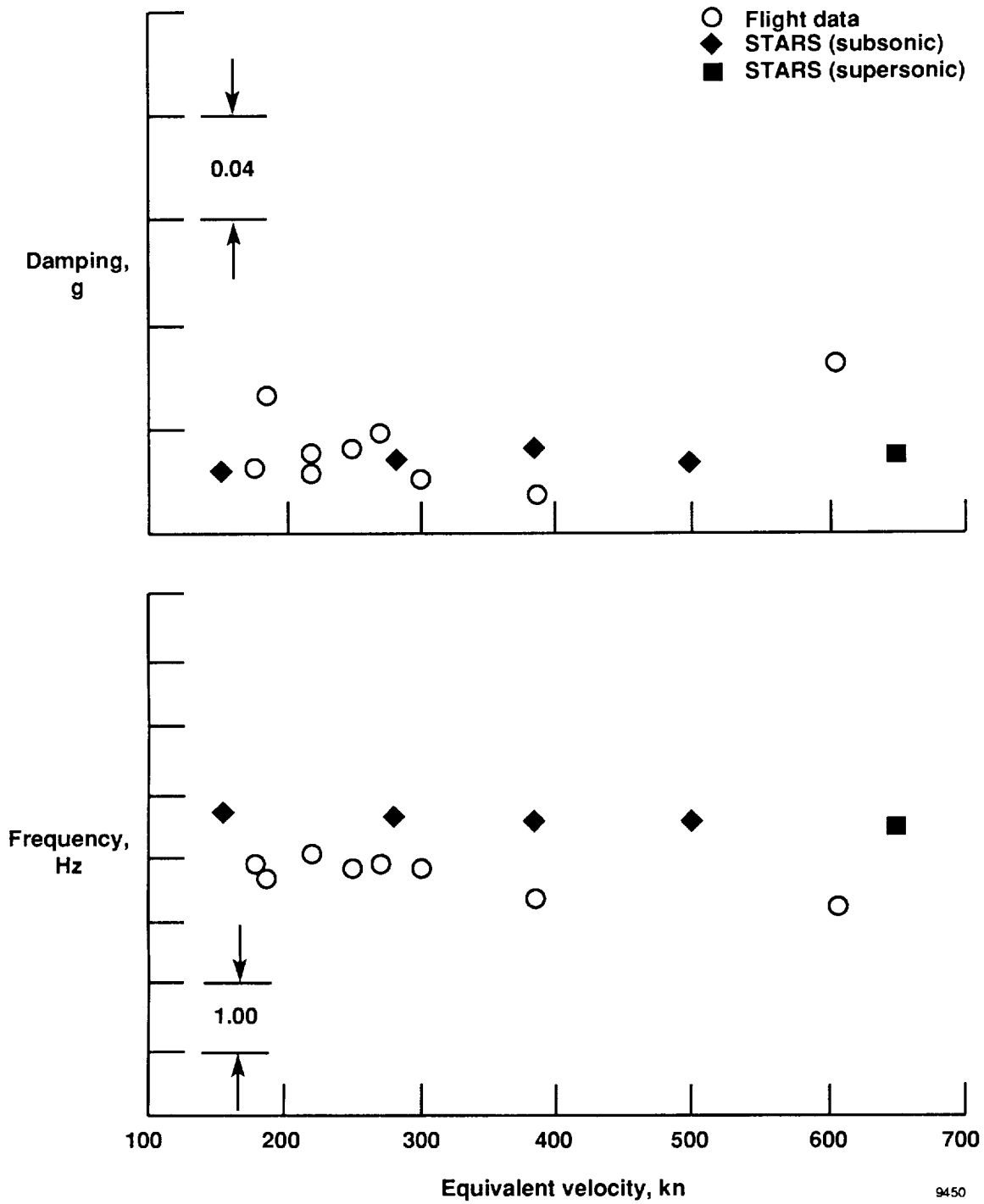
Figure 35. Continued.



(d) 40,000 ft.

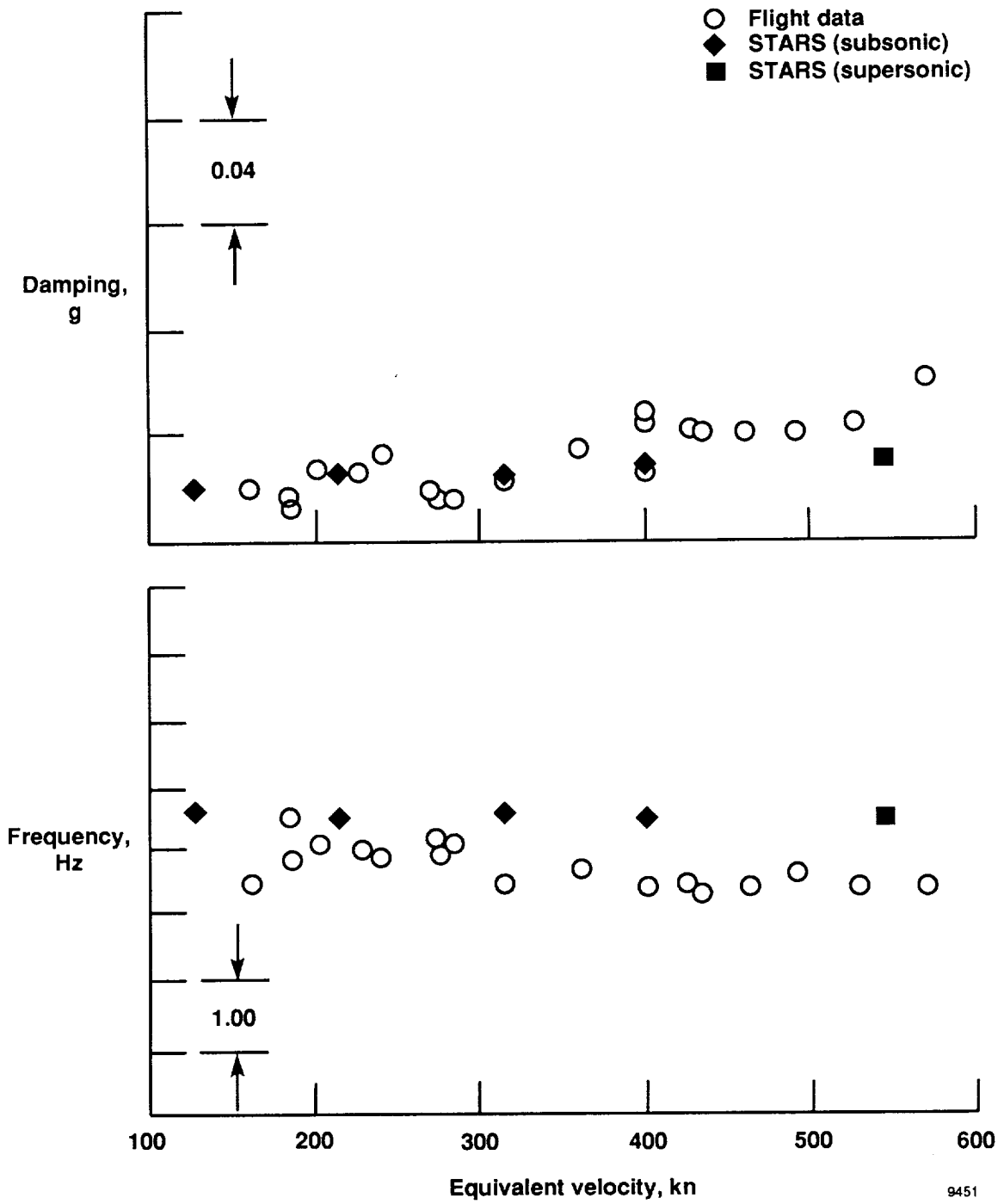
Figure 35. Concluded.

9449



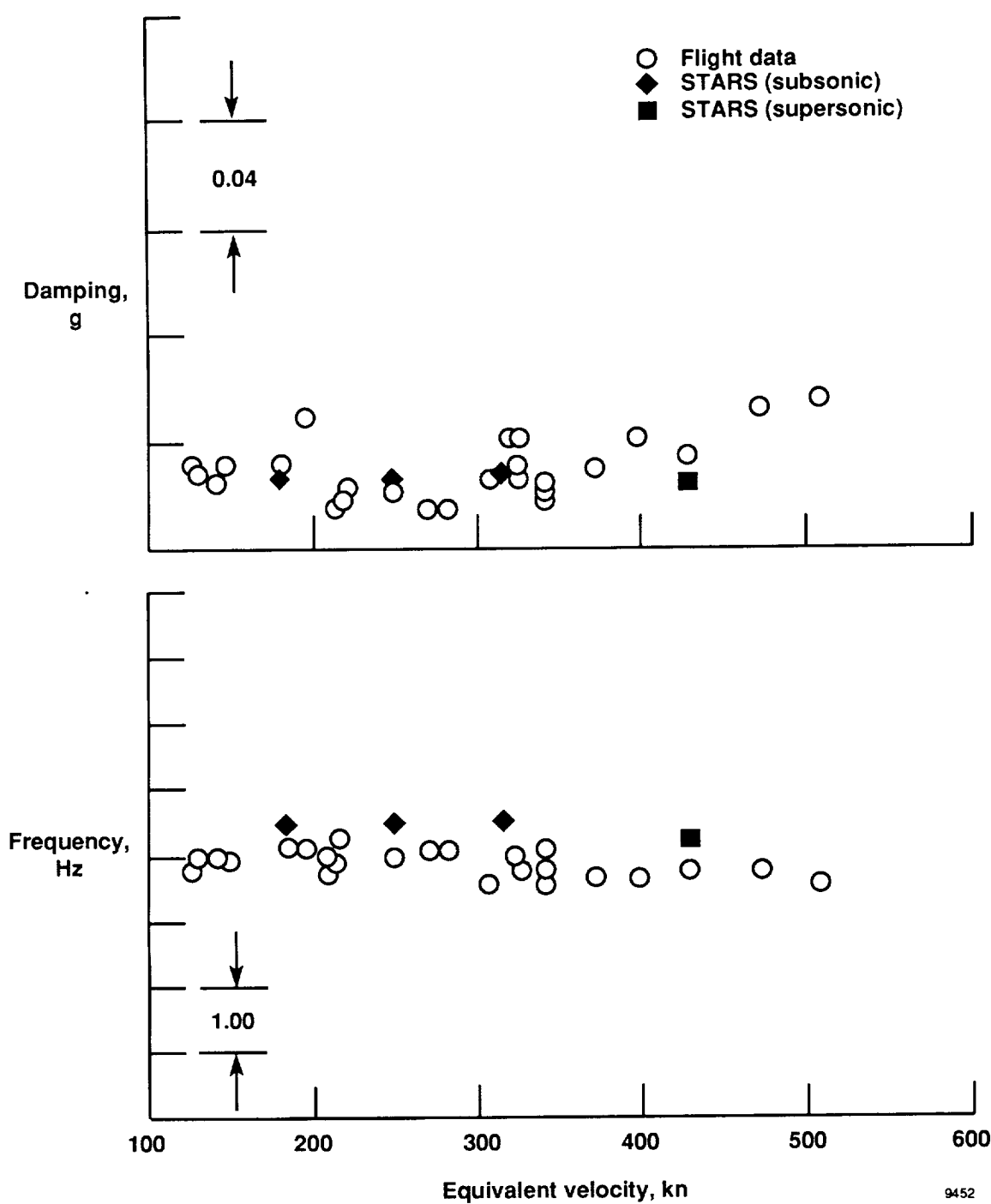
(a) 10,000 ft.

Figure 36. Modal damping and frequency comparisons between flight measured data and STARS for fuselage vertical bending.



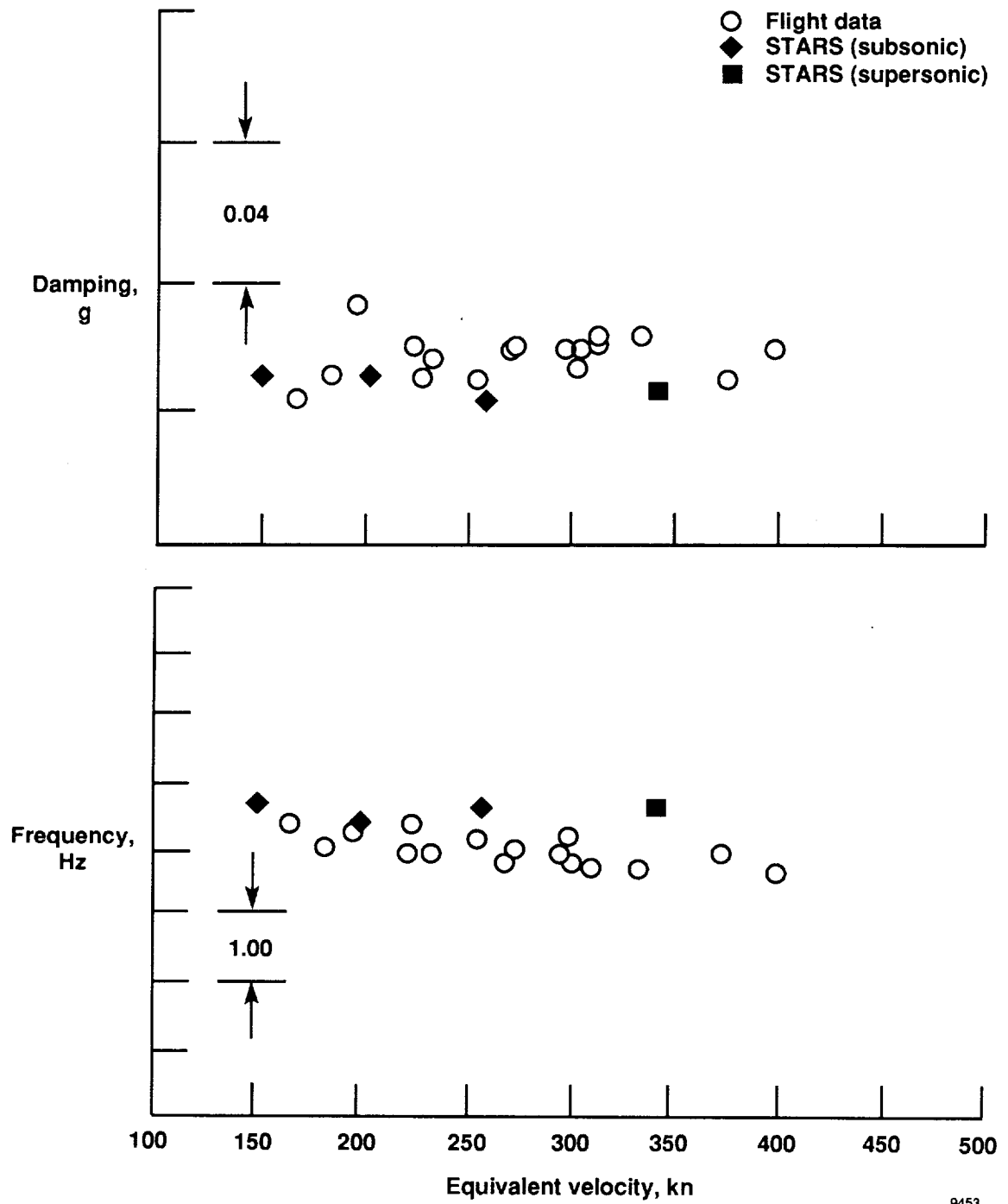
(b) 20,000 ft.

Figure 36. Continued.



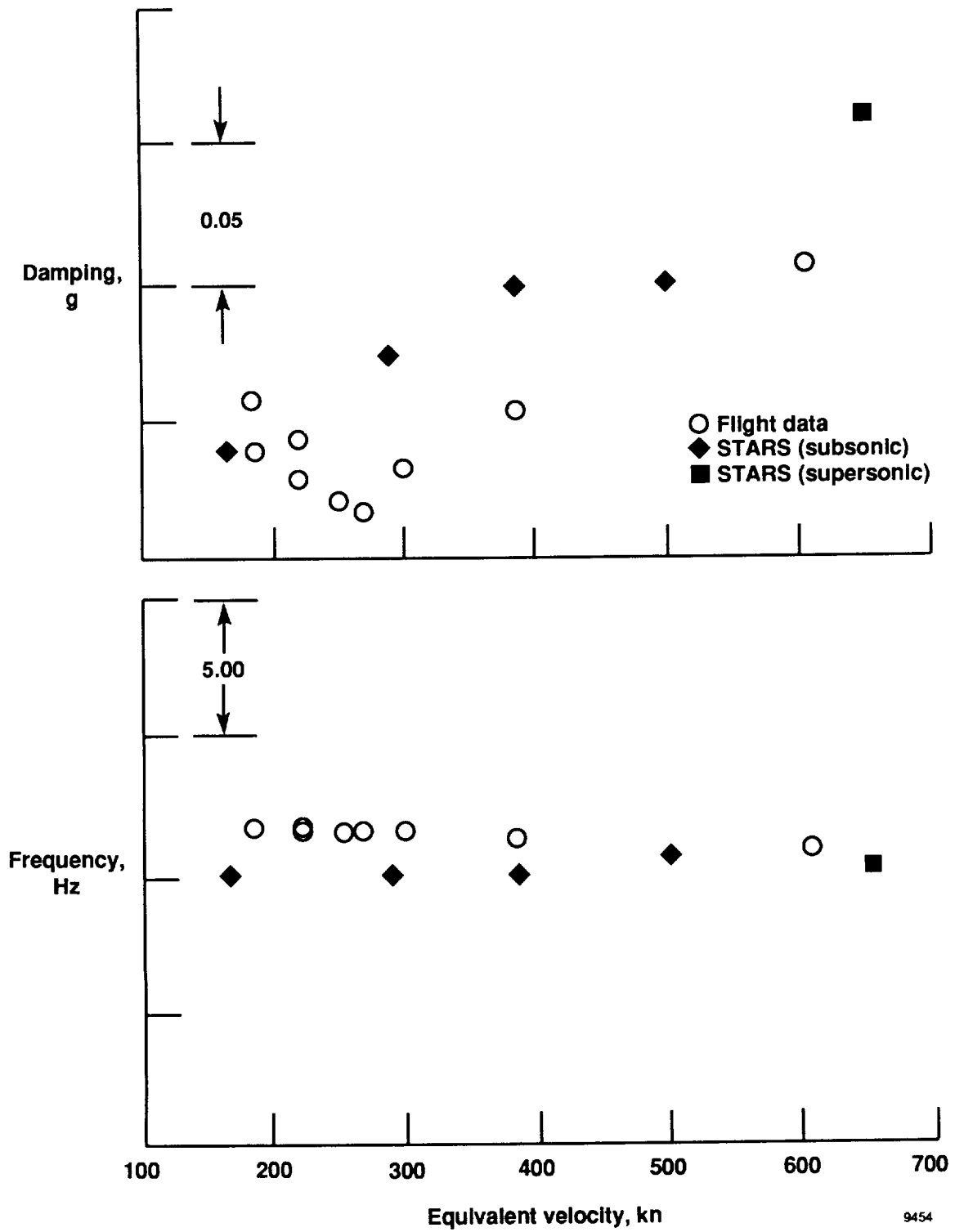
(c) 30,000 ft.

Figure 36. Continued.



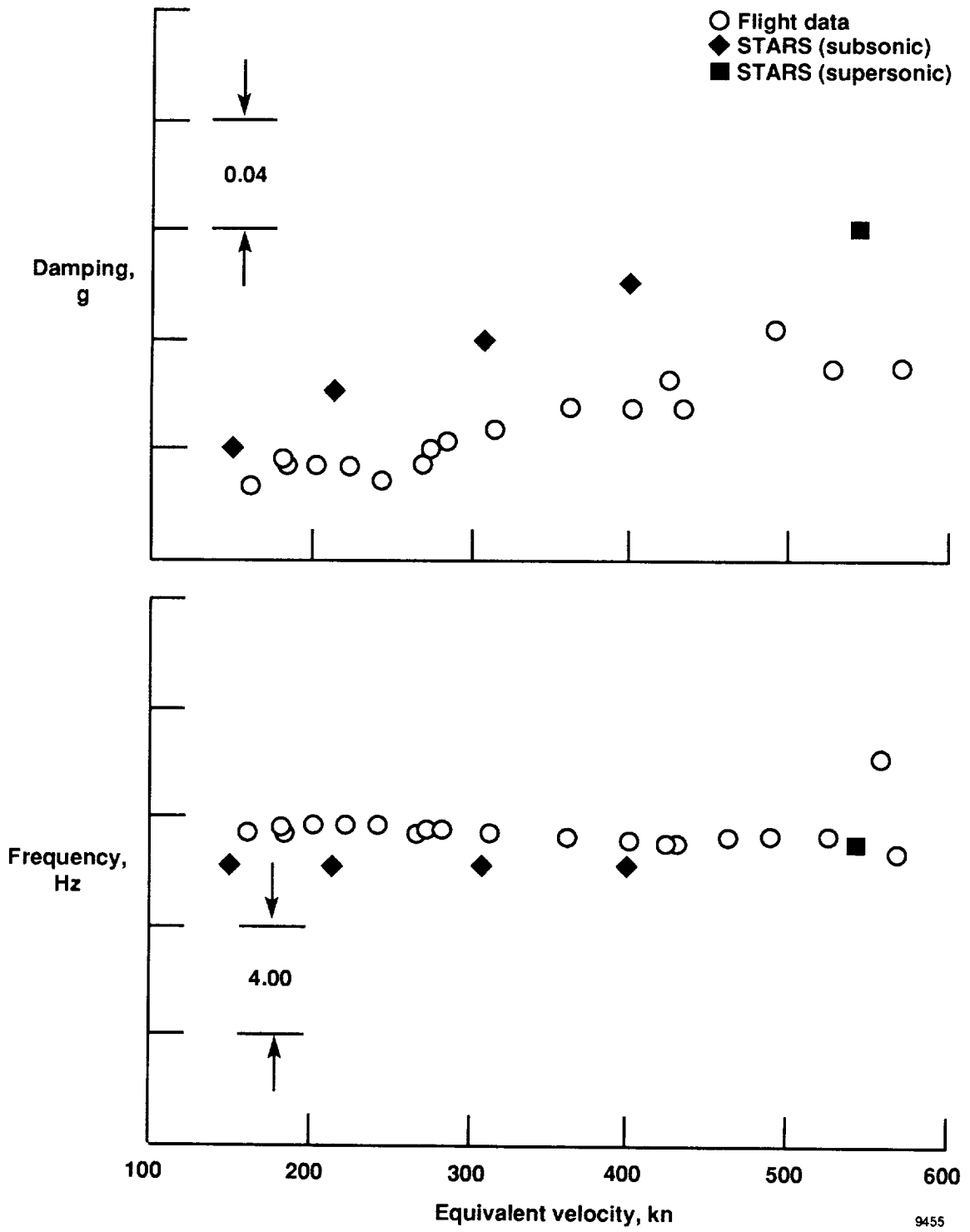
(d) 40,000 ft.

Figure 36. Concluded.



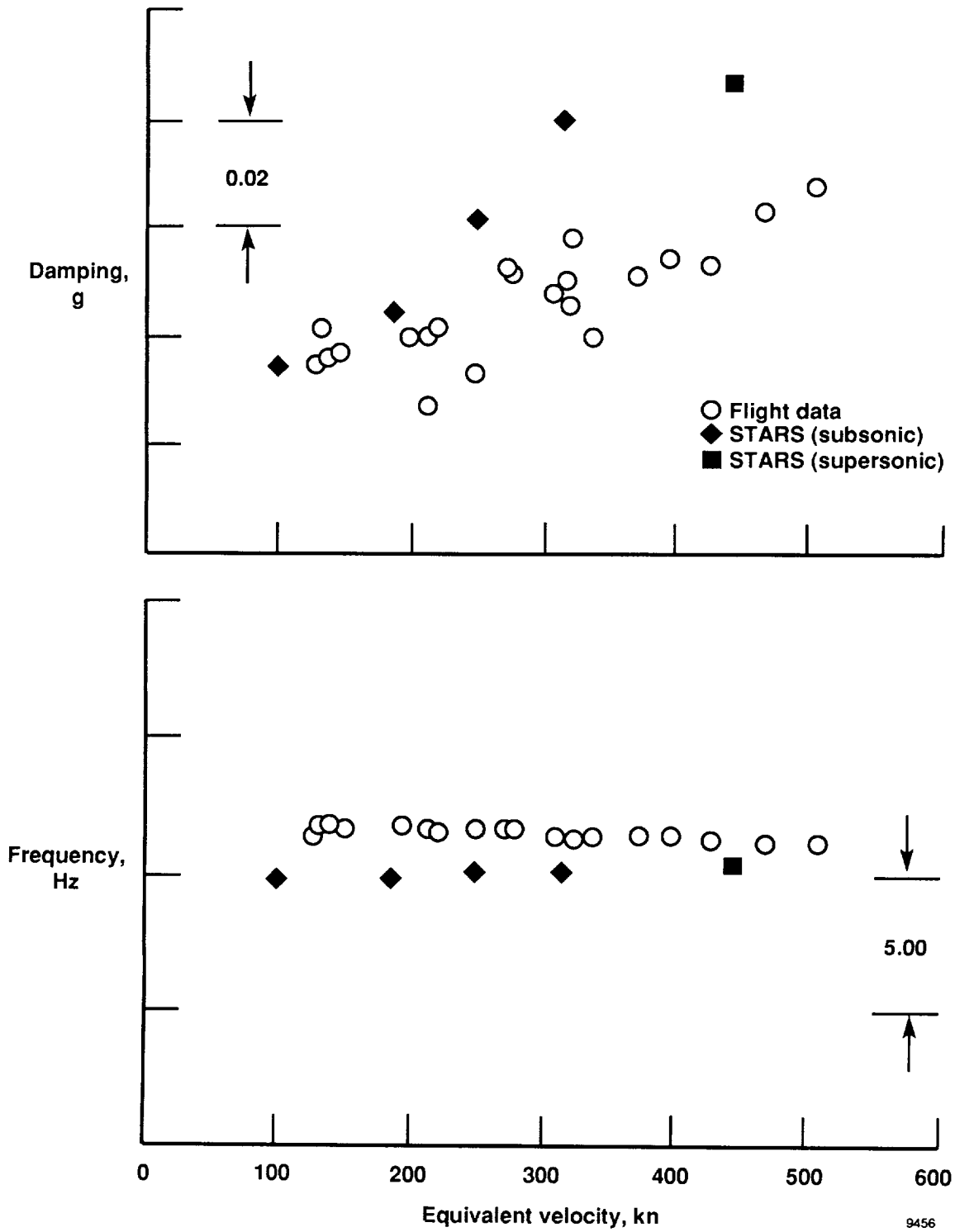
(a) 10,000 ft.

Figure 37. Modal damping and frequency comparisons between flight measured data and STARS for antisymmetric wing first bending.



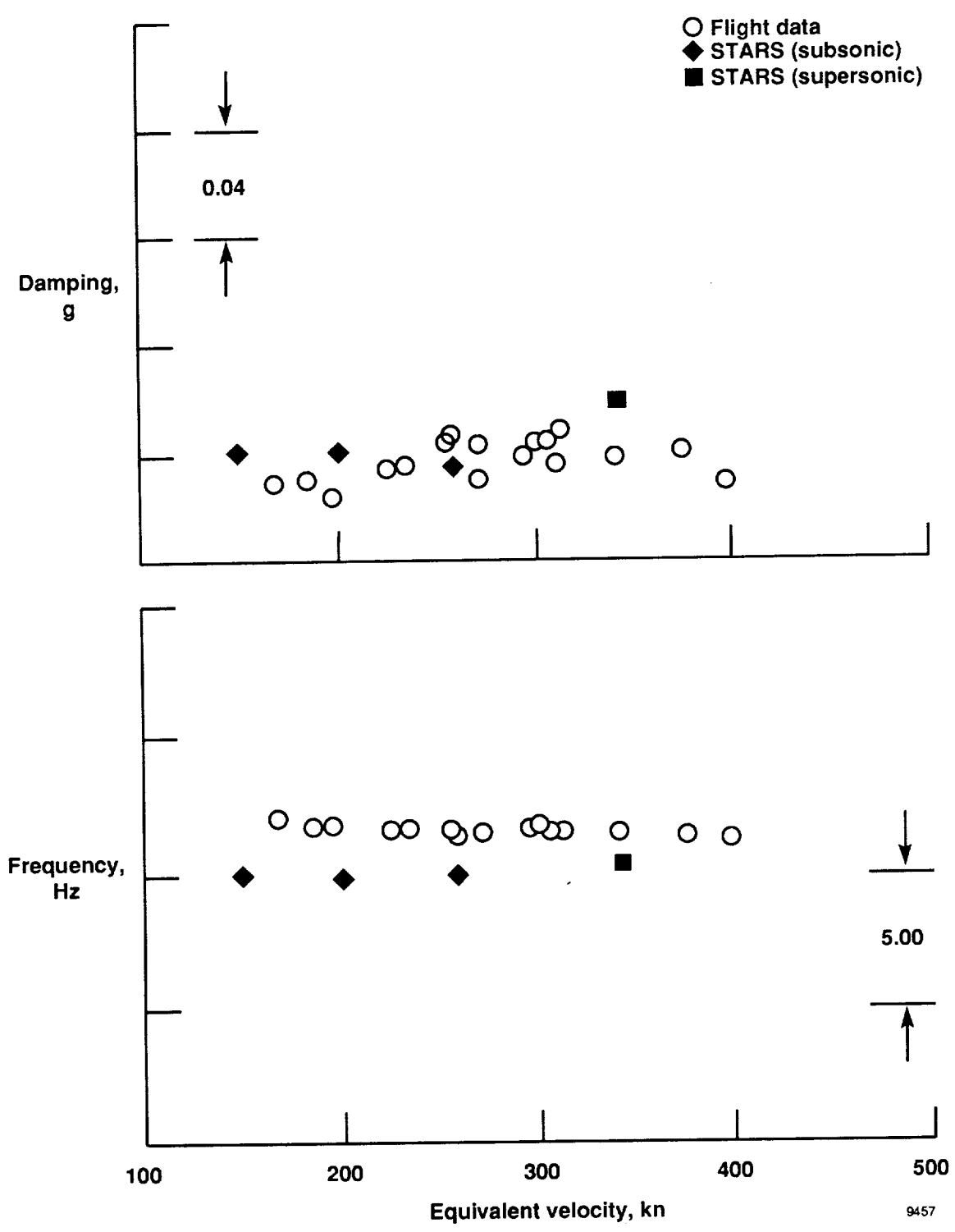
(b) 20,000 ft.

Figure 37. Continued.



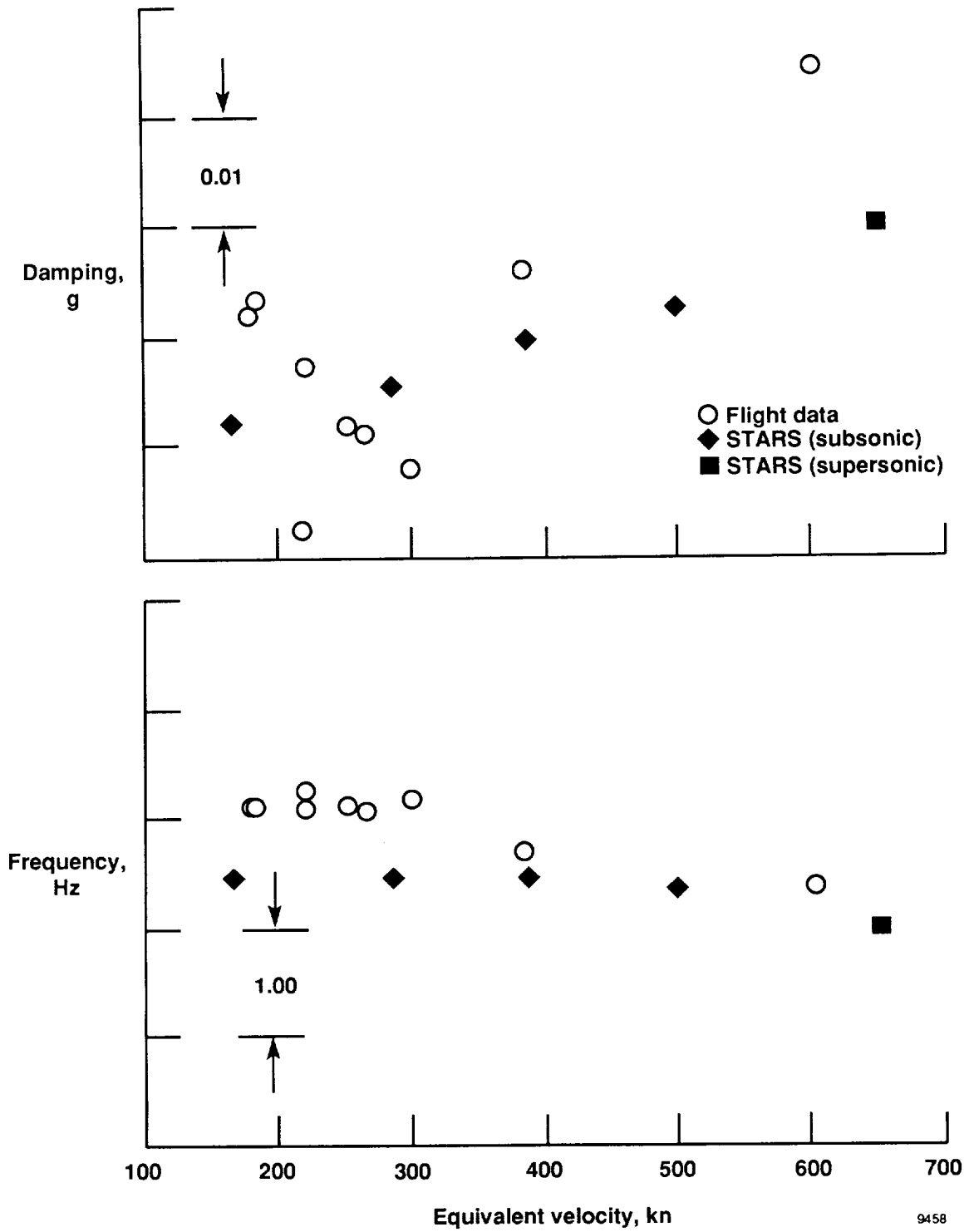
(c) 30,000 ft.

Figure 37. Continued.



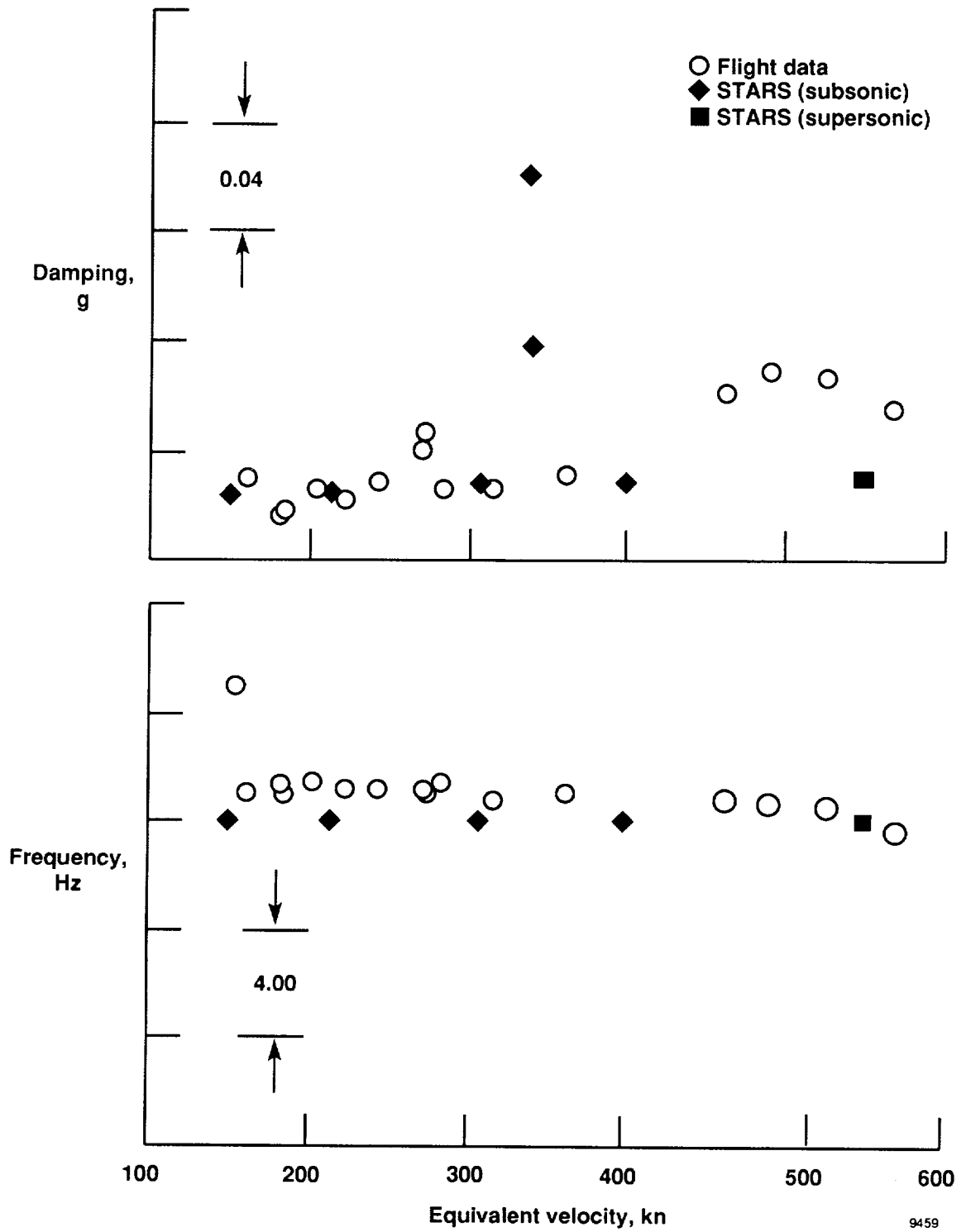
(d) 40,000 ft.

Figure 37. Concluded.



(a) 10,000 ft.

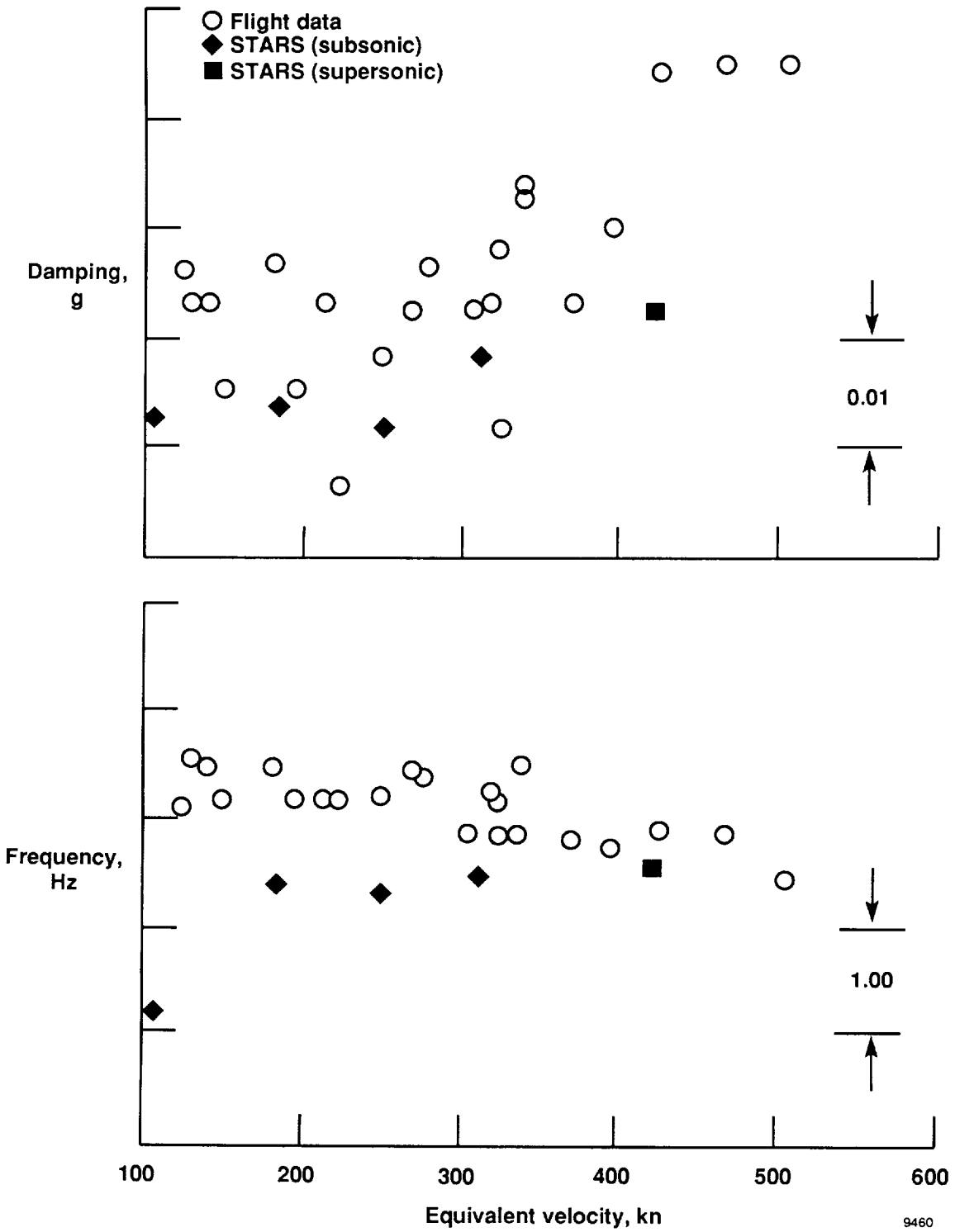
Figure 38. Modal damping and frequency comparisons between flight measured data and STARS for fuselage lateral bending.



(b) 20,000 ft.

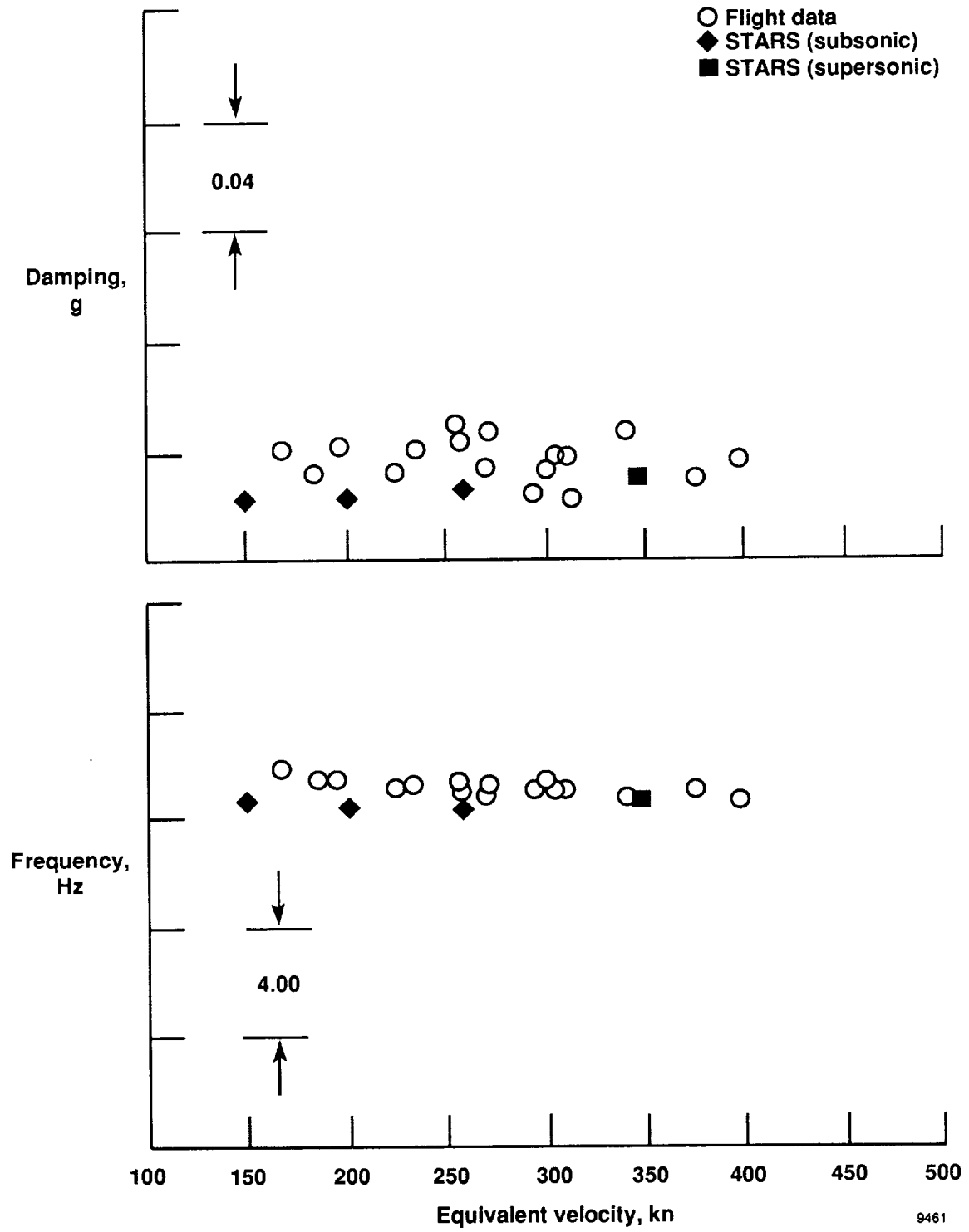
Figure 38. Continued.

02



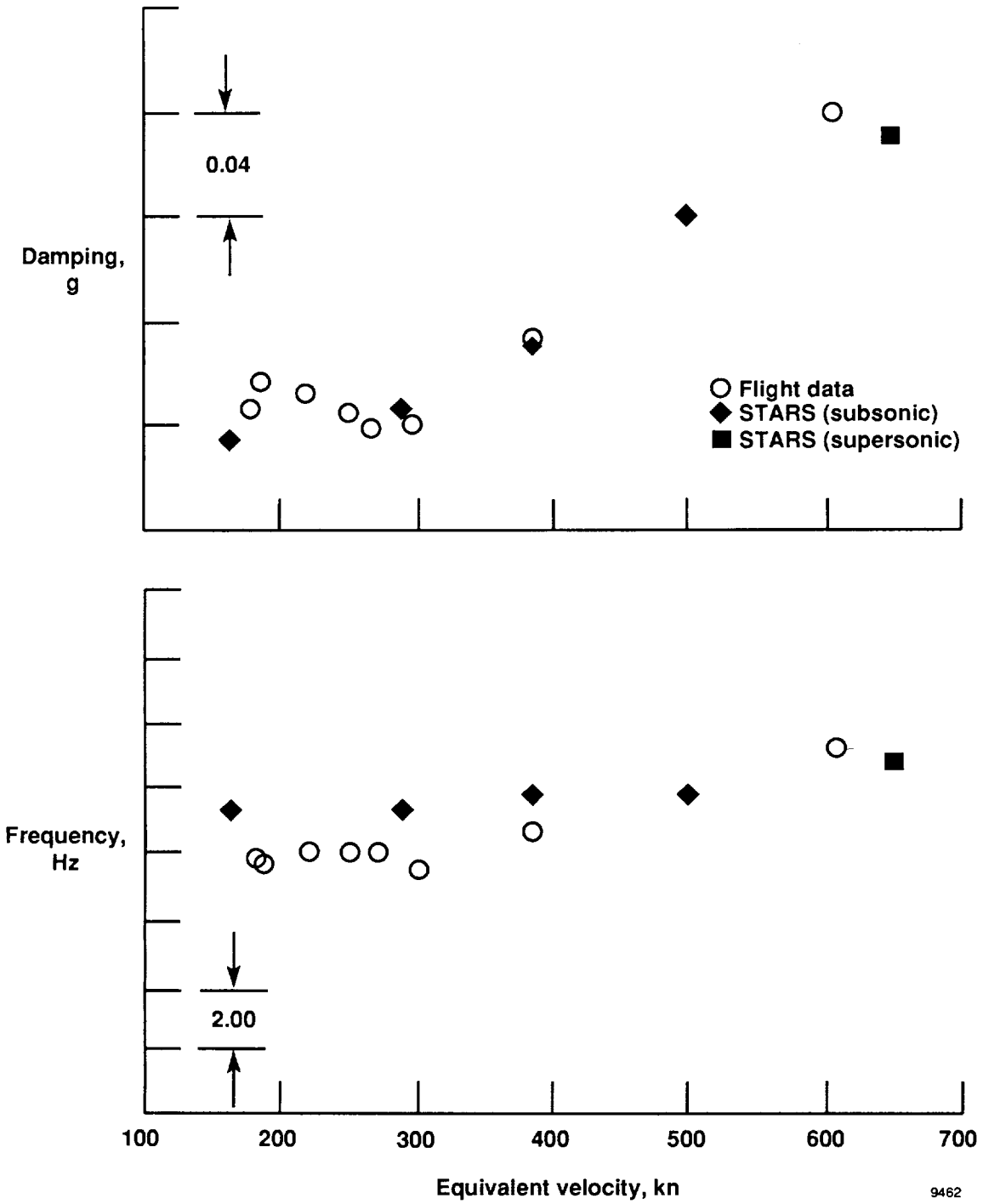
(c) 30,000 ft.

Figure 38. Continued.



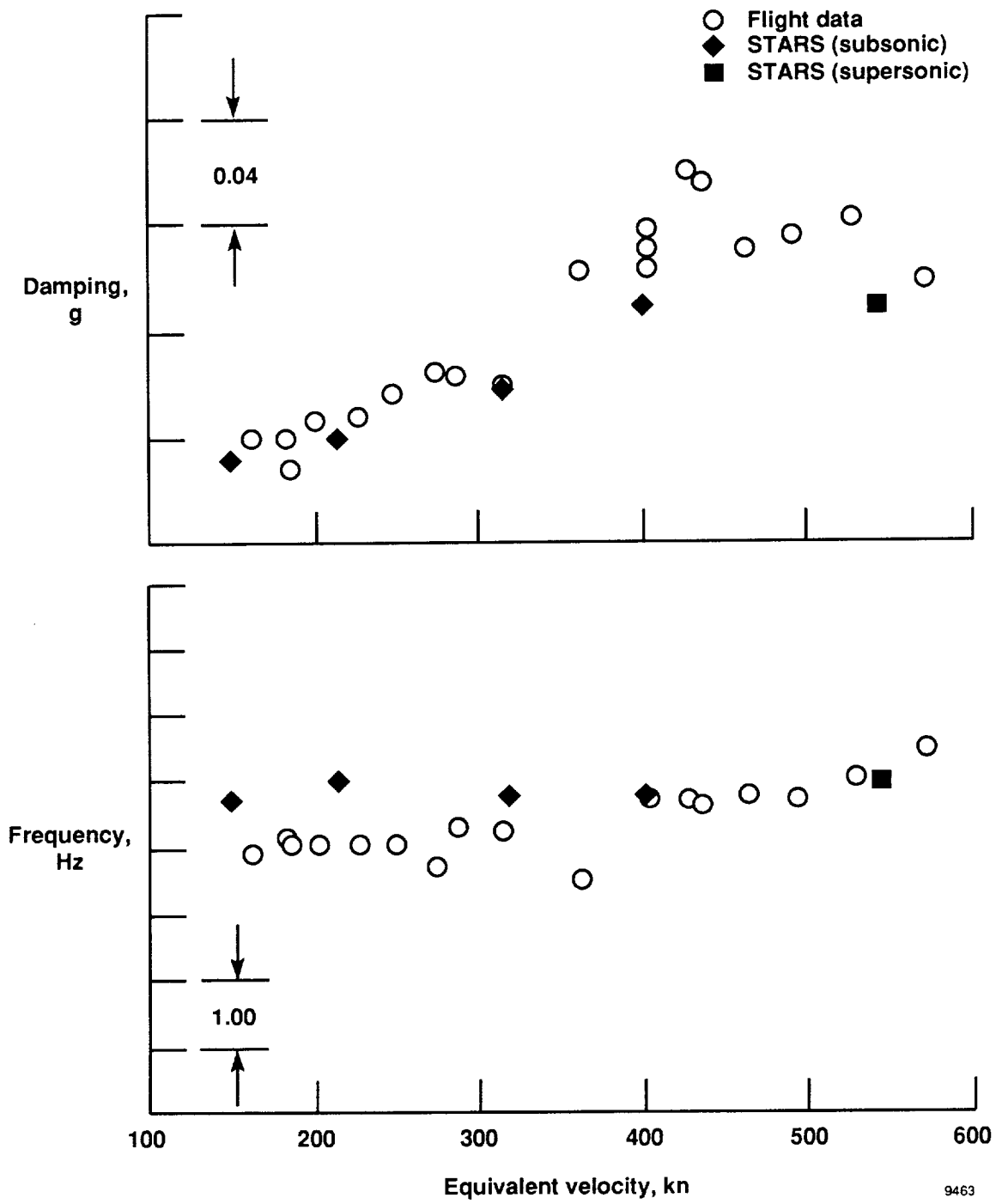
(d) 40,000 ft.

Figure 38. Concluded.



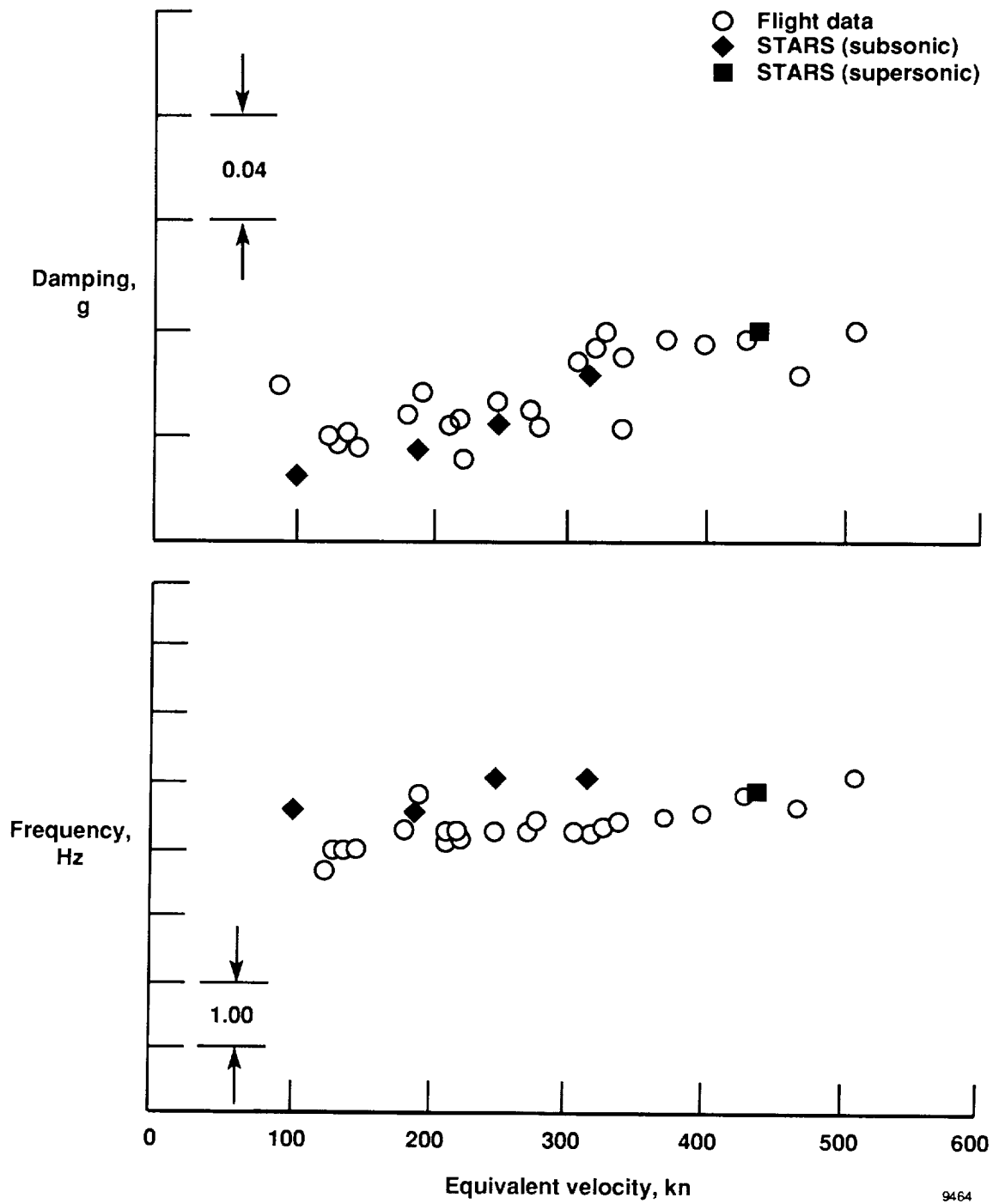
(a) 10,000 ft.

Figure 39. Modal damping and frequency comparisons between flight measured data and STARS for fin first bending.



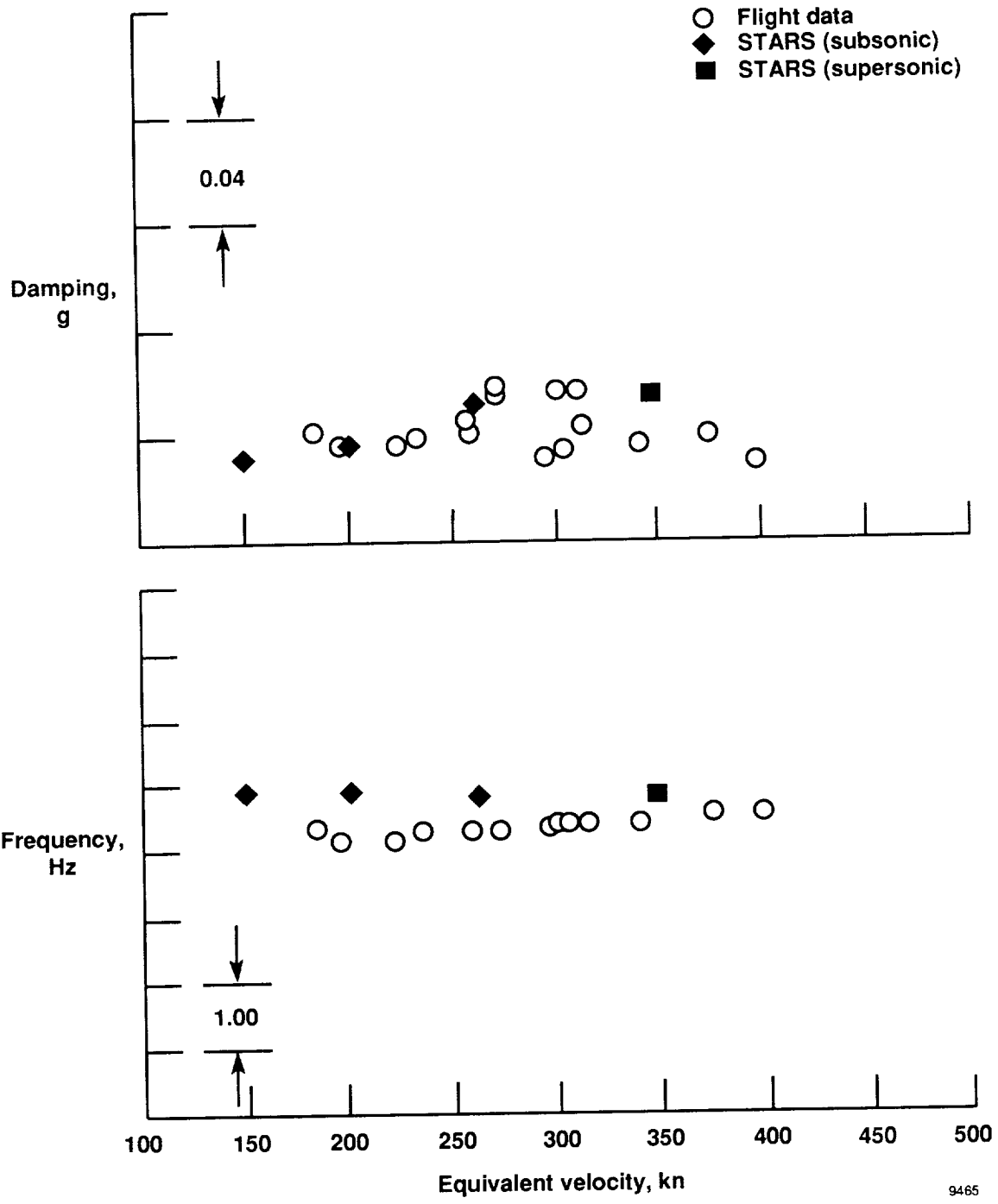
(b) 20,000 ft.

Figure 39. Continued.



(c) 30,000 ft.

Figure 39. Continued.



(d) 40,000 ft.

Figure 39. Concluded.

1. Report No. NASA TP-3120		2. Government Accession No.		3. Recipient's Catalog No.	
4. Title and Subtitle Development of an Integrated Aeroservoelastic Analysis Program and Correlation With Test Data				5. Report Date May 1991	
				6. Performing Organization Code	
7. Author(s) K. K. Gupta, M. J. Brenner, and L. S. Voelker				8. Performing Organization Report No. H-1543	
				10. Work Unit No. RTOP 533-02-51	
9. Performing Organization Name and Address NASA Dryden Flight Research Facility P.O. Box 273 Edwards, California 93523-0273				11. Contract or Grant No.	
				13. Type of Report and Period Covered Technical Paper	
12. Sponsoring Agency Name and Address National Aeronautics and Space Administration Washington, DC 20546-3191				14. Sponsoring Agency Code	
15. Supplementary Notes					
16. Abstract <p>This report presents the details and results of an extension of the general-purpose finite element STRUCTURAL Analysis RoutineS (STARS) to perform a complete linear aeroelastic and aeroservoelastic analysis. The earlier version of the STARS computer program enabled effective finite element modeling as well as static, vibration, buckling, and dynamic response of damped and undamped systems, including those with pre-stressed and spinning structures. Additions to the STARS program include aeroelastic modeling for flutter and divergence solutions, and hybrid control system augmentation for aeroservoelastic analysis.</p> <p>Numerical results of the X-29A aircraft pertaining to vibration, flutter-divergence, and open- and closed-loop aeroservoelastic controls analysis are compared to ground vibration, wind-tunnel, and flight-test results. The open- and closed-loop aeroservoelastic controls analyses are based on a hybrid formulation representing the interaction of structural, aerodynamic, and flight-control dynamics.</p>					
17. Key Words (Suggested by Author(s)) Aeroelastic; Aeroservoelastic; Finite element; Flight controls; Flight dynamics			18. Distribution Statement Unclassified — Unlimited Subject category 01		
19. Security Classif. (of this report) Unclassified		20. Security Classif. (of this page) Unclassified		21. No. of Pages 103	22. Price A06

